Magnetic, DC Transport, and Microwave Properties of High Temperature Superconductors

by

Paul Phong Nguyen

Submitted to the Department of Physics
in partial fulfillment of the requirements for the degree of

Doctor of Philosophy

at the

MASSACHUSETTS INSTITUTE OF TECHNOLOGY

August 1994

© Massachusetts Institute of Technology 1994. All rights reserved.

Author .....
Department of Physics
August 5, 1994

Certified by .....
Mildred S. Dresselhaus
Institute Professor
Thesis Supervisor

Accepted by .....
G.F. Koster
Chairman, Departmental Committee on Graduate Students

MASSACHUSETTS INSTITUTE
OF TECHNOLOGY

OCT 14 1994

LIBRARIES

Science

Magnetic, DC Transport, and Microwave Properties of High Temperature Superconductors

by

Paul Phong Nguyen

Submitted to the Department of Physics
on August 5, 1994, in partial fulfillment of the
requirements for the degree of
Doctor of Philosophy

Abstract

This thesis involves three major projects: 1. Effects of bromination on the dc transport and magnetic properties of $YBa_2Cu_3O_{7-x}$ (YBCO) single crystals, 2. Power dependence of the microwave surface impedance of $YBa_2Cu_3O_{7-x}$ thin films, and 3. Microwave properties of $YBa_2Cu_3O_{7-x}$ Josephson junctions.

In the first project, de-oxygenated non-superconducting $YBa_2Cu_3O_{6.2}$ single crystals are doped with Br. The resulting crystals (YBCOBr) become superconducting with $T_c \sim 92$ K, $\Delta T_c \sim 1.0$ K. This project was the first to measure the transport and magnetic properties of YBCOBr, whose rough surface has made it extremely difficult to make good electrical contacts. The normal resistivity in the best sample is linear in temperature. The large ratio in resistivity of the brominated to the pristine YBCO single crystals ($\sim$35:1) suggests that bromination greatly increases the scattering rate. The upper critical fields $H_{c2}(T)$ are measured resistively and the corresponding coherence lengths $\xi_{ab}(0)$ and $\xi_c(0)$ are estimated. A comparison with the fully oxygenated YBCO single crystals shows that $\xi_{ab}(0)$ remains approximately the same, whereas $\xi_c(0)$ decreases by a factor of ~ 3, suggesting that Br never enters the CuO_2 planes. The pinning energy for vortex motion in the *ab* plane decreases after bromination and this decrease can be attributed to the increased anisotropy. Compared with the fully oxygenated YBCO single crystals, the critical current density is suppressed by bromination and is strongly dependent on the applied magnetic field. The reduced lower critical field H_{c1} in YBCOBr indicates a reduction in the carrier density.

The second project involves thorough measurements of the surface impedance for the first time as a function of frequency (1–20 GHz), temperature (4.2–91 K), and peak rf magnetic field ($0 < H_{rf} < 500$ Oe) for high-quality epitaxial $YBa_2Cu_3O_{7-x}$ thin films, using a stripline-resonator technique. Unlike the other resonators such as cavities, the stripline resonator allows for the study of the frequency dependence of the surface resistance. The microwave-field-dependent surface impedance $Z_s(H_{rf})$ increases quadratically with increasing H_{rf} at low and intermediate rf fields ($H_{rf} <$ 50 Oe at 77 K) . The results for the low- and intermediate-rf-field regime are explained by the power-dependent coupled-grain model formulated in this work, which treats

the film as a network of superconducting grains connected by grain boundaries acting as resistively shunted Josephson junctions. Quantitative agreement has been obtained between the model and the measurements. In the high-rf-field region, $Z_s(H_{rf})$ changes to a different functional dependence on H_{rf}. Through the use of the modified Bean critical-state model, the results for the high-rf-field region are explained quantitatively for the first time by hysteresis losses due to the penetration of microwave vortices. The value of the microwave-vortex penetration field $H_p(T)$ for YBCO thin films, which is nearly frequency independent, is low compared with the dc lower critical fields. The critical current-density values obtained from fits to the hysteresis model are consistent with those measured via dc transport.

Finally, microwave measurements of YBCO Josephson junctions are presented with emphasis on the poorly understood power dependence. Prepared by an *in-situ* laser-ablation process, each junction is located at the midpoint of the center conductor of a stripline resonator so that only the odd resonant modes are altered by the junction. Unaffected by the junction, the even resonances provide an effective means to isolate the properties of the film from those of the junction. The results are analyzed using phase slip and microwave-vortex penetration into the junctions.

Thesis Supervisor: Mildred S. Dresselhaus
Title: Institute Professor

Acknowledgments

First and foremost, I would like to thank my thesis advisor Dr. Daniel E. Oates for being both a great advisor and a true friend. Among the most active people I have met, both in work and play, Dan has set a good model for me. I have benefited a great deal from his guidance as well as insightful ideas and suggestions, and from his unearthly listening skill, which should qualify him for some Hall of Fame.

I would also like to thank Prof. Mildred Dresselhaus and Dr. Gene Dresselhaus for all of their important suggestions and support, and for keeping my research on track. In addition, I would like to thank Prof. Raymond Ashoori and Prof. Louis S. Osborne for spending the time to serve on my thesis committee. Prof. J. Graybeal is also thanked for his encouragement in the early part of my thesis work.

Many others have also provided me with assistance and collaboration as well as friendship throughout my research. First I would like to thank the assistant group leader Dr. Gerry Sollner for taking special interest in the microwave part of my research. His support and helpful comments are gratefully acknowledged. He will be remembered as a critical reader whose strictness helped making my published papers referee-proof and speeding up the acceptance process. Second, Dr. Alfredo Anderson is greatly thanked for his high-quality films, and his useful ideas and insights on the microstructure of YBCO films as well as other microwave-related topics. His Shakepearean humor, which complements Dan's humor rather well, has helped enliven the work place; and his coffee grinder has served as a starting morning signal for my work day. Bob Konieczka is especially thanked for his help and training on the fabrication of stripline resonators, as well as his interesting discussions. He and Rene Boisvert, Terry Weir, and Billy Walker are gratefully acknowledged for the assistance in the measurement lab. Furthermore, I would also like to thank the group leaders Dr. Richard Ralston and Dr. Gerry Sollner of Lincoln Lab, and Drs. Paul Carr and Dallas Hayes of Rome Lab for their leadership guidance and for securing funding. Dr. David Feld is also acknowledged for the helpful discussions on Josephson junctions, as well as other topics related to general world problems. Dr. Sylvie

Revenez, Dr. Lawrence Lee, and the graduate students in Prof. M. Dresselhaus's and Dr. D. Oates's group, Joe Habib and Nathan Belk are also thanked for useful discussions. Dr. Kimo Tam is especially acknowledged for his help with the computer. The other postdoc and graduate students in Prof. M. Dresselhaus's group: Drs. Zhaohui Wang and X. X. Bi, Lyndon Hicks, Alex Fung, Gillian Reynolds, Siegfried Fleischer, Steve Cheng, James J. Chen, and the rest are also thanked for the technical discussions, support and friendship.

Profs. G. Koren and E. Polturak are gratefully acknowledged for preparing the YBCO edge junctions. Profs. Sridhar, M. Tinkham, J. Clem, S. Anlage and T. Orlando, and Drs. J. Halbritter, John Steinbeck, John Derov, and Balam Willemsen are thanked for the useful technical discussions.

Joe Flavin, Mary Bourquin, and the rest of the staff in publications, and especially Phoebe Wang are thanked for promptly preparing many of the figures for my papers and presentations. I would also like to thank Karen Challberg for technical editing of papers for publications.

The research at MIT Lincoln Lab was supported in part by the Air Force Office of Scientific Research, and in part by the Advanced Research Project Agency under the auspices of the Consortium for Superconducting Electronics.

To my parents,

my sister and brother-in-law, and my brother

for their love and support

Contents

List of Figures

List of Tables

Chapter 1

Introduction

The revolutionary discovery of high-T_c superconducting oxides has sparked new interest in the science and technology of superconductive materials. High-T_c superconductors offer a host of interesting new phenomena, including the high transition temperature T_c, whose underlying mechanisms have defied theoretical explanations. With T_c above 77 K, the boiling temperature of inexpensive and easy-to-use liquid nitrogen, high-T_c superconductors make highly attractive candidates for industrial use.

This thesis reports the research I have carried out on high-T_c compounds, specifically $YBa_2Cu_3O_{7-x}$ (YBCO). The electrical and magnetic properties of these materials are essential to an understanding of the mechanisms of high-T_c superconductivity, and of course, to applications.

The organization of this thesis is described in the following. In Chapter 2, I describe some of the basic structural and physical properties of high-T_c superconductors, with emphasis on YBCO. I review the relevant thin film deposition techniques and the resulting film microstructures to provide the necessary background. This chapter is largely a review of the literature.

The next chapter, Chapter 3, the effects of bromine doping on YBCO is investigated. In a way, the discovery of high-T_c superconductors was a direct result of substitutions and dopings on related low-T_c or nonsuperconducting systems. Consequently, it is natural to turn to substitutional studies to search for superconducting

compounds with higher T_c and to understand the mechanisms for superconductivity. Substitutional studies also can help replace toxic, rare, or expensive components with less toxic, abundant, or cheaper ones without compromising on the superconducting properties. Substitutional studies have been performed on most of the high-T_c materials, especially on $YBa_2Cu_3O_{7-x}$, replacing most of the compositional elements with equivalent ones. Replacing oxygen by bromine in YBCO powder and single crystal has been shown to produce exciting results, with the final products retaining the same or slightly higher T_c. The doping process occurs at relatively low temperatures (around 260°C) and the reaction is highly exothermic, yielding strong bonding of the bromine in the lattice. The low processing temperatures and the stability of the final products makes bromination of YBCO potential for industrial applications. The issues that still remain to be resolved involve the mechanisms of Br diffusion into and reaction with YBCO, the location of Br in the lattice, and the mechanisms by which superconductivity is restored in the nonsuperconducting deoxygenated YBCO compounds by Br-doping. This chapter presents the results on the transport and magnetic measurements on brominated YBCO single crystals with the hope to shed light into the above issues.

Chapter 4 details the experimental procedure for the microwave measurements. The concept of surface impedance Z_s is reviewed, followed by a brief discussion of the stripline-resonator structure I use in this work. I also point out the complications that arise from going to high microwave powers, where Z_s becomes nonlinear, i.e., dependent on power.

Chapter 5 makes up the bulk of this thesis where data from my Z_s measurements on YBCO thin films and related analysis are presented. For dc or low frequencies, electrical losses due to quasiparticles in a superconductor approach zero as the superconducting pairs shunt the quasiparticles. Consequently, little useful information can be obtained in the superconducting state. On the other hand, at high frequencies such as microwave frequencies, losses due to quasiparticles can be clearly observed, as the quasiparticles are induced to moved simultaneously with the superconducting pairs. Microwave measurements hence provide a sensitive probe to study the supercon-

ducting state of a superconductor. Since microwave excitations of quasiparticles are insensitive to lattice conduction modes (i.e., phonons), microwave measurements hold an advantage over other measurement techniques such as specific heat that attempt to probe the electronic state. If the superconductor contains defects which generate low-energy excitations in the superconducting phase, microwaves also provide an excellent probe of these defects and an effective way to characterize the sample.

In addition to probing the quasiparticles in the superconducting phase, microwave measurements also provide information on the superconducting condensate via the kinetic inductance. All the microwave measurements can be performed without physical contact to the samples, circumventing the contact-resistance problems that have plagued dc measurements of high-T_c superconductors.

The technological importance of studying the microwave surface impedance of high-T_c superconductors cannot be overstated. For many applications of these materials, such as resonators, filters, and low-loss delay lines, the surface impedance provides an essential figure of merit since it represents the losses incurred in the device.

Chapter 6 moves on from the subject of surface impedance to explore the microwave properties of high-T_c Josephson junctions, especially the microwave power dependence. The motivation for this investigation of high-T_c junctions is two-fold. First, as observed in the microwave measurements, structural defects in high-T_c superconductors appear to dominate their transport properties. These defects behave like a network of weak-link Josephson junctions. Detailed study of individual isolated junctions is necessary for an overall understanding of the properties of such a junction network. Second, the physical mechanisms involved in each individual isolated junction also warrant a thorough study themselves, as high-T_c junctions are still poorly understood, even though their potential for technological applications is tremendous.

Finally, Chapter 7 summarizes the main points of the thesis and offers some suggestions for related future research.

Chapter 2

Material Properties Of High-T_C Materials

In this chapter, we briefly review the relevant properties of the high-T_c superconductor $YBa_2Cu_3O_{7-x}$ (YBCO) to provide the necessary background for the research described in this thesis. The crystal structure of the Y-based compound is first examined to illustrate the anisotropic nature of the high-T_c material and to define the non-equivalent oxygen sites in the lattice. The relationship between the oxygen stoichiometry, the lattice parameter, and T_c in the bulk samples is then discussed. Next the thin film preparation techniques and the resulting film microstructures are studied in some detail as they form the conceptual basis for many discussions in this thesis.

2.1 Structure

Superconducting $YBa_2Cu_3O_{7-x}$ has a modified perovskite crystal structure in which there are several non-equivalent oxygen sites. As shown in Fig. 2-1, oxygen is ordered on the basal plane such that oxygen occupies sites along the b-axis O(4) and is absent along the a-axis, hence creating copper-oxygen (CuO) chains.

Copper-oxygen planes sandwich the yttrium atom with oxygen in the O(2) and O(3) sites. The compound can exist over a range of oxygen stoichiometry from $0 \leq x \leq 1$ with its electrical properties changing from superconducting near $x = 0$

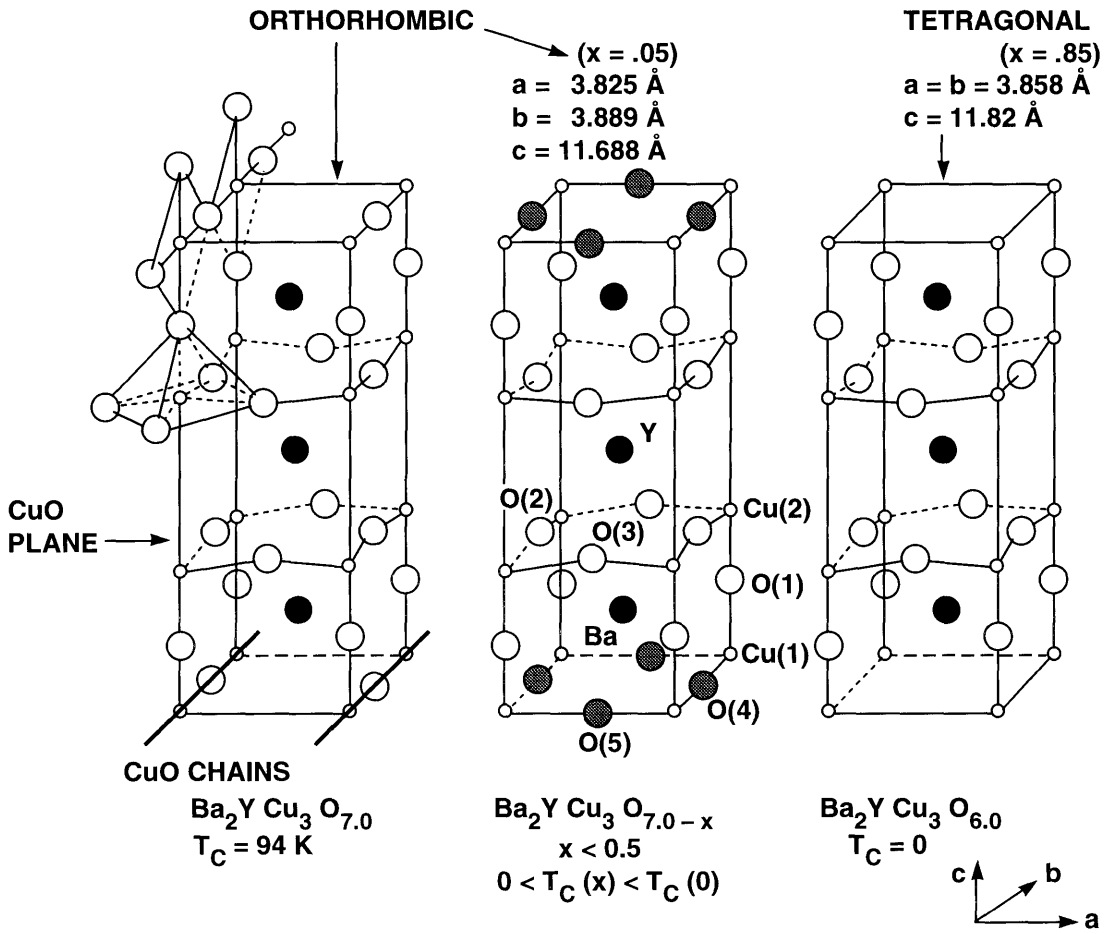

Figure 2-1: The YBCO crystal structure is composed of alternating BaO, CuO_2, Y, CuO_2, BaO, and CuO layers [1]. The structure is similar to a perovskite with the unit cell tripled in length along the c-axis. The CuO chains lie along the b-axis.

to semiconducting near $x = 1$. As oxygen is depleted from the lattice, the structure of YBCO changes continuously from orthorhombic to tetragonal. Changes in oxygen occupancy have been measured in bulk ceramic samples by a variety of techniques: neutron diffraction, thermogravimetric analysis (TGA) [2], transmission electron microscopy (TEM) [3], and x-ray analysis by profile fitting of weak 012 and 102 diffraction peaks [4]. Changes in oxygen content are shown in these studies to be accommodated by changes in the oxygen occupancy of the O(4) site along the CuO chains while the CuO planes remain fully oxygenated. The structure becomes unstable and decomposes as oxygen is further depleted from the lattice beyond $x = 1$.

For the bulk YBCO compound, the relationship between lattice parameter, oxygen content, and T_c has been extensively studied [5]. Fully oxygenated YBCO ($x = 0$) has the following lattice parameters: a = 3.825$\AA$, b = 3.889$\AA$, and c = 11.688$\AA$. As oxygen is depleted, the unit cell expands along the a-axis and the c-axis and contracts along the b-axis (Fig. 2-1). Oxygen depletion also results in a reduction of T_c. Changes in lattice parameter as a function of temperature and oxygen pressure have also been measured *in situ* using hot stage x-ray analysis by Specht *et al.* [6]. At a fixed oxygen pressure, the a-axis and c-axis lattice parameters increase with temperature while at fixed temperature, these parameters decrease with increasing oxygen pressure. The orthorhombic to tetragonal transformation temperature decreases with decreasing oxygen pressure.

The oxygen stoichiometry has an even more profound effect on the electrical transport properties than on the structural properties of YBCO. In the O_6 state, YBCO is a non-superconducting antiferromagnetic insulator with the Cu(2) spins antiferromagnetically ordered (see for instance, Beyers *et al.* and references therein [1]). Band structure calculations, however, predict that the O_6 state should be metallic, and much theoretical effort has been expended to explain this discrepancy. It has been widely believed that in the insulating state, the strong electron correlations renders $YBa_2Cu_3O_6$ a charge-transfer or Mott-Hubbard insulator (see for instance, Yasuhiro Iye [7]). With higher oxygen concentration, phenomenologically, as the oxygen concentration is increased above the O_6 level the material undergoes an insulator-metal

transition at an oxygen concentration [1] of about 6.4. A superconducting transition at finite transition temperature appears simultaneously with the metallic behavior. As the oxygen concentration increases past the insulator-metal transition, the T_c increases from zero, approaching a maximum of about 94 K in the O_7 state. Further increases in oxygen concentration in YBCO are extremely difficult, though possible for certain substitutional variants [8]. The increase in T_c with doping is monotonic but shows some interesting plateaus at $T_c = 60$ K and 90 K. The plateau at 60 K has been attributed to partial oxygen ordering in the chains. The maximum T_c of up to 96 K can achieved at some optimal doping level [9].

A charge-transfer picture has been widely adapted to explain the sensitivity of the YBCO compound to oxygen concentration: the chain oxygens dope holes onto the CuO planes. In this picture, the CuO chains act only as charge reservoirs and play no role in the superconducting mechanism. The mechanisms responsible for the superconductivity and the electrical behavior of the high-T_c materials have been a subject of great debate with no clear consensus at this time.

2.2 Superconducting Properties

The new copper-oxide superconductors have many unusual properties of which the three most unique are high transition temperature T_c, short coherence lengths, and large anisotropy.

The high transition temperatures of the copper-oxide superconductors allow for operations in the superconducting state at much higher temperatures than previously possible. At the same time, such high-temperature operations pose new problems related to thermal fluctuations. Because thermal activation is much higher at high temperature, vortices jump more readily from their pinning sites, causing giant flux creep effects. Large flux creep broadens the transition temperature in an applied magnetic field, making it harder to determine T_c accurately and limiting the usefulness of the copper-oxide superconductors.

The extremely short coherence lengths in the high-T_c leads to the high sensitivity

of their electromagnetic properties to any type of structural defects such as grain boundaries, regions of nonstoichiometry and oxygen-deficiency, twin boundaries, etc.

Anisotropy complicates the measurements and interpretations. The large anisotropy in the high-T_c compounds both in the superconducting and normal phases arises from the layered structure. As described above, the bulk of the carrier density is believed to reside in CuO planes. Strongly decoupled layered superconductors have been analyzed theoretically by Lawrence and Doniach [10]. Their model extends the standard Ginzburg-Landau theory to the case of strongly decoupled 2-D superconducting layers coupled by Josephson junctions, and hence provides a suitable description of the highly anisotropic BiSrCaCuO (BSCCO) and TlBaCaCuO (TBCCO) materials. For YBCO, however, because the interlayer coupling is strong, the simpler Ginzburg-Landau theory with an anisotropic mass tensor is adequate [11]. The ratios of the penetration depths for YBCO are $\lambda_a : \lambda_b : \lambda_c \rightarrow 1.2 : 1 : 5$ as determined from flux lattice decoration experiments [12]. Since the anisotropy in the ab plane is small, it will be ignored in the following discussion. The corresponding mass ratio is the square of the λ values: $m_c/m_{ab} \simeq 25$. Muon spin relaxation measurements reveal the penetration depth $\lambda_{ab} = 1400\mathring{A}$ at low temperature [12].

2.3 Superconducting $YBa_2Cu_3O_{7-x}$ Thin films

2.3.1 Introduction

For many reasons, superconducting thin films deserve a study of their own, separate from the bulk superconductors. In superconducting thin films, a host of interesting new phenomena, many of which are surface-related, arise that do not exist in bulk form. High-T_c thin films have generally yielded higher critical current densities which, together with good control and reproducibility as well as ease of use, make them attractive candidates for applications. Superconducting thin films can be used in hybrid superconducting-semiconducting circuits and microwave and millimeterwave devices, for instance. Such devices are important in circuit applications for rf signal

generation, electromagnetic wave detection and mixing, parametric amplification and frequency conversion, and high-sensitivity magnetometry and switching [13].

The preparation techniques for the high-T_c superconducting films are the underpinning of this work, which examines film defects and how they affect the film properties. In this section, I review extremely briefly the techniques used to produce the YBCO films I measured. Knowledge of the deposition and thin film growth process provides important clues as to the nature of the defect structures in the films. All of the thin film techniques discussed here are for preparing oriented YBCO films on single crystal substrates. Polycrystalline, unoriented films will not be discussed in this work due to their poor transport properties. I also present a schematic of the important defect structures in the film that provides a conceptual basis for many of the discussions in this thesis.

2.3.2 Deposition Techniques

YBCO thin films have been successfully grown by several fabrication techniques including chemical-vapor deposition, sputtering, laser ablation, spray pyrolysis, and molecular-beam epitaxy [14, 15]. Various materials have been used as single-crystal substrates for these films, including $SrTiO_3$, MgO, ZrO_2, Al_2O_3 (sapphire), $LaAlO_3$, $LaGaO_3$, and silicon [14].

Among the different deposition processes, one of the most widely used for growing highly epitaxial films *in situ* is sputtering. Substrate-target orientation in sputtering has a major impact on the film stoichiometry: negative ion bombardment onto the substrate leads to re-sputtering of the deposited film causing a change in stoichiometry. To prevent this, various methods such as high gas pressures, low discharge voltages, and off-axis placement of substrates have been successfully employed [14].

Most of the YBCO superconducting films measured in this work were grown *in situ* on $LaAlO_3$ substrates, using off-axis rf magnetron sputtering and cylindrical magnetron sputtering.

In the off-axis configuration, the target and the substrate are situated at a 90° angle to each other to minimize the adverse effects of film bombardment resulting

from negative ions ejected by the target. The main advantage of this technique is its simplicity and the main disadvantage is the slow deposition rate, typically on the order of $5 - 10$ $\mathring{A}$/min. It should be noted that even though a single-target stoichiometric source is used, the composition of the deposited film is not necessarily the same as that of the target [13].

In the cylindrical magnetron sputtering configuration, the target is shaped in the form of a hollow cylinder. The main advantages of this technique are that it is simple and that the deposition rate is almost ten times faster than off-axis sputtering. In addition, it is possible to vary substrate bombardment by changing the anode voltage in this system. As with any single-target technique, composition of deposited films cannot in general be changed without replacing or altering the target [16].

2.3.3 Film Structures

X-ray-diffraction studies show the films with the best electrical properties to be almost completely c-axis oriented. SEM analysis indicated micrometer-sized boulder-like precipitates protruding from the surface of the film [17], as seen in Fig. 2-2.

Smaller submicrometer precipitates, distributed between the larger precipitates, can also be seen in Fig. 2-2. In Fig. 2-3, a low-magnification micrograph shows both types of precipitates marked as A and B. Energy dispersive X-ray spectroscopy (EDS) spectrum identifies the larger precipitate A as copper oxide (CuO). EDS identifies the smaller precipitate B as barium chromium oxide. A third type of precipitate is also found in the film (Fig. 2-4). These extremely small precipitates are about $15 - 20$ nm and are commensurate with their lattice rotated by a 45° twist along the c-axis of the surrounding film. An EDS analysis identifies these precipitates to be yttrium oxide (Y_2O_3) [13].

All c-axis oriented YBCO films contain some a-axis grains [13] though the number of these grains is extremely small for the best c-axis films. In addition, the films show numerous stacking faults, mostly in the form of extra CuO planes, some examples of which are marked by arrows in Fig. 2-5 [17].

Twinning along the [110] and [1$\bar{1}$0] directions is also observed. The TEM micro-

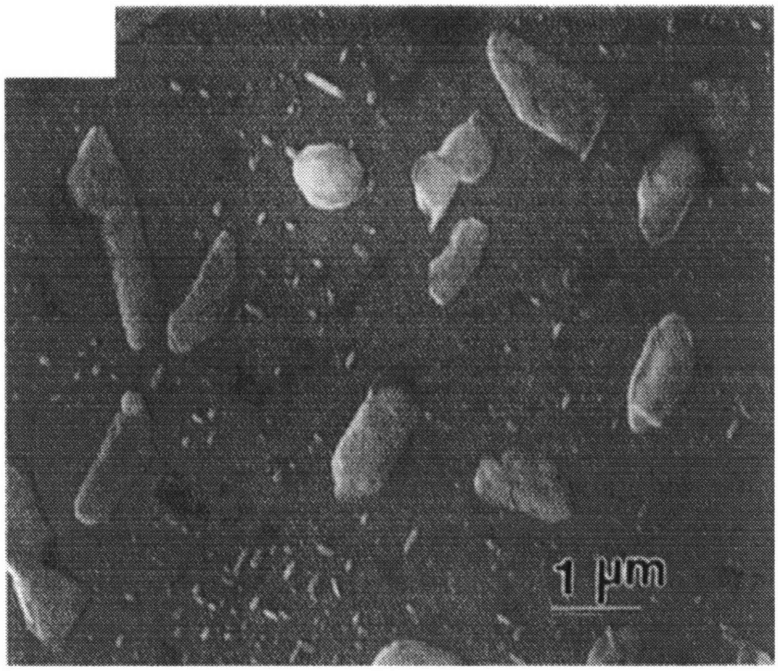

Figure 2-2: Scanning electron micrograph showing CuO precipitates on the film surface (Westerheim *et al.* [17]).

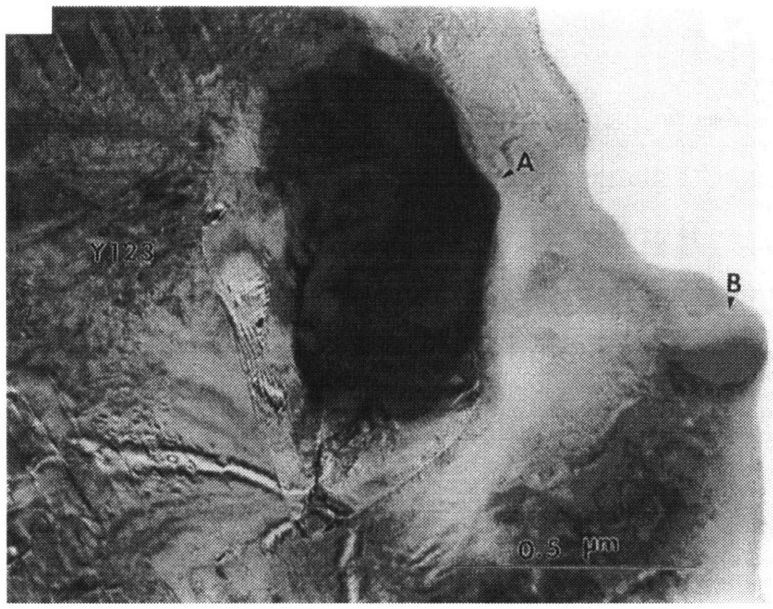

Figure 2-3: Plan-view TEM brightfield micrograph showing two types of precipitates marked as A and B (Bhatt *et al.* [13]).

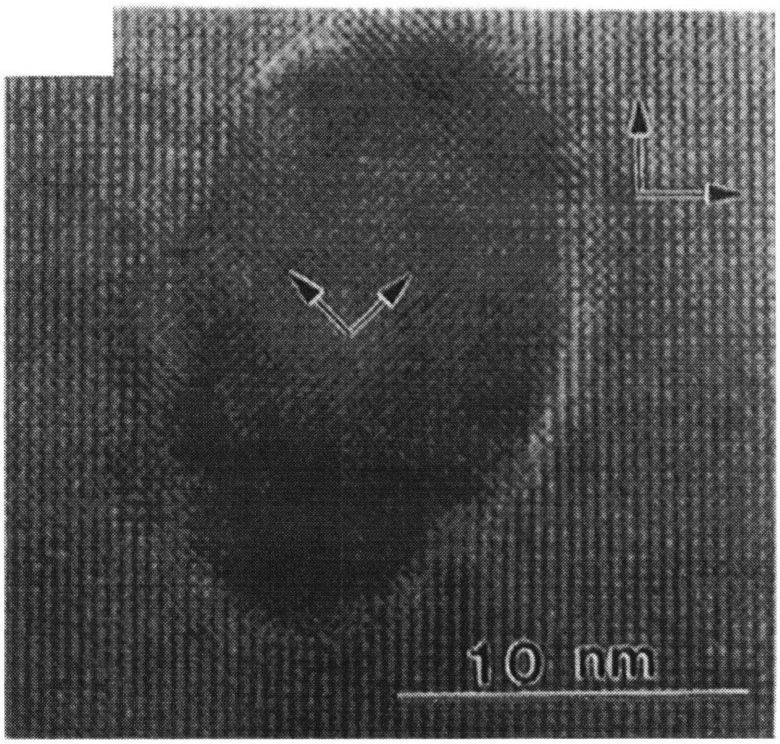

Figure 2-4: High-resolution TEM micrograph of Y_2O_3 precipitates. The precipitate is coherent with its lattice rotated at 45° to the YBCO lattice (Bhatt *et al.* [13]).

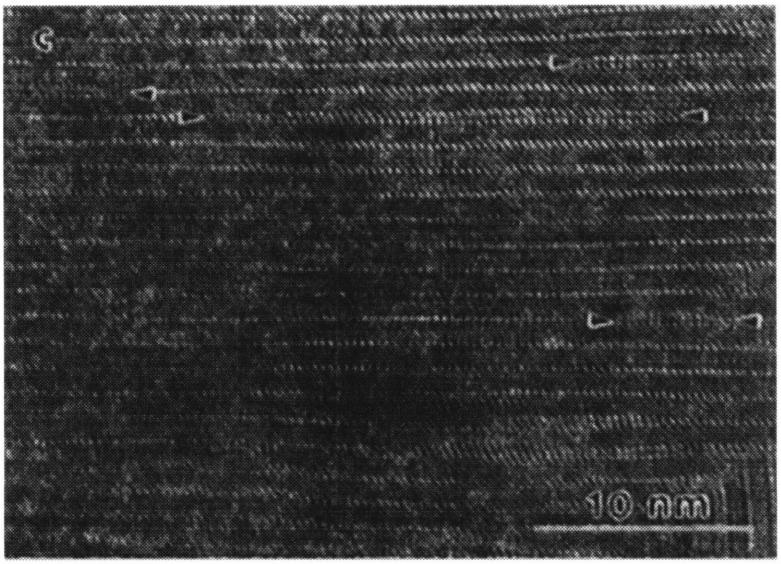

Figure 2-5: TEM showing stacking faults (Westerheim *et al.* [17]).

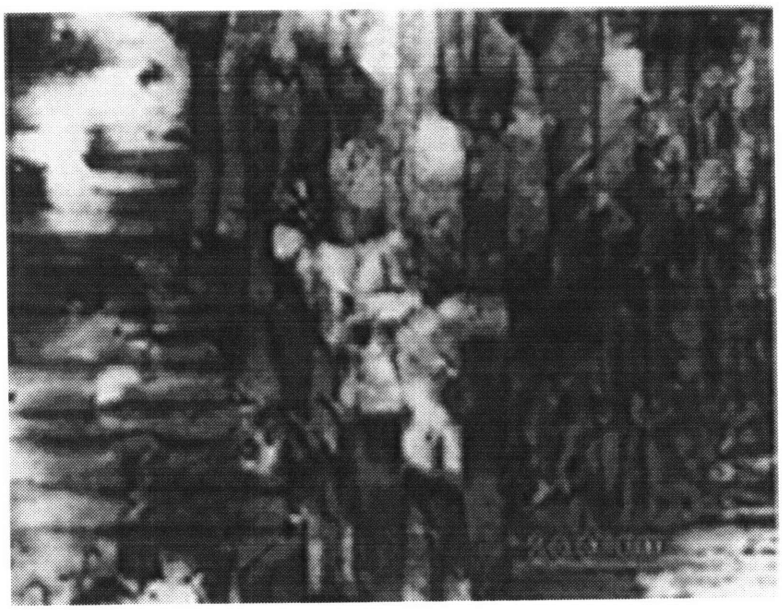

Figure 2-6: TEM brightfield micrograph showing twin boundaries in a c-axis oriented film (Bhatt *et al.* [13]).

graph in Fig. 2-6 exhibits both mutually perpendicular variants of the twins. The twin boundaries appear fairly regularly spaced separated by a distance of approximately 50 nm.

The schematic in Fig. 2-7 illustrates the important point, line, and plane defects arising from misfit dislocations caused by dislocated atoms in the lattice. Smaller defective regions of extra phase (CuO, Y_2O_3, etc.) formations are similar to point defects in their effects on the transport properties and hence are lumped together with point defects in Fig. 2-7. Defects at the substrate-film interface are usually healed within a few hundred $\AA$ into the film and hence are assumed unimportant in determining the transport properties of the relatively thick films discussed in this work. Chapter 5 considers the influence of these structural defects on the microwave surface impedance of the films.

The substrate selection and the deposition method together with the deposition temperature and pressure, all influence the properties of the resulting films in ways not fully understood. The defect structures in the films are shaped by various competing mechanisms: thermodynamics, mobility, vacuum-film interface and film-substrate

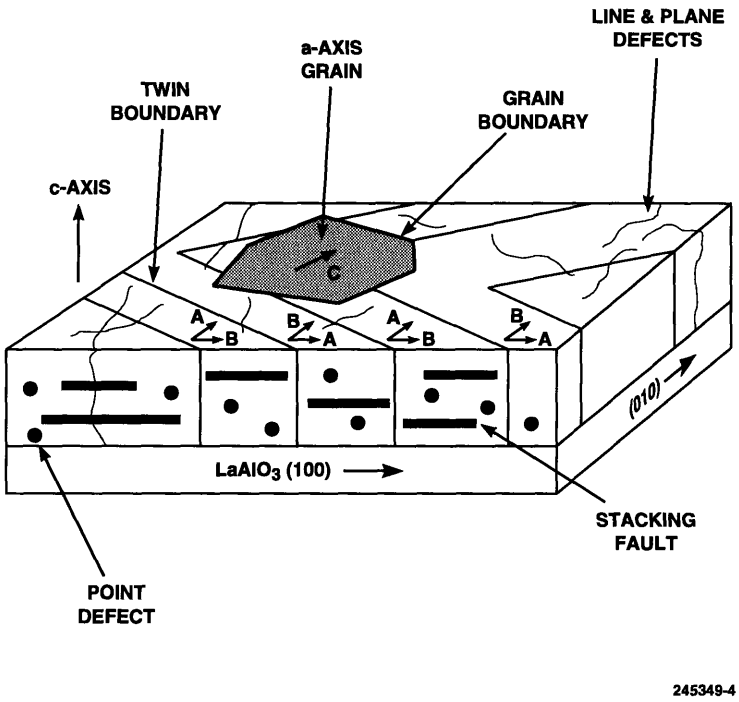

Figure 2-7: Schematic of an *in situ* c-axis oriented YBCO film on $LaAlO_3$ showing some important defect structures: twin boundaries, point defects, line and plane defects, a-axis grains, and stacking faults.

interface. Generally, higher mobility of the atomic components results from higher deposition temperature. The formation of large defect structures, such as second phase inclusions and non-stoichiometric grain boundaries, is possible with higher mobility because the atomic components can segregate over large distances. The formation of small-scale defects such as substitutions and interstitials to accommodate non-stoichiometric material, on the other hand, is more likely with small mobility. Higher deposition temperatures, however, favor situations of greater entropy and hence tends to promote growth of small-scale defects. The deposition temperature and the oxygen growth pressure modify the free energy of the YBCO phase relative to the competing phases and defect structures. Varying the temperature and pressure hence affects greatly the quality of the films deposited [17, 18].

Chapter 3

Transport and Magnetic Properties of $YBa_2Cu_3O_{7-x}Br_y$ Single Crystals

3.1 Introduction

Substitution studies of high-T_c superconductors can provide insight into the mechanisms of superconductivity and produce new materials with higher T_c and other improved properties.

In substitutional studies, three primary factors influence site occupancy:

1. Ionic radii,
2. Valence state, and
3. Coordination number of the on-site cation

Table 3.1 [19] shows the valence state and ionic radii corresponding to different coordinations of various cations of some high-T_c superconducting compounds.

In general, complete substitution of a dopant is possible when it is isovalent and for the same coordination number, its radius is within 15% of the on-site cation. Otherwise, the substitution is only partial [19].

Many substitution studies have been made on various components of different high-T_c compounds [19]. For the Yttrium-based cuprates, substitutions at all of the

Table 3.1: Properties of cations forming some high-T_c compounds.

Compound	Cation	Valence State	Existing Coordination Number	Corresponding Ionic Size ($\AA$)
$La_2(Sr)CuO_4$	La (Sr)	3 +	9	1.20
	Cu	2 +	6	0.73
$YBa_2Cu_3O_7$	Y	3 +	8	1.02
	Ba	2 +	10	1.52
	Cu(I)	2 +	4	0.62
	Cu(II)	2 +	5	0.65
$Bi_2CaSr_2Cu_2O_x$	Bi (Tl)	3 +	6	1.02 (.68)
	Ca	2 +	8	1.12
	Sr (Ba)	2 +	9	1.30 (1.4)
	Cu	2 +	5	0.65
$Ba(K)BiO_3$	Ba (K)	2 +	12	1.60
	Bi	3 +	6	1.02

cation sites (Y, Ba, and Cu) have been studied. Substitutions at the anion O-sites of Yttrium-based cuprates have also been investigated to see if high-T_c superconductivity can exist in non-oxide compounds. Specifically, halogens such as F, Cl, Br, and I have been used extensively as substitutional elements for O.

Halogen doping at modest temperatures provides an interesting method for restoring superconductivity in partially de-oxygenated non-superconducting $YBa_2Cu_3O_{6.2}$ crystals [20, 21, 22, 23]. The introduction of Br at low temperature 260°C and in a short time (> 5 minutes) has been shown [20] to convert initially insulating powder $YBa_2Cu_3O_{6.2}$ to a high-T_c superconductor with similar properties to the fully oxygenated $YBa_2Cu_3O_{7-x}$ compound. With longer Br exposure time, similar results have been observed in oxygen-deficient $YBa_2Cu_3O_{6.2}$ single crystals [22]. The reaction of the oxygen-deficient compound with Br has been found to be highly exothermic, suggesting strong bonding of the Br in the lattice. Thermal gravimetric analysis coupled with mass spectrometry indicates no release of Br from brominated powder samples heated up to 1000°C in flowing forming gas ($2\%H_2/98\%N_2$). Because of the relatively low processing temperature ($\sim$ 260°C for Br compared with $\sim$ 450°C for O) and the stability of the brominated $YBa_2Cu_3O_{6.2}$ compound to high temperatures (though further loss of oxygen can occur in the brominated samples at elevated tem-

peratures), these halogenated compounds have attracted attention for possible use in connection with hybrid semiconductor-superconductor integrated circuit devices.

Outstanding questions remain as to the mechanisms of diffusion and reaction of the Br with the deoxygenated compound, and the mechanisms by which the superconductivity is restored upon bromination. The location of Br in the lattice has also been of great interest because it gives insights into the role of charge transfer in the oxide superconductors. Previous attempts to locate the bromine position in the lattice have proved inconclusive, chiefly because the x-ray diffraction pattern broadens significantly when the bromine is present. Radousky and coworkers [24] conclude that this broadening results from the bromine occupying several non-equivalent sites in the lattice. This point of view has recently been strengthened by the results of Amitin et al.[25] who conclude from detailed NMR work on YBCO-Cl material that the Cl occupies three separate sites in the lattice.

In this chapter, I investigate the temperature and magnetic field dependence of the conductivity and magnetic susceptibility of brominated YBCO, and I relate these properties to the fully oxygenated superconducting YBCO both in the normal and superconducting states. The goal is to gain further understanding through these transport measurements on the role of Br in restoring superconductivity to de-oxygenated YBCO. In Sect. 3.2, I discuss sample preparation and characterization, and the experimental procedures. In Sect. 3.3 the results of zero-magnetic-field transport measurements are presented, while Sect. 3.4 is devoted to the corresponding resistivity measurements in a magnetic field parallel and perpendicular to the $\hat{c}$-axis at temperatures close to T_c. Section 3.5 estimates the pinning potentials for vortex motion parallel and perpendicular to the ab plane. Sect. 3.6 presents the results of the measurements of the critical current density $J_c(T, H)$ and the lower critical field. Sect. 3.7 summarizes the results of the chapter.

3.2 Experimental

3.2.1 Sample Preparation and Characterization

The starting materials used for these experiments were small nearly rectangular platelets ($\sim 1.2 \times 0.9 \times 0.05$ mm) of high-quality $YBa_2Cu_3O_{7-x}$ single crystal with $T_c \sim 92$ K and $\Delta T_c \sim 1.0$ K, as determined from resistivity measurements. These crystals were de-oxygenated by heating at 600°C for ~12 hours and subsequently brominated for 24 hours at 260°C, as described by Radousky *et al.* [22].

Though the lattice constants of the brominated YBCO single crystals studied here were not measured, previous x-ray-diffraction data taken on brominated powder showed an orthorhombic structure which is consistent with the result of others [22, 26, 27, 28, 29], with the lattice constants $a = 0.38274 \pm 0.0008$ nm, $b = 0.3880 \pm 0.001$ nm, and $c = 1.1636 \pm 0.004$ nm [22]. These measured lattice constants are similar to the results of joint x-ray and neutron diffraction by Williams et al.[28], though slightly less than those reported by Jorgensen [29]. Although x-ray data were not obtained on the crystals measured here, the brominated crystals from similar runs were found in general to be twinned as they had been prior to bromination.

Auger depth profiling and energy dispersive x-ray analysis on these samples confirmed the uniform incorporation of Br in the de-oxygenated $YBa_2Cu_3O_{6.2}$ single crystals with a nominal stoichiometry $YBa_2Cu_3O_{6.2}Br_{0.9}$ [30]. Previous work on powders and crystals had shown that for crystals with near 100% magnetic-shielding fractions, both weight gain and x-ray-fluorescence microprobe measurements find the bromine content to be 0.9 (i.e., $YBa_2Cu_3O_{6.2}Br_{0.9}$). The oxygen content is nominal, and is based on similar de-oxygenation procedures performed on powders. The oxygen content is assumed not to change during the bromination (since the bromination temperature is low compared with the de-oxygenation temperature) [22].

The magnetic susceptibility measurements were carried out using a superconducting quantum-interference device (SQUID) to characterize the samples for their shielding fractions. The zero-field-cooled (ZFC) data of Fig. 3-1, taken with an applied field of 20 Oe parallel to the c-axis (before demagnetization correction), showed $T_c \simeq 85$ K

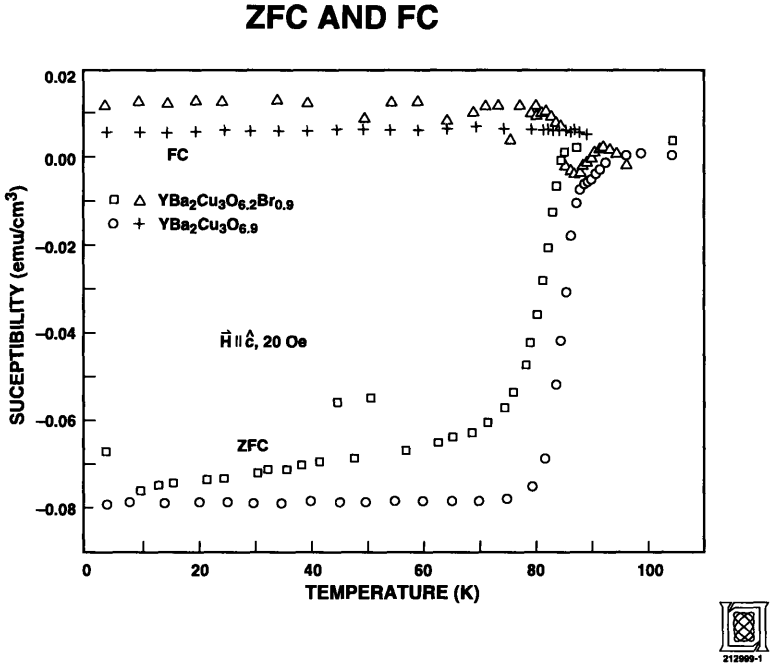

Figure 3-1: Susceptibility versus T as determined from SQUID measurements for a fully oxygenated $YBa_2Cu_3O_{6.9}$ single crystal sample (T_c = 85 K) and for a 24-hour brominated $YBa_2Cu_3O_{6.2}$ single crystal sample with a nominal stoichiometry $YBa_2Cu_3O_{6.2}Br_{0.9}$ [30] and T_c = 82 K. The applied magnetic field is along the $\hat{c}$-axis and has a magnitude of 20 Oe. Both field-cooled (FC) and zero-field-cooled (ZFC) data are shown.

and $\Delta T_c \simeq 4$ K with a shielding fraction $\simeq 100\%$ for the YBCO, and $T_c \simeq 82$ K and $\Delta T_c \simeq 20$ K with a shielding fraction $\simeq 97\%$ for the brominated YBCO-Br single crystals. (I define T_c determined by magnetization measurements to be the temperature where the slope of the susceptibility vs T curve is a maximum. ΔT_c is calculated from the 10% and 90% points.) Zero-field resistivity measurements (described below) yield $T_c \simeq 92$ K, $\Delta T_c \simeq 1$ K for both brominated and fully oxygenated YBCO single crystals.

The field-cooled (FC) temperature-dependent susceptibility data showed a small positive increase of the magnetization for both the YBCO and brominated YBCO-Br samples (see Fig. 3-1). This effect has been observed previously [31] and is believed to come from the flux-trapping capabilities of the materials and the nonuniform distribution of the magnetic field inside the SQUID [32].

It is appropriate at this time to mention the question of sample quality, which I believe has caused some confusion over the disparate results in the literature. Since the magnetically determined T_c for the Br-doped sample is lower than that for the pristine one, even though their transport T_c are about the same, the Br-doped sample is probably more inhomogeneous and impure. Results concluding that the bromine is incorporated in the lattice [22, 25, 33], and results indicating that the bromine (or chlorine) causes a decomposition of some parts of the sample, and a re-oxygenation of other parts [34], can both be found. It has been my experience that both types of reactions can occur, without yet determining which uncontrolled factors (e.g., bromine pressure, moisture, initial oxygen content and ordering, etc.) control the quality of the sample. The samples used here and in previous studies [24, 30] had shielding fractions near 100%, and a uniform bromine distribution as measured by Auger depth profiling, indicating that the bromine has been incorporated into the lattice. It appears that some of the samples used in the literature actually did show a decomposition, but this is clearly accompanied by shielding fractions that are far below 100%. We believe that the problem of understanding the bromination process is a separate issue from determining the position of the bromine (to be addressed in this chapter) which has been demonstrably incorporated into the lattice.

3.2.2 Experimental Procedure

To make the transport measurements, the samples were first mounted on mica with GE-varnish. To make good electrical contacts, I used an ion-milling technique whereby an aluminum mask was employed to expose only those areas where the silver contact pads were evaporated. The optimum ion milling parameters were: current $\simeq 42\mu$A, voltage $\simeq 3.5$ kV, and time $\simeq 4$ hours. The current was kept low to minimize heating, though the ion-milling time becomes much longer. The contact pads ($\sim 0.1 \times 0.1$ mm^2) were deposited and leads were attached using silver paint at the four corners of the sample. Whereas the contact resistance per pad for the YBCO was only on the order of 0.5 Ω, the contact resistance for the brominated YBCO was ~ 15 Ω. The contact resistance for both YBCO and YBCO-Br was found to decrease slightly as the temperature decreased from 300 K to 4.2 K.

The resistivity measurements with and without magnetic fields were made using a van der Pauw four-point probe method. With the magnetic field in the *ab* plane or along the *c* axis, but always perpendicular to most of the current, the magnetoresistance was measured for current flowing in the *ab* plane by sweeping the magnetic field from 0 to 14 Tesla in 20 minutes. Heating effects were avoided by operating at low current densities ($J \ll J_c$ where J_c is the critical current density). The resistivity measurements were checked for heating effects by increasing the current by a factor of 5 to 10, and observing no change in the measured ρ_{ab}. The reversibility of the ρ_{ab}-versus-H measurements was checked by sweeping the field both up and down.

The inductive critical current density of brominated YBCO was obtained by sweeping the applied field between -6 and 6 T at a fixed temperature, and using the Bean critical-state-model formula for $H \parallel \hat{c}$-axis [35, 36]

$$J_c = 30[M_+ - M_-]/D \tag{3.1}$$

where $M_+(M_-)$ is the measured magnetization for increasing (decreasing) field and D is the diameter of the in-plane surface of the sample. For $H \perp \hat{c}$-axis, a slightly

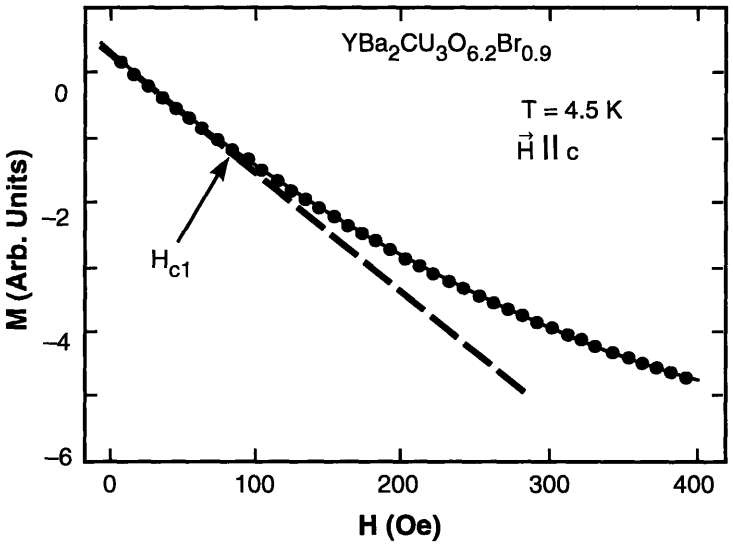

Figure 3-2: Magnetization of a $YBa_2Cu_3O_{6.2}Br_{0.9}$ single crystal as a function of field (before demagnetization corrections are applied) at 4.5 K for field perpendicular to the CuO_2 plane. The magnetic field at which the magnetization starts to deviate from the straight line is taken as the criterion for calculating H_{c1}. After demagnetization corrections are applied, the field value H_{c1} is about 10 times greater than that indicated by the arrow in the figure.

modified formula is used [36]

$$J_c = 20[M_+ - M_-]/d \tag{3.2}$$

where d is the sample thickness.

The lower critical field H_{c1} is defined to be the field (after applying the sample demagnetization correction) where the magnetization versus field curve starts to deviate from linearity. Figure 3-2 illustrates the criterion for determining H_{c1}. Using this criterion, H_{c1} versus T was determined.

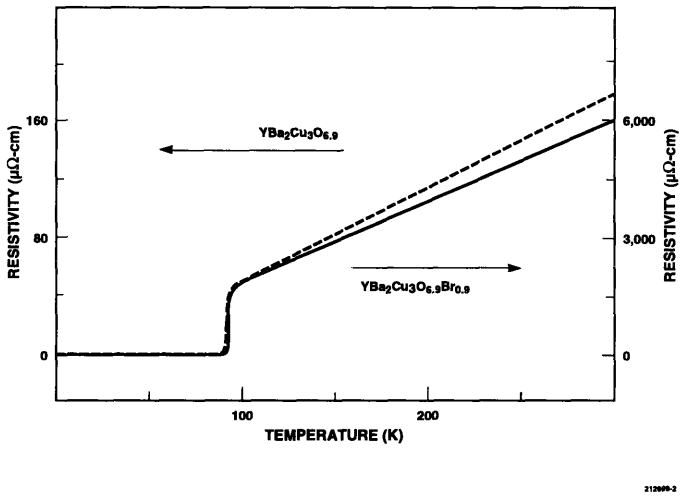

Figure 3-3: Measured $\rho(T)$ versus T for a single crystal $YBa_2Cu_3O_{6.2}Br_{0.9}$ ($T_c \simeq 92$ K) shown by the solid curve. For reference, $\rho(T)$ for a fully oxygenated $YBa_2Cu_3O_{6.9}$ ($T_c \simeq 92$ K) single crystal is also shown (dashed curve) to illustrate the approximately 35-fold increase in the normal state resistivity on bromination.

3.3 Zero-Field Transport

Results for the zero-field temperature-dependent resistivity $\rho(T)$ for the fully oxygenated $YBa_2Cu_3O_{6.9}$ and $YBa_2Cu_3O_{6.2}Br_{0.9}$ single crystals are shown in Fig. 3-3.

There is good agreement between our YBCO data for ρ vs T and the literature values for YBCO single crystals [37, 38]. With the 7 or 8 available contacts per sample, a set of 4 good contacts is selected. Our best YBCO-Br sample exhibited a zero field $\rho(T)$ curve similar to that for the $YBa_2Cu_3O_{6.9}$ single crystal used for the starting material, showing a linear T dependence for $\rho(T)$, except that the slope for $\rho(T)$ for the brominated sample (solid curve) is about 35 times larger than that for the starting material (dashed curve). Of the three other YBCO-Br samples, one also showed a linear dependence of $\rho(T)$ with a comparable slope. The remaining two samples which had been subjected to a prolonged acetone and ultrasonic cleaning process exhibited much larger ρ and non-linear $\rho(T)$ curves.

Despite the large increase in the normal-state resistivity for the brominated samples, they demonstrated almost the same T_c values and transition widths (ΔT_c). Note

that the two resistivity curves almost coalesce if I scale the brominated YBCO curve down $\simeq 35$ so that the scaled resistivity equals that of the pristine YBCO sample at $\sim$100 K. The room temperature resistivity value for our best brominated YBCO single crystal is accurate only to within 20% due to sample inhomogeneity and slightly nonuniform thicknesses. This value of resistivity for the brominated sample is considerably less than that quoted in Ref. [30] probably because the sample used there had been subjected to a prolonged acetone and ultrasonic cleaning process.

As will be discussed in Sect. 3.6, the carrier density in $YBa_2Cu_3O_{6.9}$ single crystals is between 2 and 3 times that in $YBa_2Cu_3O_{6.2}Br_{0.9}$. If I assume a Drude expression for the dc resistivity and assume that the effective mass remains the same upon bromination, I can estimate the resistivity for the brominated sample by

$$\frac{\rho_{Br}}{\rho_0} = \frac{n_0\tau_0}{n_{Br}\tau_{Br}} \simeq \frac{2.5\tau_0}{\tau_{Br}} \tag{3.3}$$

where ρ_0, n_0, τ_0 and ρ_{Br}, n_{Br}, τ_{Br} are the resistivity, carrier density, and scattering time of the fully oxygenated YBCO and the brominated YBCO single crystals, respectively. Since in this chapter I always consider the factor [carrier density/effective mass], the assumption that the effective mass is not changed by bromination can be relaxed by substituting the factor [carrier density/effective mass] for the quantity [carrier density] throughout the text. Experimentally, $\rho_{Br}/\rho_0 \simeq 35$ at room temperature. This leads us to conclude that bromination greatly increases the scattering rate.

One might argue that the increase of the scattering rate is caused by an increase in the number of impurities and grain boundaries after bromination. Impurities and grain boundaries, however, tend to give rise to only weakly temperature-dependent carrier scattering and hence should have little effect on the temperature dependence (i.e., the slope) of the normal-state resistivity. The 35-fold increase of the slope of $\rho(T)$ indicates that impurities and grain boundaries alone cannot account for the remarkable increase of the scattering rate.

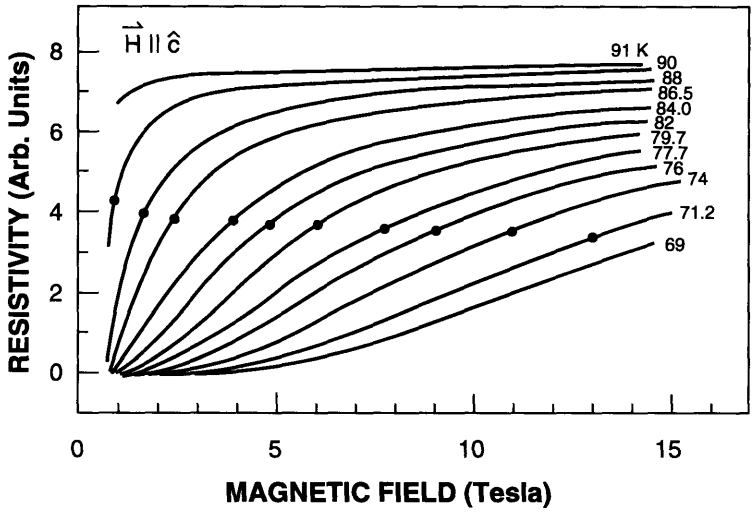

Figure 3-4: Magnetic field dependence of the resistivity for $H \parallel \hat{c}$-axis for a $YBa_2Cu_3O_{6.2}Br_{0.9}$ single crystal as a function of magnetic field for various temperatures from 69 K to 91 K. The 50% points which are taken as the upper critical field are marked with bullets.

3.4 Upper Critical Fields

The measured resistivity as a function of magnetic field (both parallel and perpendicular to the $\hat{c}$-axis) at various temperatures is shown in Figs. 3-4 and 3-5.

For each of the lowest temperatures (for either field orientation), the resistivity as a function of field rises from zero with an increasing slope up to some field value above which the slope starts to decrease. The higher-temperature curves seem to follow the same qualitative trend, except that their low-field zero-resistivity points are not shown due to a finite remanent value of the applied magnetic field in our superconducting magnet.

Although a sophisticated scaling procedure exists for uniquely determining the upper critical field H_{c2} from the fluctuation conductivity data [24], the conventional method, in which I define H_{c2} as the field where 50% of the normal-state resistivity is restored, has been shown to give about the same result for $H_{c2}(T)$ [24]. Moreover, I am mainly interested in the change, not the absolute value, of H_{c2} upon bromination. This change can be obtained by consistently applying the same criterion, whether the

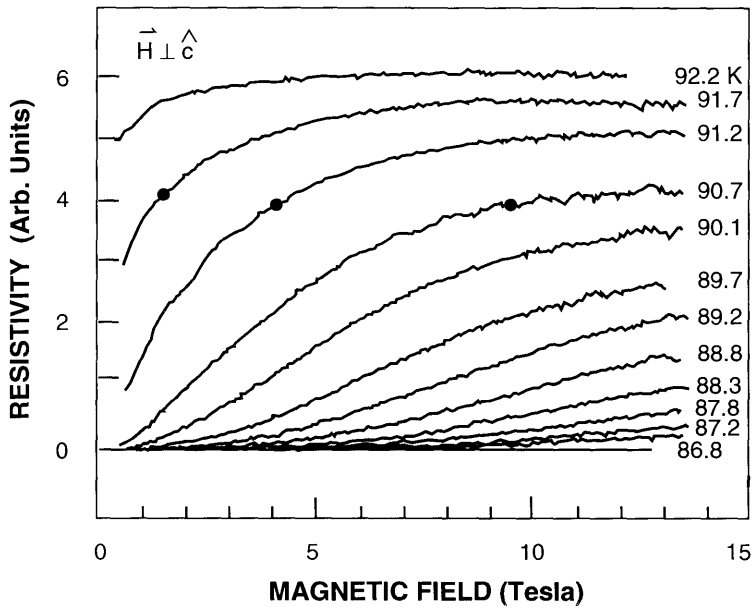

Figure 3-5: Magnetic field dependence of the resistivity for $H \perp \hat{c}$-axis for a single crystal $YBa_2Cu_3O_{6.2}Br_{0.9}$ sample as a function of magnetic field for various temperatures from 86.8 K to 92.2 K. The 50% points which are taken as the upper critical field are marked with bullets.

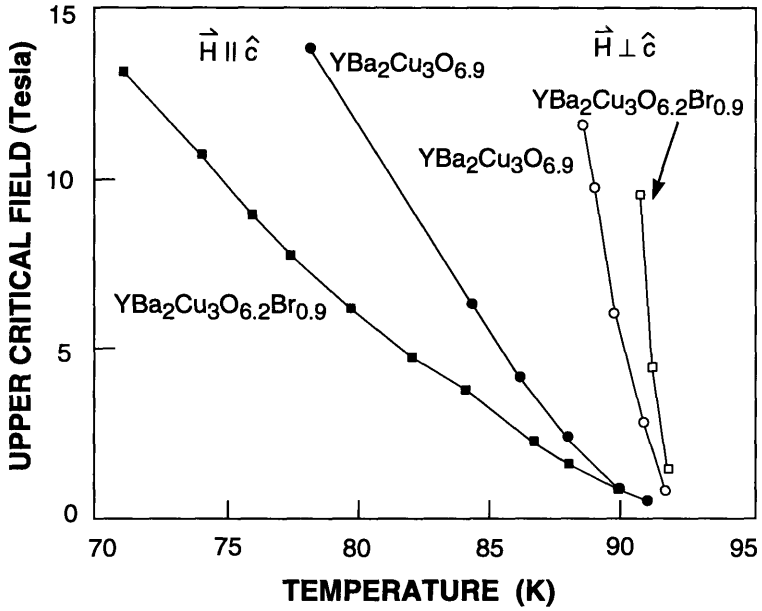

Figure 3-6: Upper critical fields $H_{c2}^{\parallel}$ (solid circles and squares) and $H_{c2}^{\perp}$ (open circles and squares) versus T for $YBa_2Cu_3O_{6.9}$ (circles) and $YBa_2Cu_3O_{6.2}Br_{0.9}$ (squares) single crystals.

simple resistive method or the elaborate fluctuation-scaling procedure, to both the pristine and the brominated samples. Employing the resistive method, the calculated values for $H_{c2}(T)$ versus T are plotted in Fig. 3-6 and these results are compared with those from the same batch of $YBa_2Cu_3O_{6.9}$ single crystals before de-oxygenation.

The results of Fig. 3-6 show that bromination increases $H_{c2}^{\perp}$ (with $H \perp \hat{c}$-axis), but decreases $H_{c2}^{\parallel}$ (with $H \parallel \hat{c}$-axis).

To obtain an estimate for the $T = 0$ values for $H_{c2}(0)$, I use the WHH (Werthamer, Helfand and Hohenberg) expression [39]

$$H_{c2}(0) = 0.69 \left(\frac{dH_{c2}}{dT} \right) T_c'. \tag{3.4}$$

Referring to Fig. 3-6, the slope in Eq. 3.4 is taken to be tangent to the $H_{c2}(T)$ curve at the highest available field (14 T) for our measurements and T_c' is the intersection of this tangent with the temperature axis. The results for $H_{c2}(0)$ for the brominated and pristine samples are given in Table 3.2 for the two magnetic field orientations.

Table 3.2: Parameters deduced from analysis of the critical field measurements.

	YBCO			Br-YBCO
Parameter[a]	This work	Iye[b]	Moodera[c]	This work
$H_{c2}^{\parallel}(0)$	78 T	118 T	61 T	53 T
$\xi_{ab}(0)$	21 Å	17 Å	23 Å	25 Å
$H_{c2}^{\perp}(0)$	313 T	510 T	222 T	776 T
$\xi_c(0)$	5.1 Å	3.9 Å	<6.3 Å	1.7 Å

(a) H defined at 50% ρ_n
(b) Ref. [40].
(c) Ref. [41].

The in-plane and $\hat{c}$-axis coherence lengths at $T = 0$, $\xi_{ab}(0)$ and $\xi_c(0)$, respectively, [40, 41] are estimated from the relations derived from the effective-mass model based on the anisotropic Ginzburg-Landau (GL) theory

$$H_{c2}^{\parallel}(0) = \frac{\phi_0}{2\pi\xi_{ab}^2(0)} \tag{3.5}$$

and

$$H_{c2}^{\perp}(0) = \frac{\phi_0}{2\pi\xi_{ab}(0)\xi_c(0)} \tag{3.6}$$

where ϕ_0 is the flux quantum. The results for $\xi_{ab}(0)$ and $\xi_c(0)$ are likewise listed in Table 3.2.

Using the effective-mass model, I relate the H_{c2} anisotropy to the effective-mass anisotropy by

$$\frac{H_{c2}^{\perp}}{H_{c2}^{\parallel}} = \frac{\xi_{ab}}{\xi_c} = \left(\frac{m_c}{m_{ab}}\right)^{1/2}. \tag{3.7}$$

Our results from Table 3.2 yield a ratio $r = \xi_{ab}(0)/\xi_c(0) \sim 14.6$ and ~ 4.0 for the brominated and pristine YBCO single crystals, respectively. I thus see that bromination has increased the anisotropy of $\xi(0)$ (and $H_{c2}(0)$) by a factor of ~ 3.6. From Eq. 3.7, I estimate the corresponding changes in the anisotropy of the effective masses upon bromination to be a factor of $\sim$13, as compared with $\sim$4 for the pristine sample.

More specifically, bromination reduces $\xi_c(0)$ by a factor of 3, but leaves $\xi_{ab}(0)$ (or the CuO_2 planes) relatively unaffected. This suggests that Br doesn't enter the CuO_2 planes. This conclusion is consistent with the findings of Amitin et al.[25] that Cl in YBCO occupies the three positions O(5), O(4) and O(1), all away from the CuO_2 planes.

3.5 Pinning Potentials

From the data of Figs. 3-4 and 3-5, the pinning energy $U(T, B)$ can be obtained using the thermally activated flux motion relation [42, 43]

$$U(T, B) = k_B T \ln\left(\frac{\rho_0}{\rho(T)}\right) \tag{3.8}$$

where ρ_0 is estimated as $\rho_0 = \rho(T_0)$ and T_0 is taken to be the onset of superconductivity [43].

The uncertainty in T_0 introduces a small systematic error, but this error does not significantly affect our comparison of $U(T, B)$ between the pristine and brominated YBCO single crystals. Figures 3-7a and b show such a comparison as a function of field for $H \parallel \hat{c}$ at $T = 89.2$K and $H \perp \hat{c}$ at $T = 76.0$K, respectively. The horizontal lines correspond to $U \sim k_B T$ and indicate the crossover between the thermally activated dissipation (upper) and the flux flow (lower) regions. Note that no data points are given in the flux flow region since Eq. 3.8, which describes thermally activated flux motion, no longer applies here. Similarly, Figs. 3-8a and b compare the pinning energies as a function of temperature at 5T for both field orientations. Again, flux flow and thermally activated dissipation dominate the regions below and above the straight lines $U \sim k_B T$, respectively.

From Figs. 3-7a and 3-8a, bromination appears to decrease the pinning energy for vortices aligned along the $\hat{c}$ axis. A possible explanation for the pinning-potential reduction is the increase of anisotropy [44] discussed above. Since

$$U = J_c B R_c^2 L_c r_p \tag{3.9}$$

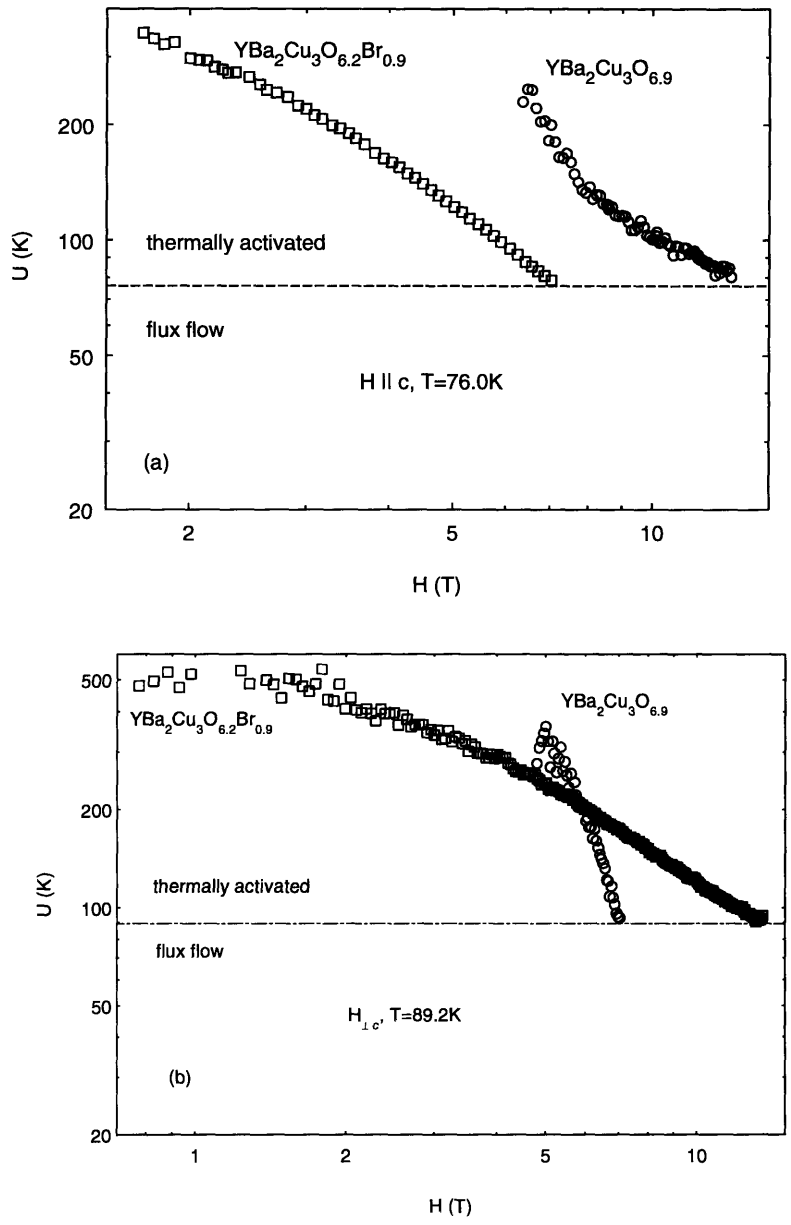

Figure 3-7: (a) The field dependence at 76.0 K of the activation energy U for flux motion in the ab plane ($H \parallel c$) derived from the resistivity data for $YBa_2Cu_3O_{6.9}$ (open circles) and $YBa_2Cu_3O_{6.2}Br_{0.9}$ (open squares) single crystals. The horizontal dashed line $U(T) = k_BT$ separates the flux flow from the thermally activated flux motion regions. (b) The corresponding field dependence at 89.2 K of the activation energy for the flux motion perpendicular to the ab plane ($H \perp c$).

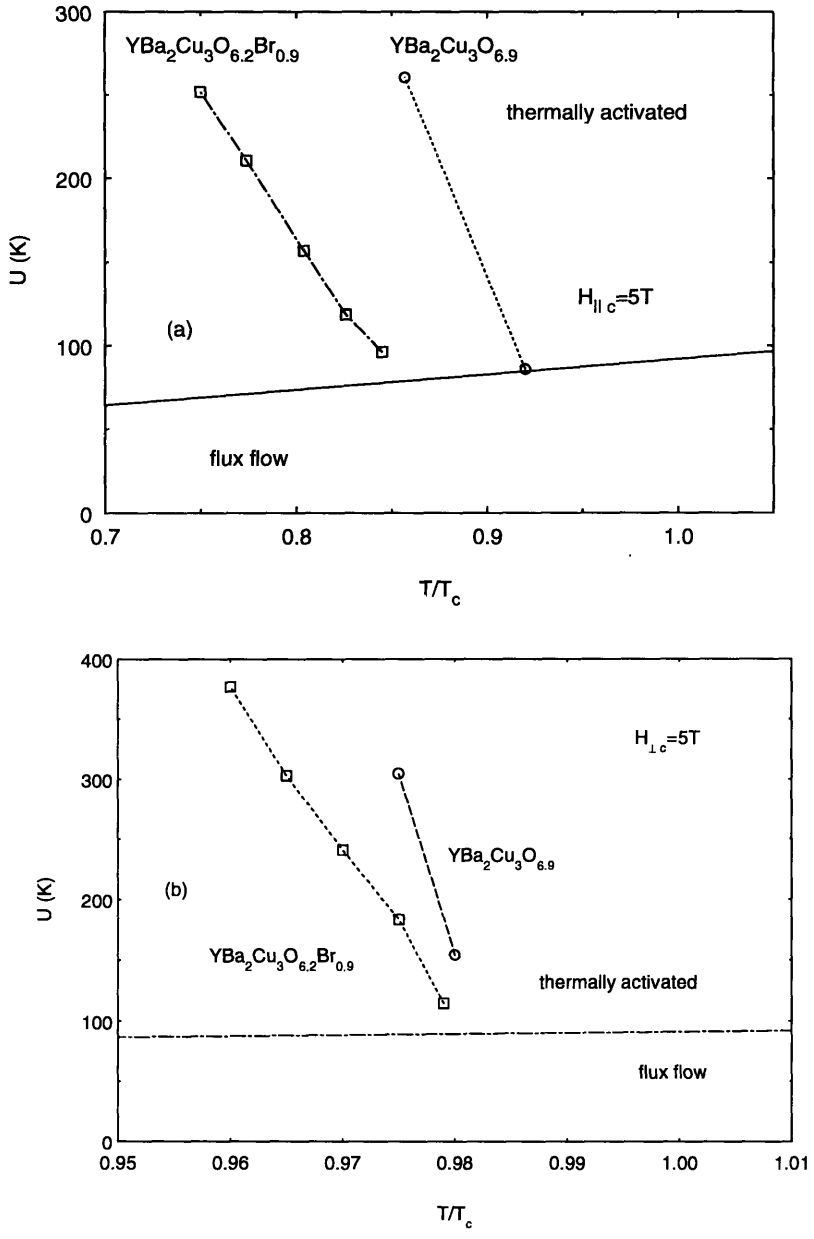

Figure 3-8: (a) The temperature dependence at 5 T ($H \parallel c$) of the activation energy for the flux motion in the ab plane derived from the resistivity data for $YBa_2Cu_3O_{6.9}$ (open circles) and $YBa_2Cu_3O_{6.2}Br_{0.9}$ (open squares) single crystals. The broken line denoting $U(T) = k_BT$ separates the flux flow from the thermally activated flux motion regions. (b) The corresponding temperature dependence at 5 T (for $H \perp c$) of the activation energy for flux motion perpendicular to the ab plane.

where r_p is the range of the pinning potential, R_c is the correlation length of the vortices in the ab plane, and L_c is the correlation length along the vortex, higher anisotropy or shorter correlation length means smaller pinning energy, assuming the other parameters r_p, R_c and J_c remain the same in the ab plane. (J_c in the ab plane, as shown in Sect. 3.6, is in fact smaller at high field for the brominated YBCO samples, reducing the pinning potential even further.)

For magnetic fields parallel to the ab plane, the anisotropy argument is inapplicable, since the pinning mechanism is different and is believed to arise from the strong modulation of the order parameter in the direction perpendicular to the layers [45]. As a result, the pinning energy for vortex motion perpendicular to the layers doesn't always increase for the more anisotropic brominated YBCO samples. In fact, as shown in Figs. 3-7b and 3-8b, the pinning potential is smaller than that of the fully oxygenated YBCO single crystals at low temperature and field.

3.6 Magnetization Measurements

Figures 3-9 and 3-10 present the critical current density J_c calculated from the magnetization hysteresis data, using the modified Bean critical-state model for magnetic field parallel and perpendicular to the $\hat{c}$-axis.

Compared with J_c of a fully oxygenated YBCO single crystal shown in the inset of Fig. 3-9 [46], the J_c values of our brominated YBCO single crystals are noticeably suppressed, especially at higher fields and temperatures.

Moreover, J_c for the brominated samples exhibits a much stronger dependence on H than for the fully oxygenated samples. Note that since the resistivity for the brominated YBCO becomes too low to be measured conveniently for the temperature and field range considered in Figs. 3-9 and 3-10, the corresponding pinning energies in this range are unavailable for comparison with the J_c values presented here.

Figure 3-11 plots the measured lower critical field H_{c1} versus temperature of a brominated YBCO single crystal. The inset shows the corresponding result by Lan et al.[31] on a fully oxygenated YBCO single crystal for H parallel to the $\hat{c}$-axis. The

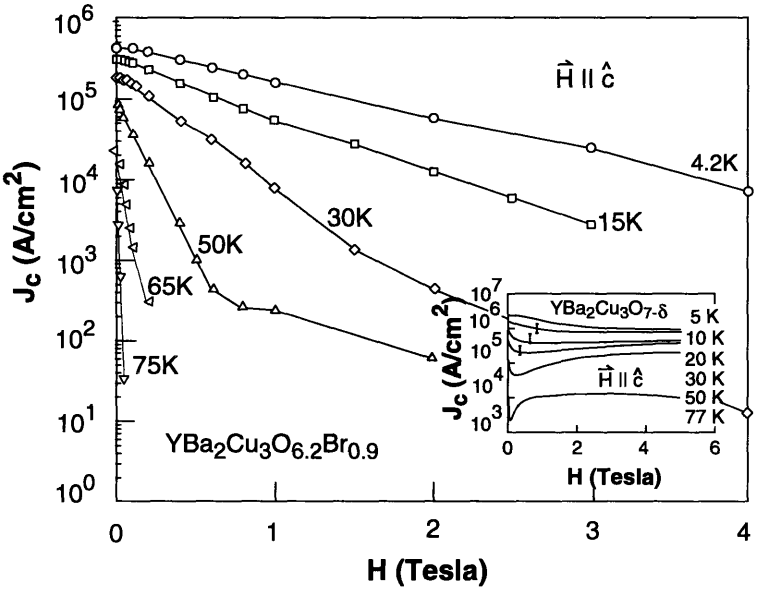

Figure 3-9: The field dependence of the inductive critical current density in a $YBa_2Cu_3O_{6.2}Br_{0.9}$ single crystal at various temperatures for fields parallel to the $\hat{c}$-axis. The solid lines are guides for the eye. The inset shows the corresponding field dependence data for a $YBa_2Cu_3O_{7-y}$ single crystal by Lan et al.[46].

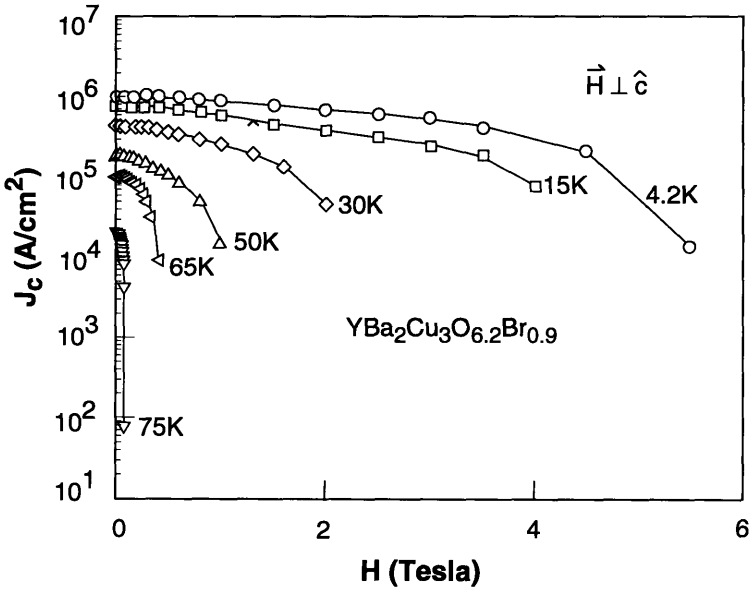

Figure 3-10: The field dependence of the inductive critical current density in a $YBa_2Cu_3O_{6.2}Br_{0.9}$ single crystal at different temperatures for fields perpendicular to the $\hat{c}$-axis. The solid lines are guides for the eye.

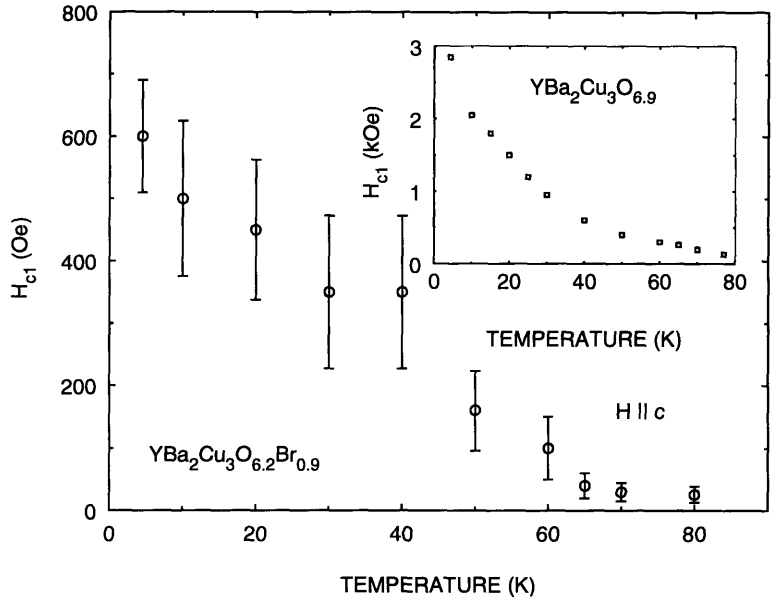

Figure 3-11: The temperature dependence of the lower critical field H_{c1} for $H \parallel c$ axis for a $YBa_2Cu_3O_{6.2}Br_{0.9}$ single crystal. The inset shows the corresponding data for a $YBa_2Cu_3O_{7-y}$ single crystal by Lan et al.[31].

anomalous upturn of H_{c1} at low temperature ($T < 50$ K) for both the fully oxygenated and the brominated YBCO single crystals can be attributed to the appearance of low-temperature surface barriers [47].

For the high-temperature regime ($T > 50$ K), using the relation derived from the anisotropic GL theory [11]

$$H_{c1} \sim \frac{\Phi_0}{4\pi\lambda_{ab}^2} \tag{3.10}$$

where λ_{ab} is the penetration depth for $H \parallel \hat{c}$-axis and Φ_0 the flux quantum, the value of $(H_{c1}^{\mathrm{YBCO}}/H_{c1}^{\mathrm{YBCO-Br}})$ between 2 and 3 implies that

$$2 \leq \left(\frac{\lambda_{ab}^{\mathrm{YBCO-Br}}}{\lambda_{ab}^{\mathrm{YBCO}}}\right)^2 \leq 3. \tag{3.11}$$

From the relation $\lambda_{ab}^2 \propto m_{ab}/n_s$ [11], with m_{ab} the effective mass in the ab plane, and n_s the density of the superconducting electrons which is taken to be equal to the carrier densities n_0 and n_{Br} for the pristine and brominated YBCO samples,

respectively, I get

$$\frac{1}{2} \geq \left(\frac{n_{\mathrm{Br}}}{n_0}\right) \geq \frac{1}{3} \tag{3.12}$$

assuming m_{ab} is the same. The reduction of the carrier density in Eq. 3.12 by a factor of 2 to 3 by bromination is consistent with the observed equivalent decrease in the plasma frequency (from ~10,000 cm^{-1} to ~6,000 cm^{-1})[30]. It is interesting to point out that even though the superconducting carrier density is reduced by more than a factor of 2, the corresponding T_c is unaffected for the brominated single crystals relative to the pristine YBCO samples. This lack of variation in T_c as the carrier density significantly decreases is consistent with the well-known plateau observed in T_c of oxygen-deficient $YBa_2Cu_3O_{7-x}$ [48, 49] for $0 \leq x \leq 0.12$ where $\delta = 0.12$ corresponds to a decrease in the carrier density by a factor of ~2 [50].

3.7 Summary

Bromination of de-oxygenated YBCO single crystals increases the scattering rate as well as the anisotropy. The relative lack of variation of $\xi_{ab}(0)$ and the reduction of $\xi_c(0)$ by a factor of 3 upon bromination of YBCO suggest that Br never enters the CuO_2 planes. The pinning energy for vortex motion in the *ab* plane decreases after bromination and this decrease can be attributed to the increased anisotropy which is measured independently. For vortex motion along the $\hat{c}$ axis, however, the pinning energy decreases or increases depending on temperature and field. Bromination suppresses J_c and makes it strongly dependent on the applied magnetic field. At high temperature, the H_{c1} in the brominated YBCO single crystals indicates a reduction in carrier density (by a factor of between 2 and 3) which is consistent with the observed reduction in the plasma frequency [30].

Chapter 4

Microwave Measurement Techniques

4.1 Introduction

Surface impedance is an important material parameter. Besides its importance in technical applications, surface impedance can offer insight into the superconducting properties of a sample. Surface-impedance measurement is one of the most sensitive techniques for probing a superconductor in its superconducting phase. In the following, I review the definition and physical meaning of surface impedance Z_s. I next describe the stripline resonator, the device I use throughout this thesis to perform my microwave measurements, and show how Z_s can be obtained from the quality factor Q and the resonant frequency f_0 of the resonator. Then, I discuss the complications arising from the nonlinearity of Z_s at high microwave power.

4.2 Surface Impedance Z_s

Consider a plane electromagnetic wave incident normally on a planar surface as shown in Fig. 4-1. For a conducting surface, in general, most of the wave gets reflected while some of it penetrates the conducting medium up to a distance of the order of the skin depth of the material. The electric and magnetic fields at the surface depend on the

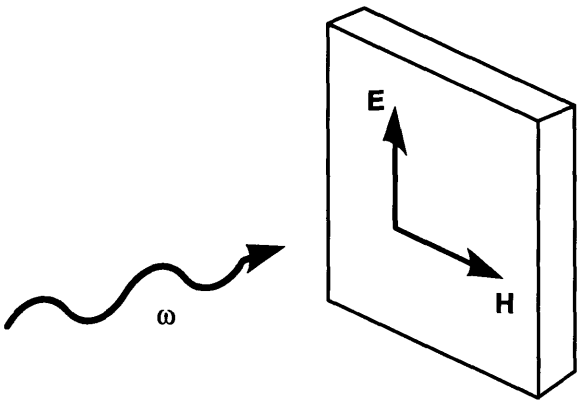

Figure 4-1: Plane electromagnetic wave impinging normally on a planar surface creating surface electric field E perpendicular to surface magnetic field H. $Z_s \equiv E/H$.

properties of the material. The surface impedance Z_s is defined by

$$Z_s \equiv E/H = R_s + jX_s \tag{4.1}$$

where the surface resistance R_s determines the dissipation and the surface reactance X_s measures the energy stored in the medium.

If the material is a normal conductor, it is in the local limit if its electron's mean free path is short compared to the skin depth. Similarly, if the material is a superconductor, the local limit is achieved when the coherence length ξ is short compared with the penetration depth λ. From Maxwell's equations, in the local limit,

$$Z_s = \sqrt{j\mu_0\omega\rho} \simeq \sqrt{\frac{\mu_0\omega}{\sigma_2}}\left(\frac{\sigma_1}{2\sigma_2} + j\right) \quad \text{for } \sigma_1 \ll \sigma_2 \tag{4.2}$$

where the (uniform) complex resistivity $\rho = 1/\sigma$ with the complex conductivity $\sigma = \sigma_1 - j\sigma_2$.

At the microwave frequencies, the high-T_c $YBa_2Cu_3O_{7-x}$ superconductor is in the local limit in the normal phase. In the superconducting phase, it is strongly local also since $\xi(< 20\mathring{A}) \ll \lambda(> 1400\mathring{A})$. Similarly, the conventional superconductor NbN considered in this thesis is also in the local limit both for the superconducting phase

with $\xi(\sim 350\mathring{A}) \ll \lambda(\sim 3700\mathring{A})$ and the normal phase. Hence, the nonlocal or the anomalous skin-depth effects need not be considered here.

Almost all superconductors have $\sigma_1 \ll \sigma_2$ at most temperatures below T_c. Consequently, from Maxwell's equations,

$$\sigma_2 = 1/\mu_0\omega\lambda^2.$$

At frequencies (e.g., microwave frequencies) much less than the superconducting gap frequency, Eq. (4.2) can be simplified to

$$Z_s \simeq \frac{1}{2}\mu_0^2\omega^2\lambda^3\sigma_1 + j\mu_0\omega\lambda \quad \text{for } \sigma_1 \ll \sigma_2 \text{ or } R_s \ll X_s. \tag{4.3}$$

Note that $R_s \propto \omega^2$ for a superconductor in contrast to $R_s \propto \omega^{1/2}$ for a normal metal (with real resistivity ρ) in the local limits. Furthermore, $X_s \propto \lambda$ at a fixed frequency.

For anisotropic superconductors such as high-T_c materials, the scalar Eq. (4.1) needs to be generalized to a tensor relation. Since I will consider only the cases in which the fields lie along the principal axes, however, the tensorial surface impedance is diagonalized and the scalar relation is adequate.

4.3 Stripline Resonator

The surface impedance $Z_s = R_s + jX_s$ can be measured by various kinds of resonators: transmission-line resonators such as parallel-plates, stripline, microstrip, and coplanar; and cavity resonators. My measurements of Z_s have been performed using the stripline resonator.

Figure 4-2 shows the stripline resonator structure which consists of a center superconducting line sandwiched between two superconducting ground planes often of the same superconducting material. The center line is an isolated section of a transmission line, coupled capacitively to the external circuit by two end gaps. The wavelength of the fundamental resonant mode is twice the length of the center line. Overtone resonances occur at multiples of the fundamental frequencies. The lengths of the

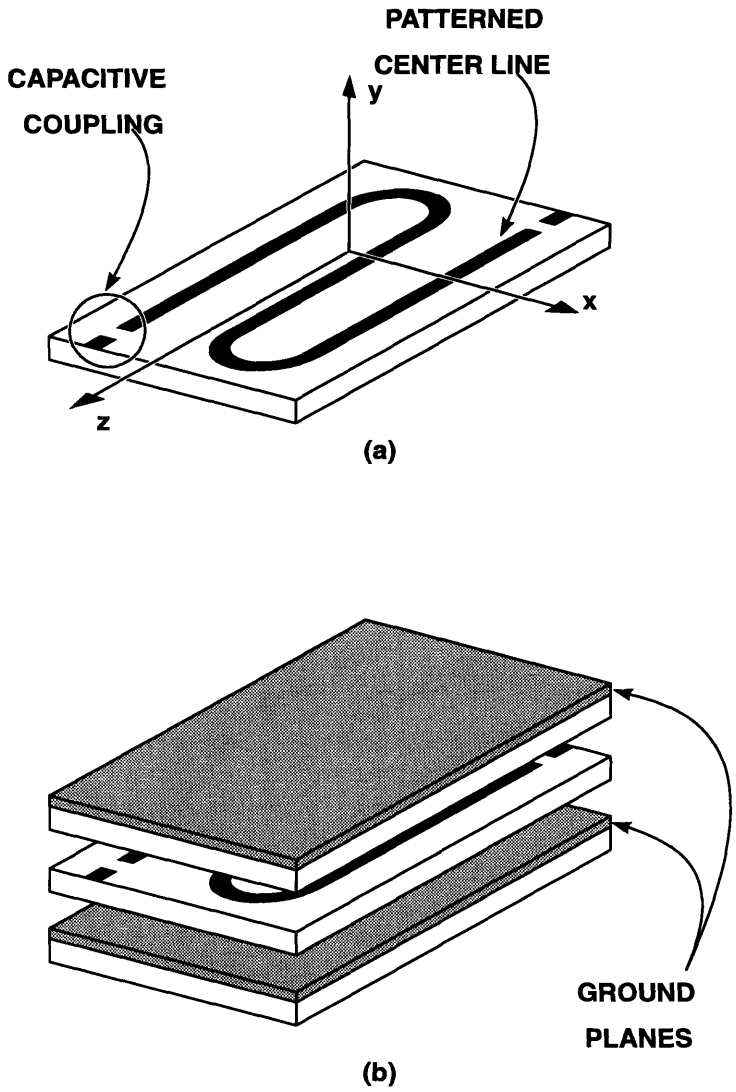

Figure 4-2: Stripline resonator. (a) Center line on substrate. The rf current flows along the line (z-direction). (b) Center line and ground planes.

center line were chosen to yield a fundamental frequency of $\sim$ 1.5 GHz for YBCO films and of $\sim$ 0.5 GHz for NbN films. With a width of the center line of 150 μm, the transmission-line characteristic impedances Z_0 are 34 Ω for $LaAlO_3$ ($\epsilon = 25$) and 50 Ω for sapphire ($\epsilon = 10$) dielectrics. Measurements of the surface resistance using the stripline-resonator technique produce an ultimate sensitivity of lower than 10^{-7} Ω, as demonstrated with niobium films at 4.2 K [51]. This sensitivity corresponds to a quality factor Q of 10^6 at 0.5 GHz. All the center line, the upper and lower ground planes, and the substrates are enclosed inside a gold-plated copper package with rf connectors. We have chosen the stripline resonator because it offers several advantages: The stripline resonator has the highest Q among the transmission-line resonators since it suffers no energy loss through radiation. The upper and lower ground planes not only eliminate radiation losses, they also confine the field almost completely from stray coupling to other lossy nonsuperconducting conductors. The narrow line geometry of the stripline concentrates the current and field, facilitating nonlinear measurements with relatively low input power. For instance, in a 50 Ω stripline resonator, an input power of only 0 dBm can produce a current density of 10^7 A/cm^2 when $Q = 10^6$ and a corresponding peak magnetic field at the surface of greater than 100 Oe. Such a large rf field amplitude is difficult to achieve in cavity measurements. Finally, the different modes of the stripline resonator allow for studies of the frequency dependence of the samples.

Substrate selection is important for transmission line resonators because rf fields penetrate the substrates on which the center conductor and the upper ground plane are deposited, inducing dielectric losses. For the YBCO films I measured, $LaAlO_3$ substrates are used because of their lower (real) dielectric constant and lower microwave losses than $SrTiO_3$, and better lattice matching than MgO. The NbN films are deposited on sapphire.

After being patterned with standard photolithography, the YBCO and NbN films are etched with 0.25% phosphoric acid and reactive ion etching in a CFC plasma, respectively.

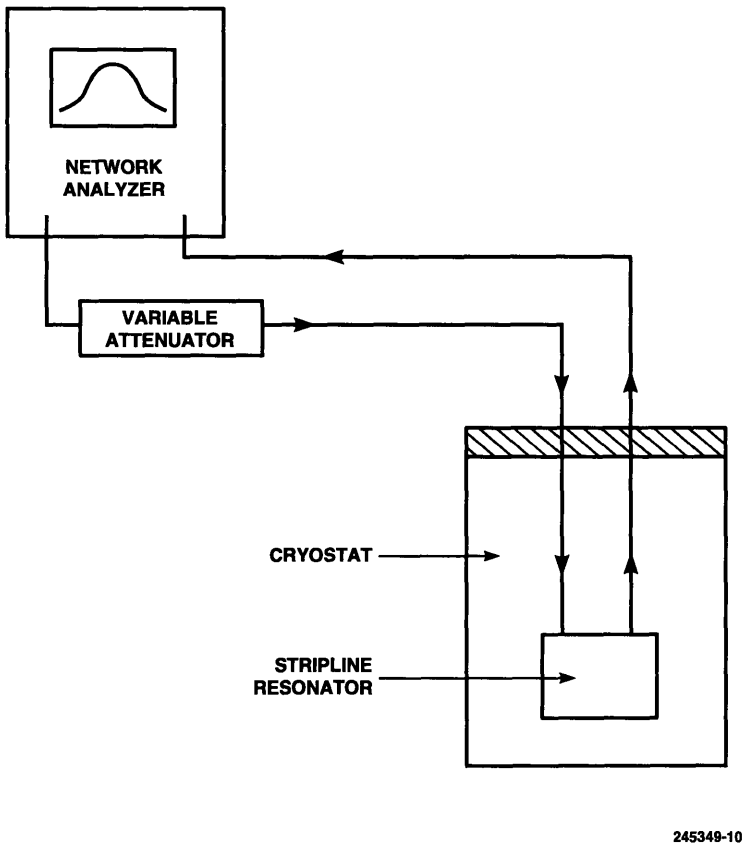

Figure 4-3: Setup for measurement of Z_s at low microwave field.

4.4 Measurement of Z_s at Low Microwave Field

The setup for measurement of Z_s at low microwave field is shown schematically in Fig. 4-3. The stripline resonator is connected to a vector network analyzer (Hewlett Packard 8720B Network Analyzer, 130 MHz – 20 GHz) which supplies the power and measures both the amplitude and phase of the transmitted rf wave. The power level is controlled by both the network analyzer and the attenuator. The low rf field limit is usually achieved for rf powers less than -20 dBm. The calibrated insertion loss can be obtained by subtracting from the apparent insertion loss the attenuation of the circuit. At low power, the resonant curve is Lorentzian in shape, and the loaded Q is given by $f_0/\delta f_0$ where f_0 is the peak of the resonant curve and δf_0 is the 3-dB bandwidth.

4.4.1 Current Distribution

Using the London equations together with Maxwell's equations, the current distribution in the cross-sectional area of the stripline has been calculated numerically based on a modification of the Weeks [52] method, and incorporating a complex conductivity to describe the superconductor. From the current distribution, the inductance per unit length and the resistance per unit length of the conductors can be calculated for a particular geometry and as a function of penetration depth λ. For small λ/t where t is the film thickness, the inductance and the relation between Q and R_s are nearly independent of λ.

As is the case for any transmission-line geometry, in the cross-sectional xy plane of the superconducting stripline (Fig. 4-2), the rf current density peaks at the surfaces, edges, and corners [53]. For the superconducting YBCO stripline in the frequency range that was considered in this work ($1 < f < 17$ GHz), the Meissner effect dominates over the classical skin-depth effect in determining the depth of the rf field penetration. At 77 K and 1 GHz, by taking the normal resistivity ρ_n to be 50 $\mu\Omega$ cm, the skin depth is estimated to be 11.4 μm, which is much larger than the effective magnetic penetration depth ($\lambda \sim 0.3$ μm). The scale of the rf current peaks in the cross-sectional area of the stripline resonator at the microwave frequencies considered here is hence determined by λ (except at temperatures very close to T_c, which are not considered here, where λ exceeds the skin depth). The current density is highly nonuniform, especially in the center conductor where the currents are crowded to the edges with the scale of the penetration from the edge determined by λ. The smaller the λ, the more strongly peaked at the edges the currents are. The current in the ground plane is much more uniform and about ten times wider than in the center conductor. Consequently, the largest contribution to the losses comes from the center conductor since losses are proportional to the square of the current density [54].

With the calculated inductance L and resistance R per unit length values, both λ and R_s of the superconductors can be extracted from the measured resonant frequency and Q of the stripline resonator. The peak rf self-field $H_{\rm rf}$ at the edges can also be calculated from the current distribution.

4.4.2 Penetration Depth

The λ is determined by measuring the temperature dependence of the fundamental resonant frequency of the resonator and fitting a model of the temperature dependence of λ to the data. The resonant frequency is proportional to $1/\sqrt{L}$ where L is the inductance per unit length. The inductance is a function of the penetration depth which, in turn, is a function of the temperature. Thus, as a function of temperature, the resonant frequency $f(T)$ is given by

$$f(T) = f_0(T_0)\sqrt{\frac{L[\lambda(T_0)]}{L[\lambda(T)]}}$$

where $L(\lambda)$ can be calculated from the current distribution, and T_0 is a reference temperature. The penetration depth is assumed to follow a two-fluid model's temperature dependence

$$\lambda(T) = \frac{\lambda(0)}{\sqrt{1-(T/T_c)^4}}.$$

A more accurate temperature dependence of $\lambda(T)$ can be obtained from the Mattis-Bardeen [55] theory for the surface impedance of a superconductor. The two-fluid and the Mattis-Bardeen temperature dependences produce curves of $f(T)/f(T_0)$ which are nearly indistinguishable if calculated with slightly different values of $\lambda(0)$.

Figure 4-4 shows measurements on a NbN film of thickness 0.8 μm with the best fit to calculations using $\lambda(T)$ computed from the Mattis-Bardeen expression with $\lambda(0)$ as a free parameter. The best fit is achieved with $\lambda(0) = 0.387\mu$m. Figure 4-5 presents similar measurements on a $YBa_2Cu_3O_{7-x}$ film 0.3 μm thick. The two-fluid model is used to model the temperature dependence. The best fit yields $\lambda(0) = 0.167\mu$m. The fit shows some deviation from the two-fluid model, as others have reported [56]. This method of determining λ has an approximate accuracy of 20% and is model dependent. The inferred value of λ shows high sensitivity to the value of T_c chosen. For example, a shift of 0.1 K in T_c can change $\lambda(0)$ by up to 10%.

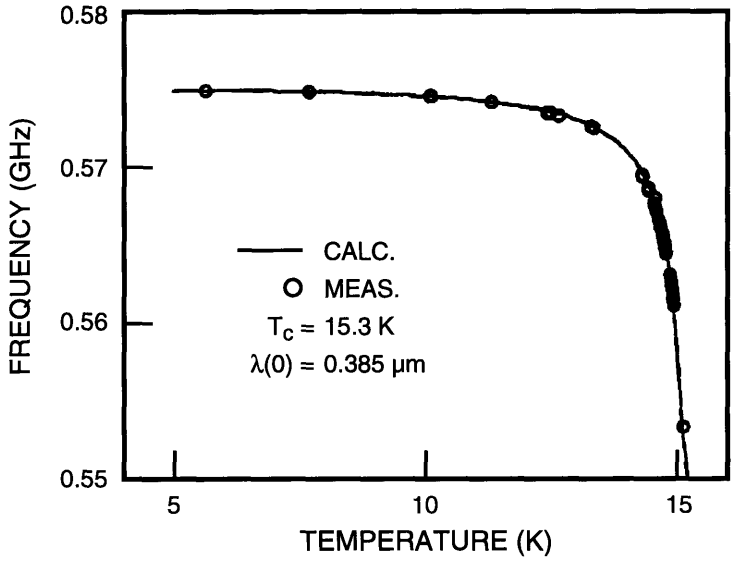

Figure 4-4: Determination of the penetration depth of NbN from resonance frequency versus temperature, measured and calculated values. Film thicknesses $t = 0.8\mu$m.

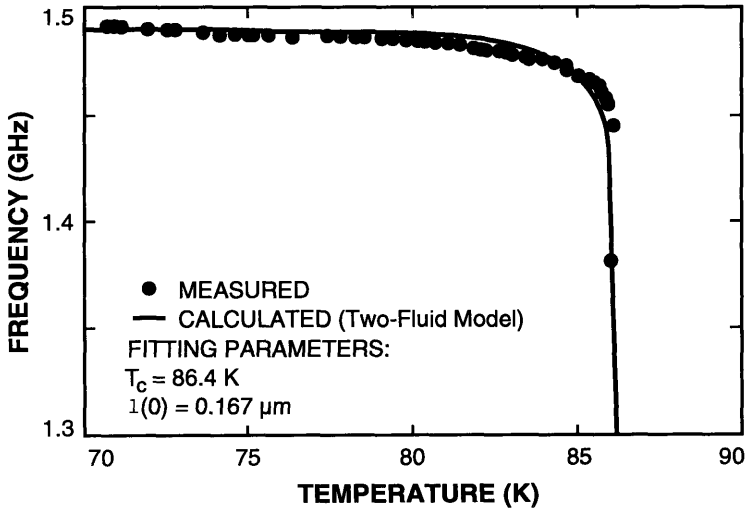

Figure 4-5: Measured and calculated values of resonant frequency of the fundamental mode of the resonator versus temperature for a $YBa_2Cu_3O_{7-x}$ film. The calculated values use the two-fluid model. The best fit is obtained with $\lambda(0) = 0.167\mu$m and $T_c = 86.4$ K.

4.4.3 Surface Resistance

With the λ determined via fitting to the temperature dependence of the resonant frequency, the imaginary part σ_2 of the complex conductivity and the inductance per unit length L can be calculated. The resistance R per unit length can be obtained from L and the measured Q, by the relation $Q = \omega L/R$. The real part σ_1 of the complex conductivity can then be calculated from R and λ. The surface resistance is given by $R_s = \omega^2\mu^2\sigma_1\lambda^3/2$, where μ is the magnetic permeability. For small λ/t, the relationship between Q and R_s is independent of λ and

$$R_s = \Gamma f/Q \tag{4.4}$$

where the geometrical factor $\Gamma = 0.41\Omega/\text{GHz}$ for the stripline geometry used in this thesis. When λ/t becomes comparable to unity, Eq. (4.4) must be modified to

$$R_s = \frac{\Gamma f}{Q\Delta(\lambda/t)} \tag{4.5}$$

where $\Delta(\lambda/t)$ is a correction factor to take into account the dependence of R and L on λ.

4.5 Measurement of Z_s at High Microwave Field

Figure 4-6 shows schematically the setup for measurement of Z_s at high microwave powers. The setup is similar to that for low microwave powers, except that a high frequency amplifier is inserted to boost the input power. The power dependence of Z_s is measured by stepping the value of the variable attenuator. In general, it is more desirable to know the dependence of Z_s on the microwave current instead of the input power. The microwave current can be calculated directly from the Q, the insertion loss of the resonator, and the incident power, as discussed below.

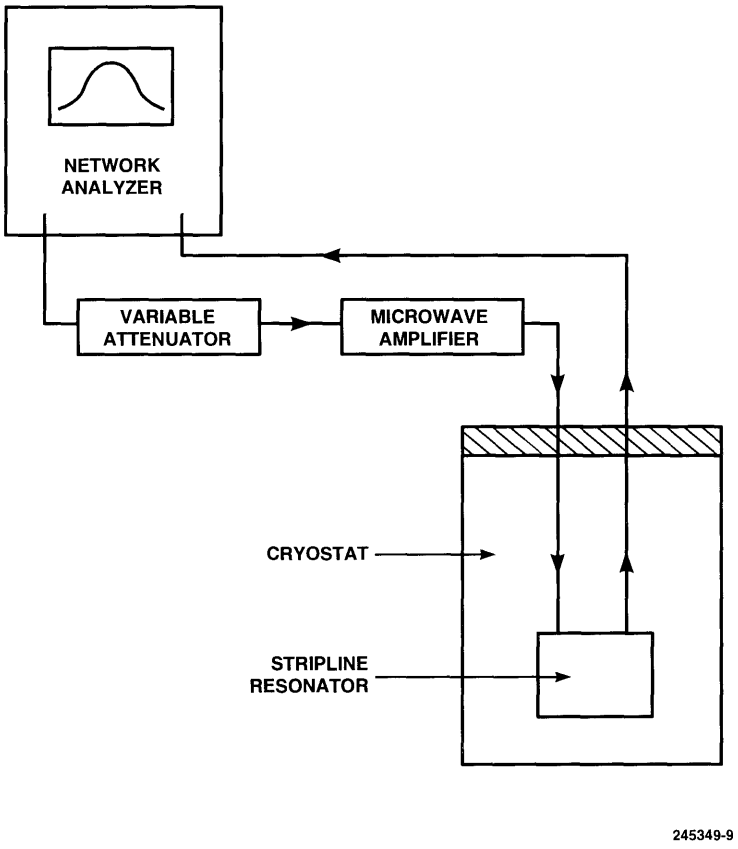

Figure 4-6: Setup for measurement of Z_s at high microwave fields.

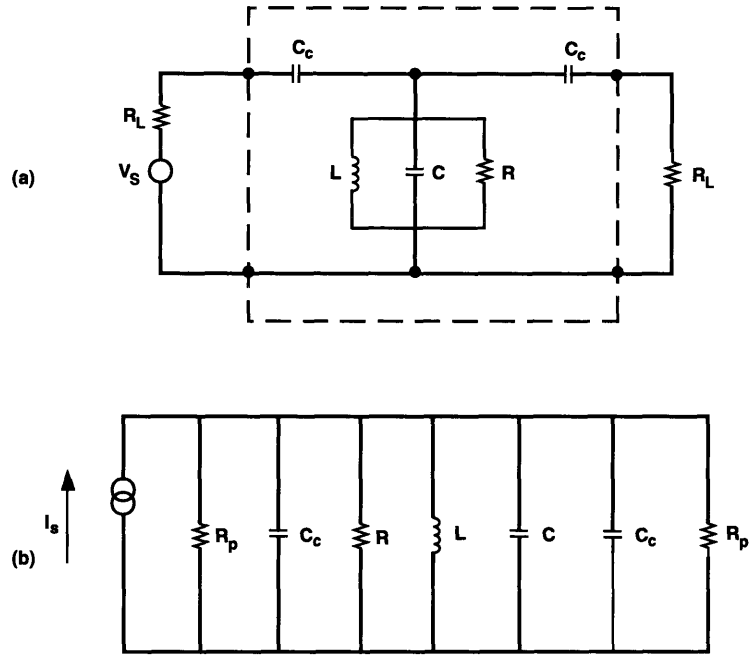

Figure 4-7: (a) Equivalent circuit and (b) parallel equivalent circuit models of a transmission line resonator, which are used for calculation of the resonator current at resonance. C_c is the capacitance of the coupling gap.

4.5.1 Microwave Current and Self-Induced Magnetic Field

The high Q values of the resonators translate into very high current densities for the conductors. To calculate the current in the resonator center conductor at resonance, the equivalent circuit model [57] shown in Fig. 4-7(a) is used.

The transmission line parameters per unit length: the capacitance C, the inductance L, and the resistance R are derived from the Q and other parameters of the resonator. Specifically,

$$C = \frac{n\pi}{2Z_0\omega} \tag{4.6}$$

$$L = \frac{1}{\omega_0^2 C} \tag{4.7}$$

$$R = \frac{2Q_c Z_0}{n\pi} = \frac{Q_c}{\omega_0 C} \tag{4.8}$$

where n is the overtone mode number of the resonance, ω_0 is the unloaded resonant frequency, and Q_c is the unloaded Q of the resonator. The voltage at resonance can

be easily calculated by transforming the circuit of Fig. 4-7a into a parallel circuit. For $\omega_0 C_c \ll 1/R_L$, where C_c is the capacitance of the coupling gap, the equivalent circuit is given in Fig. 4-7b. Here I_s, the current generated by the source, is $I_s = j\omega_0 C_c V_s$, where V_s is the voltage generated by the source; and R_p, the equivalent parallel source resistance, is $R_p = 1/(\omega_0^2 C_c^2 R_L)$. At resonance, the voltage in the resonant cavity is

$$V = \frac{RR_p}{2R + R_p} I_s. \tag{4.9}$$

The V_L, defined as the voltage across the load resistance R_L, is $V_L = [R/(2R+R_p)]V_s$. We can then define a voltage insertion ratio for the resonator, r_v, as $r_v \equiv |2V_L/V_s| = 2R/(2R + R_p)$; r_v is related to the insertion loss by $IL = -20 \log r_v$. The cavity voltage V is then given by

$$V = j\sqrt{r_v(1 - r_v)\frac{R}{2R_L}} V_s \tag{4.10}$$

and by using expressions 4.6, 4.7, and 4.8, we obtain

$$V = j\sqrt{\frac{r_v(1 - r_v)Q_c Z_0}{n\pi R_L}} V_s. \tag{4.11}$$

The available power P from the source is

$$P = \frac{V_s^2}{4R_L} \tag{4.12}$$

and the current I at the standing wave peaks in the resonator at resonance is

$$|I| = \frac{|V|}{Z_0}. \tag{4.13}$$

Substituting (4.12) and (4.13) into (4.11) yields:

$$|I| = \sqrt{\frac{r_v(1 - r_v)4Q_c P}{n\pi Z_0}}. \tag{4.14}$$

This is the rms value of I, so the maximum current, I_0, is $I_0^2 = 2I^2$. From the total

current and the calculated distribution, the rf magnetic field at the surface of the conductors can easily be calculated. The field distribution peaks near the edges, like the current density. Throughout this thesis, I define the amplitude of the maximum magnetic field at the peaks of the resonant standing wave in the center line to be H_{rf}.

4.5.2 Complications Arising from Nonlinearity

A. Distorted Resonant Curve

As the microwave power is increased, the Q decreases, and the center frequency of the resonance shifts downward. As the power is increased further, the resonant curve of the transmitted power vs frequency becomes distorted and depart markedly from the usual Lorentzian shape.

Figure 4-8 shows a series of resonance curves for different input powers for a YBCO film at 78 K for the first overtone mode of the resonator $f_0 = 3$ GHz. The input power is stepped in 5-dB increments starting at -20 dBm and ending at $+30$ dBm (1 W). These results are typical of the behavior of a nonlinear oscillator [58] and are similar to those observed in other superconducting resonators [59], except that YBCO resonance curves usually do not show hysteresis in frequency sweeps, as is seen in NbN (Fig. 4-9). The dashed lines are calculations using a transmission line model with a nonlinear inductance and a nonlinear resistance [60]. Figure 4-9 show the equivalent non-Lorentzian resonant curves for NbN films at high powers together with the calculations [60].

B. Measurement of Q

When the resonant curve gets distorted, the calculation of the Q by the 3-dB bandwidth criterion becomes invalid. An equivalent circuit, however, can be used to show that the Q is proportional to the insertion loss at the peak of the resonant curve [61]. In practice, however, the Q values measured by the 3-dB points and by the insertion loss at the resonant peak are found to differ by less than 10%. Consequently, I use the 3-dB bandwidth criterion to calculate the Q at high rf powers in this thesis. The resonant frequency for the non-Lorentzian resonant curve is still at the peak of the

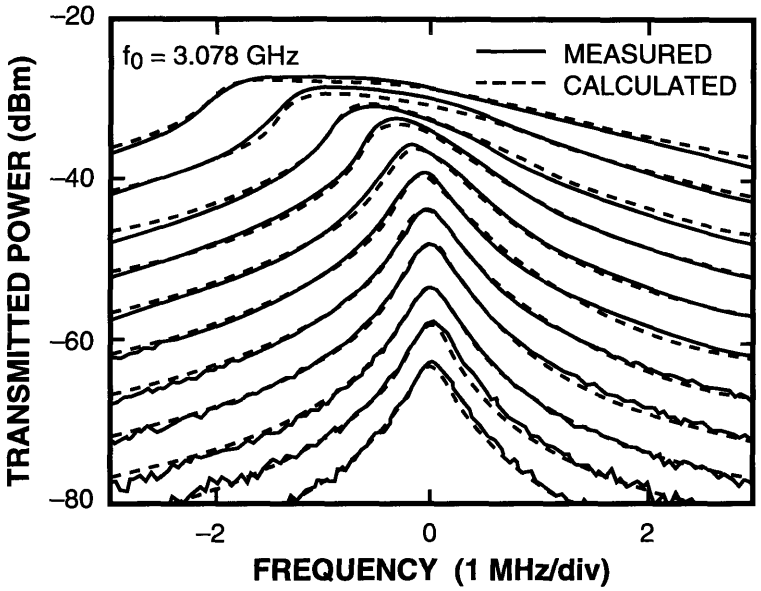

Figure 4-8: A $YBa_2Cu_3O_{7-x}$ resonator. Transmitted power versus frequency $(f - f_0)$ for input power levels ranging from 30 dBm to -20 dBm in 5 dB increments. The solid curve is the measured response, and the dashed curve is the calculated response. Resonator operated at $t = T/T_c = 0.89$.

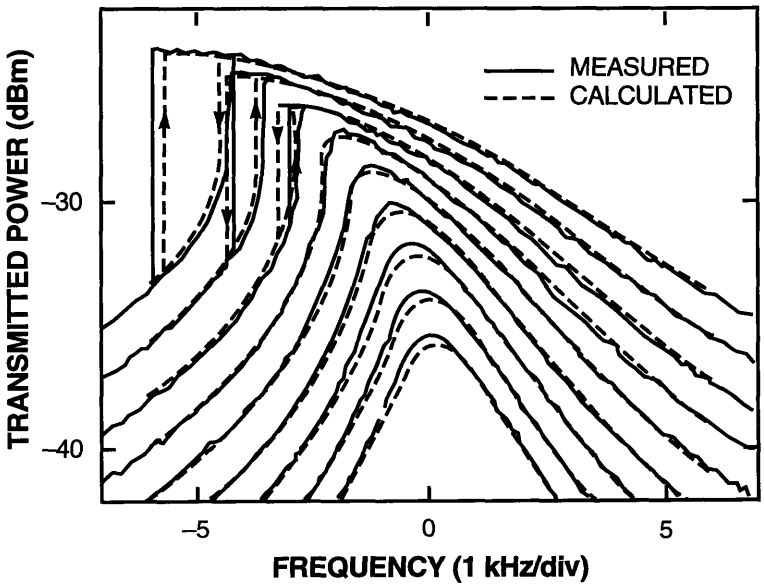

Figure 4-9: A NbN resonator. Transmitted power versus frequency $(f - f_0)$ for input power levels ranging from 0 dBm to -16 dBm in 2 dB increments. Solid curve is the measured response, and the dashed curve is the calculated response. Arrows represent the sweep direction. Resonator operated at $t = T/T_c = 0.27$.

curve, where the total reactance of the circuit is zero.

C. Microwave Current and Self-Induced Magnetic Field

From the Q, the input power, and the insertion loss, the rf current amplitude at the standing wave maxima at resonance can be calculated exactly the same way as for low-rf-power measurements (Sect. 4.5.1). The current as a function of the position z along the length of the stripline still is

$$I_{\rm rf}(z,t) = I_0 \sin(\frac{n\pi z}{l}) \cos(\omega t), \tag{4.15}$$

where l is the length of the resonator center line and $\omega = 2\pi f$ with f being the frequency. Though derived assuming a linear circuit, Eqs. (4.14) and (4.15) can be used to calculate the current at high rf power, because the measurements show that the changes in the total inductance of the transmission line are small, even at the highest rf power levels considered in this work. Therefore, the total current and the current distribution remain, to a good approximation, unchanged at high power, since they are determined by the inductance.

The peak self-induced surface field at the maxima of the standing waves at resonance $H_{\rm rf}$ can be calculated from the current distribution [53], after obtaining the current amplitude I_0 (see Sect. 4.5.1). In the limit of zero rf field, $H_{\rm rf}$ is proportional to I_0, and the proportionality constant is a function of the geometry and $\lambda(T)$. At nonzero rf field, the proportionality constant becomes dependent also on $I_{\rm rf}$. For the low and intermediate field regions (the vortex-free regions), we can use the zero field value for the proportionality constant, since the power dependence of this constant is weak [62]. For the high field region, our estimate yields only an upper limit to the true $H_{\rm rf}$.

D. Surface Resistance

For rf fields at which nonlinear effects become observable, the power dependence of the geometrical factor Γ in Eq. (4.5) must be taken into account. Furthermore, Eq. (4.2)

no longer holds, since the complex resistivity ρ becomes spatially nonuniform. Nevertheless, I can define an effective surface resistance as

$$R_s \equiv \Gamma[\lambda(T)/d] f/Q_c, \tag{4.16}$$

which reduces to

$$R_s = \mathcal{R}e(Z_s) = \mathcal{R}e([j\omega\mu_0\rho]^{1/2})$$

if ρ is spatially uniform. (For low enough rf magnetic field, ρ is in fact nearly uniform [63].) This is the definition for R_s that I use throughout this thesis. Note $\Gamma[\lambda(T)/d]$ here is the geometrical factor in the zero field limit.

E. Penetration Depth

Analogously, the effective London penetration depth λ, which is inversely proportional to the superconducting carrier density, becomes spatially nonuniform for nonzero rf fields. I can define, however, an effective λ at high $H_{\rm rf}$ as follows:

$$\lambda(T, H_{\rm rf}) \equiv F[f_0(T, H_{\rm rf})], \tag{4.17}$$

where $F[f_0(T, H_{\rm rf})]$ is the function mapping the temperature-dependent $f_0(T, 0)$ into $\lambda(T, 0)$ in the zero-field limit [53]. Recall that f_0 denotes the resonant frequency (of a certain mode n) of the resonator, whereas f denotes the frequency. The field-induced change $\Delta\lambda(T, H_{\rm rf})$ can be calculated using

$$\frac{\Delta\lambda(T, H_{\rm rf})}{\lambda} = -\frac{2L}{\lambda dL/d\lambda}\frac{\Delta f_0(T, H_{\rm rf})}{f_0}, \tag{4.18}$$

where L is the total inductance of the stripline resonator, and $dL/d\lambda$ is its derivative with respect to λ [53].

Chapter 5

Power Dependence of Surface Impdedance of $YBa_2Cu_3O_{7-x}$ Thin Films at Microwave Frequencies

5.1 Introduction

Microwave measurements of the surface impedance $Z_s = R_s + jX_s$, where R_s is the surface resistance and X_s the surface reactance, provide one of the most useful probes of the superconducting state. The surface resistance R_s results from microwave power losses and can be related to the normal carrier density, whereas X_s reveals information about the superconducting electron density.

This chapter is concerned with measurements and modeling of Z_s as a function of temperature, frequency, and rf magnetic field of high-quality $YBa_2Cu_3O_{7-x}$ thin films in order to provide insight into the mechanisms of superconductivity and to better understand the microwave properties when the films are applied to practical devices.

The surface resistance R_s in epitaxial thin films of high-temperature superconductors deviates considerably from the predicted BCS exponential drop at low tem-

perature [64] below the superconducting transition temperature T_c. The difference between the measured R_s and that calculated from the BCS theory is defined as the residual surface resistance. All superconductors show a finite residual surface resistance which dominates the intrinsic BCS value at sufficiently low temperatures. In the oxide high-T_c materials, however, the residual surface resistance is dominant up to $t = T/T_c = 0.9$. As will be discussed below, my analysis and measurements are consistent with the residual surface resistance being an extrinsic effect, resulting from defects in the material.

The nonlinearity in Z_s, i.e., the dependence of Z_s on the microwave current $I_{\rm rf}$, in the oxide superconductors has been observed by a number of workers in both bulk and thin film materials [65, 66, 67]. Nonlinear effects provide a means to study the pair-breaking process, vortex creation, and vortex motion. A better understanding of the nonlinearity can also help high-T_c film makers characterize and improve their films. The strong power dependence of Z_s in high-temperature superconductors invariably affects possible applications of these materials. Decreases in the resonant Q or increases in device loss have a negative impact on device performance. Moreover, a nonlinear impedance leads to such nonlinear effects as intermodulation distortion and harmonic generation. Microwave frequency $1/f$ noise may also be related to nonlinear conduction processes.

In addition to presenting the measurements, I will attempt to model the linear (in the limit of zero rf field) surface impedance as well as the nonlinear effects. The linear residual surface resistance has been an important subject for study in high-T_c materials, and a number of authors have proposed models to explain it [68, 69, 70, 71, 72]. The nonlinear effects have also been measured by a variety of workers [66, 67, 73]. Little work, however, has been done to date to model the nonlinear effects in epitaxial films. The epitaxial films reported here show similar behavior from sample to sample and therefore can be modeled in a consistent manner.

The surface impedance of YBCO thin films shows two regions of qualitatively different behavior: the low- and intermediate-rf-field and the high-rf-field regions. I will first present the measurements and modelling of the two regions. Then I will

Table 5.1: Parameters of films

Film	Sample	Thickness [μm]	$\lambda(0)$ [a] [μm]	T_c [a] [K]	H_p(T) [b] [Oe]	J_c^P(T) [b] [A/cm^2]
YBCO:						
Off-axis	1	0.30	0.17	86.4	190 (11K)	1.5 $\times 10^7$ (11K)
Off-axis	2	0.30	0.22	89.5	37 (77K)	5.3 $\times 10^6$ (77K)
Off-axis	3	0.30	0.27	89.6	27 (77K)	1.0 $\times 10^6$ (77K)
Cylindrical	4	0.80	0.23	87	102 (77K)	2.8 $\times 10^6$ (77K)
Cylindrical	5	0.20	0.22	88	189 (6K)	1.8 $\times 10^7$ (6K)
Pulsed laser	6	0.10	0.16	91	145 (4.3K)	5.5 $\times 10^7$ (4.3K)
Off-axis	7	0.20	0.17	90	17 (77K)	4.8 $\times 10^6$ (77K)
Off-axis	8	0.30	0.20	90	—	—
NbN:						
On-axis	NbN1	0.80	0.39	15.3	42 (13.4K)	1.2 $\times 10^5$ (13.4K)
On-axis	NbN2	0.80	0.39	15.9	—	—

[a] Obtained by method described by Sheen *et al.* [53]

[b] Pinning critical current density J_c^P and vortex penetration field H_p are obtained from fits to the fundamental modes using the modified Bean model, see text.

discuss the validity, the limitations and some possible improvements of the models. Magnetization data will be examined to determine the effects of structural defects on the transport properties of the films. Finally, intermodulation products measurements will be shown as an alternative microwave technique to study the nonlinearities in a superconductor and to demonstrate that the nonlinearities observed in Z_s are not caused by heating effects, which are slow.

5.2 Samples

Several YBCO films were measured, eight of which are listed in Table 5.1. They were deposited *in situ* onto $LaAlO_3$ substrates by off-axis sputtering [74], inverted-cylindrical-magnetron sputtering [75], and pulsed laser deposition [76]. The transition temperatures T_c obtained via microwave Z_s measurements range from 87 K to 91 K. The dc critical-current densities for the YBCO films exceed 10^7A/cm^2 at 4.2K [17]. The low-rf-field R_s is comparable to that of other high-quality films reported in the

literature [64], e.g., for sample 7 in Table 5.1, R_s at 1.5 GHz is 1.3 $\mu\Omega$ at 19 K and 12 $\mu\Omega$ at 77 K. Two polycrystalline NbN films (Table 5.1) deposited on sapphire substrates by planar on-axis dc magnetron sputtering of a pure Nb target in an argon-nitrogen mixture were also measured for comparison [77]. NbN was chosen because it is a conventional superconductor whose properties are similar to high-T_c materials: large T_c, high upper critical field H_{c2}, high critical current density, strongly type II (i.e., the Ginzburg-Landau parameter $\kappa \gg 1/\sqrt{2}$), etc. [78, 79].

After being patterned with standard photolithography, the YBCO and NbN films were etched and assembled into stripline resonators. From the measured Q and resonant frequency f_0, we extract R_s and λ. The details of the resonators, measurements, and determination of Z_s from the measured quantities were described in Chapter 4. The superconducting transition temperatures T_c were determined from rf measurements and the zero-temperature penetration depths $\lambda(0\text{ K})$ were estimated from the temperature dependence of the resonant frequencies as also discussed in Chapter 4.

5.3 Nonlinearity of $Z_s(H_{\rm rf})$

Figure 5-1 shows the measured R_s and λ as functions of $H_{\rm rf}$ for sample 1 (Table 5.1). Similar results are obtained for the other films. The behavior of both R_s and λ is qualitatively different for the low- and intermediate- and high-rf-field regions. For the low- and intermediate-field region ($H_{\rm rf} < 50$ Oe for sample 1), R_s and λ increase quadratically in $H_{\rm rf}$,

$$R_s = R_s(0)[1 + b_R H_{\rm rf}^2] \tag{5.1}$$

and

$$\lambda = \lambda(0)[1 + b_\lambda H_{\rm rf}^2] \tag{5.2}$$

where b_R and b_λ are quadratic coefficients. In the high-rf-field region (> 50 Oe for sample 1), both R_s and λ increase faster than the quadratic dependences observed in the low- and intermediate-rf-field region. The broken lines in Fig. 5-1 are the best quadratic fits to *the entire field range* of $R_s(H_{\rm rf})$ and $\lambda(H_{\rm rf})$. The noticeably large

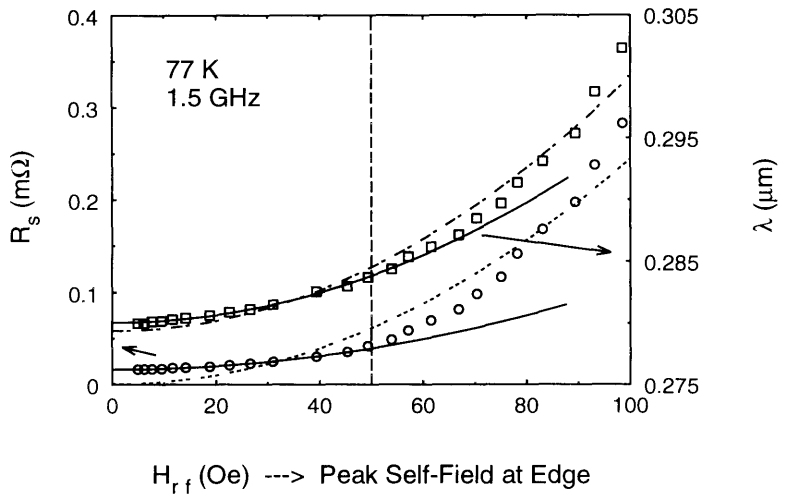

Figure 5-1: The measured R_s ($\circ$) and λ ($\square$) vs $H_{\rm rf}$ for YBCO sample 1 at 77.4 K and 1.5 GHz. The vertical dashed line at 50 Oe marks the approximate place where R_s and λ deviate noticeably from a quadratic dependence on $H_{\rm rf}$. The solid lines are the best quadratic fits of the power-dependent coupled-grain model [63] to the low- and intermediate-field region (< 50 Oe). The broken lines are the best general quadratic fits for the entire rf field range both below and above 50 Oe to demonstrate the non-quadratic behavior of R_s and λ.

deviation of the fits from the data indicates that R_s and λ are not well-described by the simple quadratic functions Eq. (5.1) and Eq. (5.2). The quadratic dependence of $Z_s(H_{\rm rf})$ on $H_{\rm rf}$ in the low- and intermediate-rf-field regime and the deviation in the high-rf-field regime has also been observed by other workers on high-quality YBCO films (see for instance, Rauch *et al.* [73] and Valenzuela *et al.* [66]).

Figure 5-2 plots R_s vs $H_{\rm rf}^2$ to emphasize the quadratic behavior in the low- and intermediate-field regime. It is more illuminating to plot $\Delta R_s(H_{\rm rf})$ vs $\Delta\lambda(H_{\rm rf})$, as shown in Fig. 5-3 for sample 1 at the same temperature and resonant frequency as in Fig. 5-1. $\Delta R_s(H_{\rm rf})$ and $\Delta\lambda(H_{\rm rf})$ are the changes in R_s and λ, respectively, induced by the increasing rf magnetic field. The inset shows the full field range. As seen in the figure, the large difference of the slope between the low- and intermediate-field and high-field regions suggests two different kinds of loss mechanisms governing the two regions.

For comparison, R_s and λ as functions of $H_{\rm rf}$ for NbN are presented in Fig. 5-4 at approximately the same reduced temperature $t \equiv T/T_c = 13.4/15.3 \simeq 77/87 = 0.885$

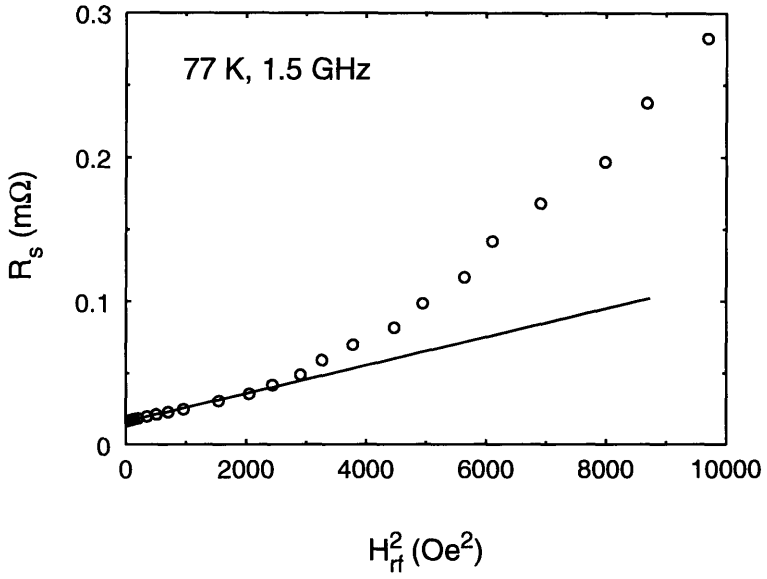

Figure 5-2: Surface resistance R_s vs H_{rf}^2 for sample 1 at the same temperature (77.4 K) and frequency (1.5 GHz) as in Fig. 5-1. In the low- and intermediate-field region, the data follow a straight line as the linear fit (solid line) shows.

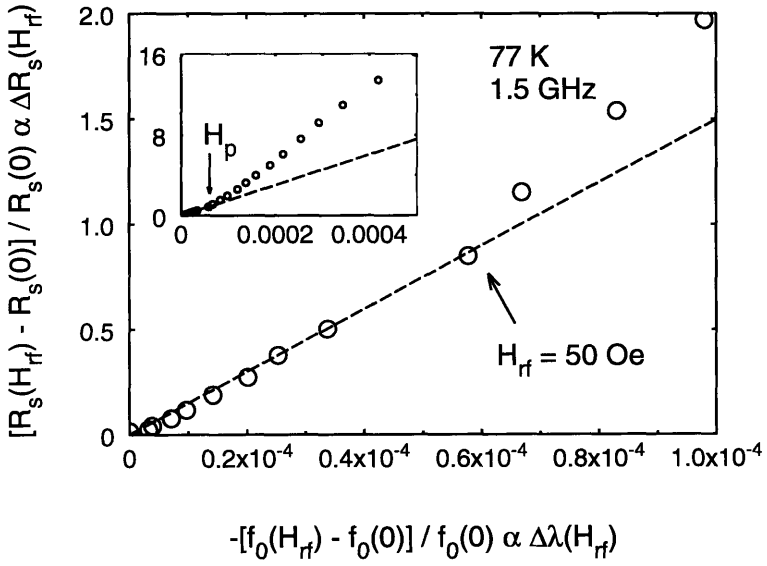

Figure 5-3: The rf-field-induced changes $\Delta R_s(H_{\rm rf})$ vs $\Delta\lambda(H_{\rm rf})$ for sample 1 at the same temperature and resonant frequency as in Fig. 5-1. The inset shows the entire field range, whereas the main plot magnifies the transition region (around 50 Oe) between the low- and intermediate-field regime and the high-field regime. The slope is observed to change noticeably upon crossing from one region to the next, signifying the appearance of new loss mechanisms.

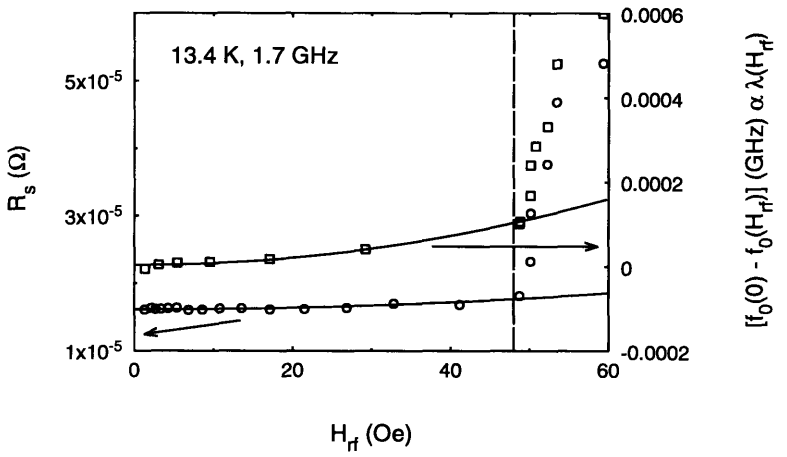

Figure 5-4: The measured R_s (○) and λ (□) vs H_{rf} for NbN sample 1 at similar reduced temperature T/T_c = 13.4 K/15.3 K as for YBCO sample 1 in Fig. 5-1 with T/T_c = 77 K/87 K. The vertical dashed line at about 49 Oe marks the place where R_s and λ start to deviate noticeably from a quadratic dependence on H_{rf}. The solid lines are the best quadratic fits to the power-dependent coupled-grain model [63] for the low- and intermediate-field region (< 49 Oe). Note that the distinction between the low- and intermediate-field and the high-field regions is much clearer for NbN than for YBCO films, since the slopes of R_s and λ for NbN change much more rapidly upon crossing into the high-field region.

as for YBCO sample 1 in Fig. 5-1.

The quadratic dependence on H_{rf} is again observed in the low- and intermediate-rf-field region (< 48 Oe). In the high-rf-field region, the deviation from a quadratic dependence is much more drastic than that in YBCO, making the distinction between the two regions much more obvious. (The difference in the magnitudes of the deviation in the high-rf-field regime between YBCO and NbN can be explained by the different magnitudes of their critical current densities, as discussed later.) Figure 5-5 plots the fractional change of R_s vs λ as induced by the rf current. Again, like for YBCO films, a large change in the slope is observed as the data cross from the low- and intermediate-field region to the high-field region.

In the next section, I focus on the low- and intermediate-rf-field region, the field region below a certain value H_p. I will use the power-dependent coupled-grain model that I developed in the Meissner state to explain the data in this field region. The model treats the superconductor as a network of superconducting grains connected

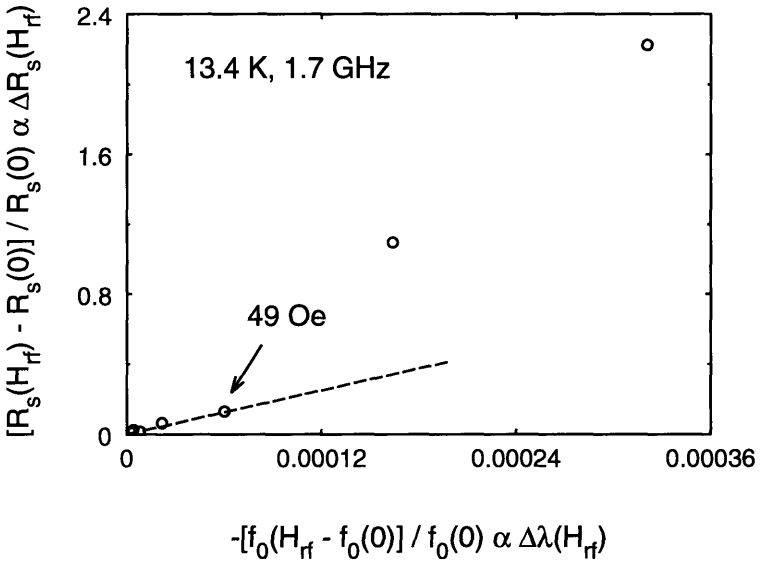

Figure 5-5: The rf-field-induced changes $\Delta R_s(H_{rf})$ vs $\Delta\lambda(H_{rf})$ for NbN sample 1 at the same temperature and resonant frequency as in Fig. 5-4. The slope changes noticeably upon crossing the same field value 49 Oe as in Fig. 5-4, signifying the appearance of new loss mechanisms.

by grain boundaries acting as resistively shunted Josephson junctions. In Sect. 5.5, I will examine the data in the high-field region and explain them with a modified Bean critical-state model, assuming the existence of rf vortices with H_p the microwave equivalent of the dc lower critical field H_{c1} above which vortices enter the sample.

5.4 Z_s at Low and Intermediate RF Fields

5.4.1 Experimental Results

Zero RF Field Limit

I define the zero-field limit for H_{rf} as the value of H_{rf} below which $R_s(H_{rf})$ is essentially independent of H_{rf}. For all of the striplines reported here, $H_{rf} \leq 0.5$ Oe satisfies this definition. Experimentally, I find that the behavior of R_s is dominated by the residual surface resistance at low temperature ($T/T_c < 0.9$) and the BCS theory does not apply. Figure 5-6 shows the zero field R_s vs the reduced temperature

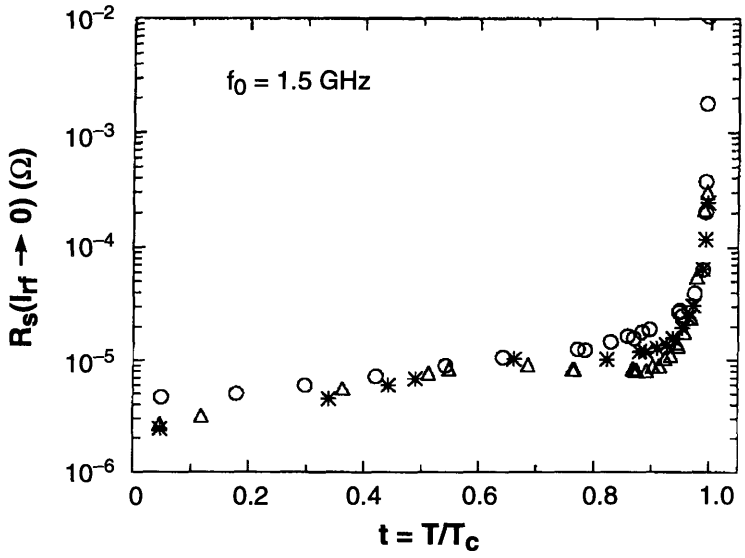

Figure 5-6: Zero-rf-field R_s for resonator 1 (circles), 2 (asterisks), and 4 (triangles) as a function of the reduced temperature $t = T/T_c$. See Table 5.1 for the parameters of the films.

$t = T/T_c$ for resonators 1 (circles), 2 (asterisks), and 4 (triangles). At 1.5 GHz, the lowest R_s value is about 15 $\mu\Omega$ at 77 K and 3 $\mu\Omega$ at 4.3 K. These films show the typical R_s vs T behavior. As observed also by others [64, 66], R_s drops sharply near T_c but then levels off to become nearly independent of T at low T, instead of decreasing exponentially to zero for $T \rightarrow 0$, as predicted by the BCS calculations. The high values of $R_s(T \rightarrow 0)$ for high-temperature superconductors are probably non-intrinsic since these values vary from sample to sample (Fig. 5-6) and sometimes even within the same samples over time [73]. Very recently, YBCO films deposited at the Research Center at Jülich, Germany, have shown an exponential drop in R_s at low temperature. This exponential decrease, however, occurs at temperatures much lower than those predicted by the BCS theory. Furthermore, efforts in our lab to observe this exponential decrease in striplines made from the same films from Jülich have failed. More work is currently underway to measure and explain the behavior of these unusual films. From now on, I will focus only on the more typical films that have non-exponential behavior at low temperature.

The small local maxima in the $R_s(t)$ curves around the reduced temperature

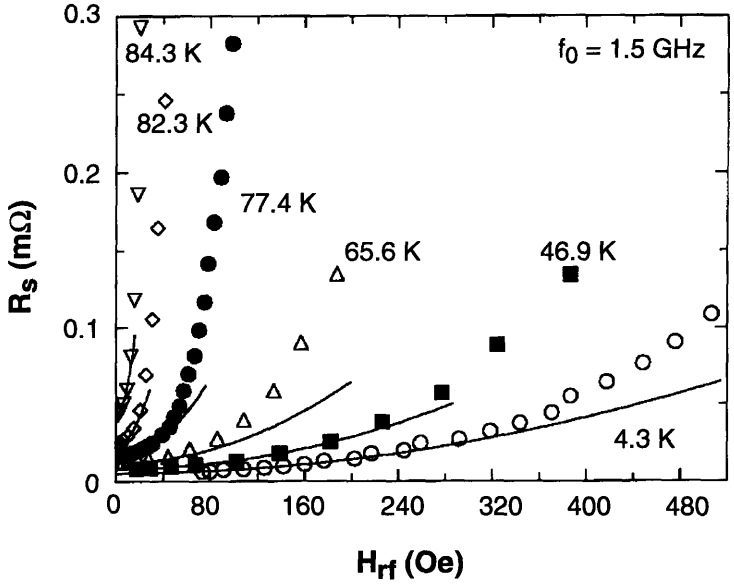

Figure 5-7: R_s vs H_{rf} at $f_0 = 1.5$ GHz for resonator 1 at different temperatures. The solid lines are quadratic fits to the data for $H_{rf} < H_p$.

$t \approx 0.6$ are less prominent for resonator 1 than for the other two. Other workers [73, 80] have observed similar peaks in R_s, although the temperature at which these peaks occur and the values of their heights appear sample dependent. The significance of the peaks is not yet well understood.

RF Field Dependence

Figure 5-7 presents a detailed set of R_s vs H_{rf} data at different temperatures for $f_0 = 1.5$ GHz. A least-squares quadratic fit to Eq. (5.1) is shown at each temperature in each of the intermediate rf field regions. All curves show similar qualitative behavior. Each curve shows that at high fields where $H_{rf} > H_p$, the increase in R_s is deviates from the H_{rf}^2 curve. The vortex-penetration field H_p decreases with increasing T. For the sake of clarity of the figure, the H_p value at each temperature is not explicitly indicated.

Figure 5-8 shows $\Delta\lambda/\lambda$ vs H_{rf} for the same temperatures as shown in Fig. 5-7 except that there is no curve at 4.2 K since the change in λ induced by rf power was smaller than the experimental uncertainties. A least-squares fit of the data to the

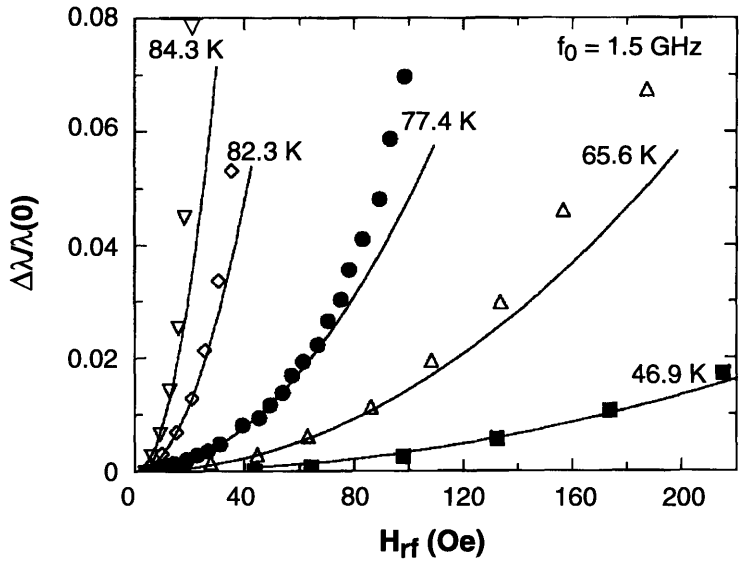

Figure 5-8: $\Delta\lambda/\lambda$ vs H_{rf} at $f_0 = 1.5$ GHz for resonator 1 at different temperatures. The solid lines are quadratic fits to the data for $H_{rf} < H_p$.

quadratic form

$$\frac{\Delta\lambda}{\lambda} = b_\lambda H_{rf}^2 \tag{5.3}$$

is shown in Fig. 5-8 for $H_{rf} < H_p$. The functional behavior of $\lambda(H_{rf})$ is similar to that of $R_s(H_{rf})$. The fractional change in λ, however, is very small compared with that of R_s. For example, $(\Delta\lambda/\lambda) \approx 0.01 \ll (\Delta R_s/R_s) \approx 1.0$ at 79.0 K, 1.5 GHz, and $H_{rf} = 50$ Oe for resonator 1.

Remember that the expression for the effective λ at finite rf power in this section is only an alternative expression of the resonant frequency of the stripline as defined in Eq. (4.17). Figure 5-9 plots the resonant frequencies f_0 as functions of rf field for the same set of temperatures as in Figs. 5-7 and 5-8. These resonant frequencies were used to calculate the corresponding effective λ in Fig. 5-8. The solid curves are quadratic fits to the form $f_0 = f_0(0)(1 - b_f H_{rf}^2)$ where $f_0(0)$ is the zero field resonant frequency (of that particular mode n) and b_f is the fitting constant.

Figure 5-10 plots R_s vs H_{rf} at $T = 79.0$ K for several resonant frequencies $n = 1$, 2, 3, and 5 for resonator 1. Mode 4 coincides with and is distorted by a resonant

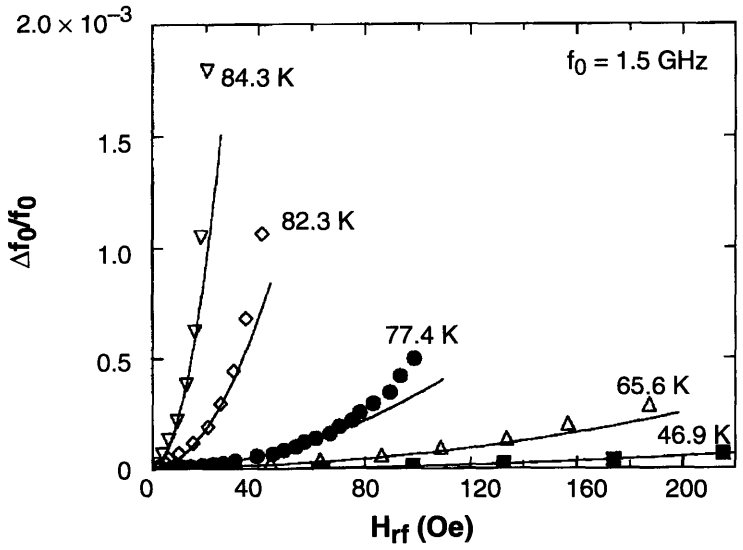

Figure 5-9: $\Delta f_0/f_0$ vs H_{rf} at $f_0 = 1.5$ GHz for resonator 1 at the same temperatures as Fig. 5-8. The solid lines are quadratic fits to the data.

frequency of the package, and hence is not shown here. The fitting procedure is the same as that used in fitting the data in Fig. 5-7.

5.4.2 Power-Dependent Coupled-Grain Model

Background

With the preliminary experimental results for Z_s and its nonlinearity, I have considered the possibility that the Ginzburg-Landau (GL) theory could be used to explain them [65]. My early work shows [65] that the functional dependence of $R_s(T)$ on rf power was consistent with the GL theory. Lam et al. [62] have also demonstrated that the GL theory can be used to fit the change in the resonant frequencies. My further efforts to calculate quantitatively the power dependence of $R_s(T)$ using the GL theory have shown that the amplitude of the power-induced change in $R_s(T)$ deduced from my measurements is too large to be explained by the GL theory with a reasonable value of the thermodynamic critical field H_c [81]. In addition, even with an extremely low H_c (< 0.1 T at 0 K), the GL theory fails to simultaneously fit the power dependences of both R_s and the resonant frequencies with the same parameters. As

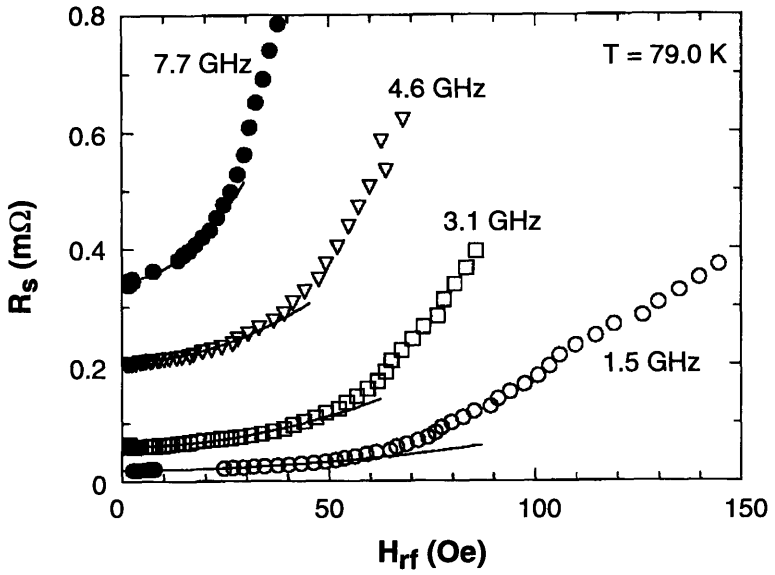

Figure 5-10: R_s vs H_{rf} at $T = 79.0$ K for various frequencies for resonator 1. The solid lines are quadratic H_{rf}^2 fits to the data.

will be seen later, the power-dependent coupled-grain model developed in this section agrees quantitatively with the measurements in the low- and intermediate-rf-field region and can fit simultaneously both R_s and the resonant frequencies with the same parameters.

Various models have been proposed to explain the non-BCS behavior of $R_s(T)$ of the high-temperature superconductors. Most of these models can explain some of the experimental results but not others. I now very briefly list some of the relevant models and their shortcomings: The large residual surface resistance (at low power) at low temperatures rules out any theories assuming a non-zero superconducting gap such as the BCS theory. For the low- and intermediate-rf-field regime, the quadratic dependence of R_s on f and H_{rf} rules out flux flow, flux creep, and hysteresis loss mechanisms, since flux flow should give a linear dependence on H_{rf} and no dependence on f, flux creep should give a linear dependence on H_{rf} [82], and hysteresis should give a linear dependence on f as I will show later in this chapter. That $Z_s(H_{rf})$ depends strongly on H_{rf} rules out models based on intrinsic losses such as the Ginzburg-Landau model, as shown before. Models with noncondensing electrons or small point

defects whose only role is to introduce extra normal electrons also cannot explain the observed large nonlinearity of $Z_s(H_{rf})$ [83].

The original coupled-grain model by Hylton et al. [71, 84] is among the simplest of the models mentioned above, and it allows for a natural introduction of the rf field dependence. Hylton et al., who considered only the low field Z_s, modeled the superconductor as being composed of a network of superconducting grains connected by grain-boundary weak links, acting as resistively shunted Josephson junctions. The grains are modeled as having intrinsic properties which can be calculated from the BCS and the Ginzburg-Landau theories. The properties of the grain boundaries are extrinsic to those of the grains. The residual R_s and the nonlinear part of R_s are related to the properties of the grain boundaries which dominate over those of the grains for temperatures $T/T_c < 0.9$. The magnetic penetration depth λ contains information on both the grains (i.e., the energy gap) and the grain boundaries (i.e., the junction critical current density and the shunt resistance). Physically, the grain boundaries determine the resistance because they are in series with the very small intrinsic resistance of the grains at low temperature. The grains, however, determine much of the inductance of the film (and hence the current distribution), since they constitute most of the volume of the material. This simple physical picture explains why the measured penetration depth is close to its intrinsic value, while the surface resistance is orders of magnitude larger than its intrinsic value at low temperatures.

The original coupled-grain model, however, fails to account quantitatively for the temperature dependence of R_s at low temperature ($t = T/T_c < 0.8$) [71]. Moreover, it does not deal with magnetic-field effects. Attanasio et al. [85] extended the coupled-grain model to take into account the field-dependent effects from the grain boundaries.

In this section, I further develop the coupled-grain concept to simultaneously describe R_s and λ as functions of temperature, frequency, and rf field amplitude. The model accounts for contributions from both the grains and the grain boundaries, resulting in the equivalent circuit for the intra- and intergranular admittances shown in Fig. 5-11. I will start by deriving expressions for the effective complex resistivity of the YBCO films.

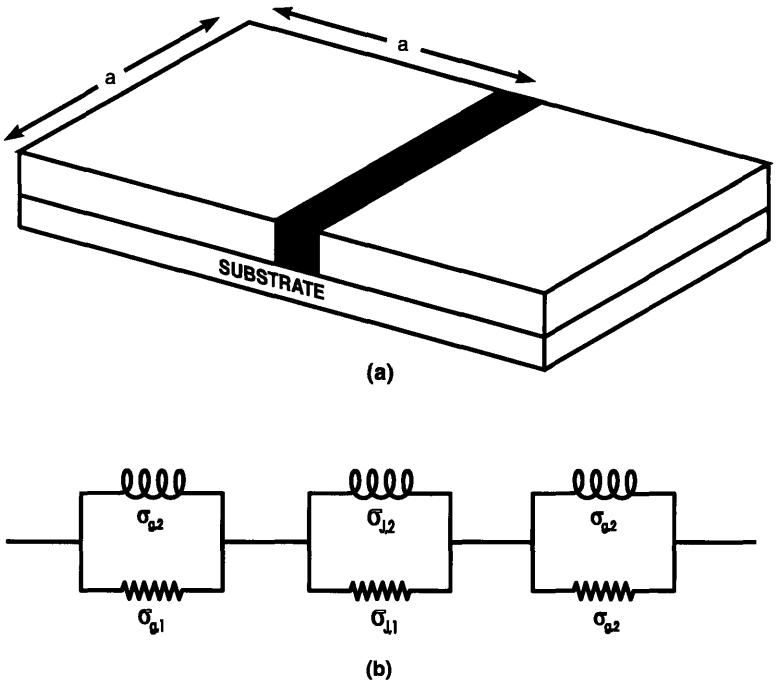

Figure 5-11: (a) Two grains of effective grain size a are coupled by a grain boundary which acts as a shunted Josephson junction. One of the two grains and a grain boundary constitutes a unit in the coupled-grain model. (b) The equivalent circuit of the unit in (a) with $\sigma_{g,1}$ and $\sigma_{g,2}$ the real and imaginary parts of the conductivity of the grain, and $\sigma_{J,1}$ and $\sigma_{J,2}$ the real and imaginary parts of the grain boundary averaged over the grain size. Note that the shunt resistance R_J is inversely proportional to $\sigma_{J,1}$ and the Josephson junction is represented as purely inductive for low rf currents (much less than the effective critical current of the junction).

Effective complex resistivity

Intragranular resistivity

For the YBCO grains, I apply the anisotropic Ginzburg-Landau (GL) equations [11] with the transport (rf or dc) current density $J(\vec{r},\tau)$ in the ab plane, where τ stands for time. I assume isotropy in the ab plane. The frequencies considered in this work (< 17 GHz) are low enough that the Meissner effect dominates over the classical skin-depth effect and hence the rf current can be treated in the same way as a dc current. Furthermore, that these frequencies are much smaller than $E_g(T)/\hbar > 1$ THz satisfies the condition for the applicability of the GL equations. Since only the transport currents in the ab plane are considered, the results here are identical to those obtained from solving the usual isotropic GL equations.

Considering the case in which $H_{\rm rf}$ is small enough that the order parameter Ψ varies slowly in space (on the order of the intragranular penetration depth λ_g, which is much larger than the coherence length), I can set $\nabla\Psi = 0$ and $\nabla^2\Psi = 0$. If I rescale the dimensions so that the anisotropic GL equations become isotropic and use the Coulomb gauge $\nabla \cdot \vec{A} = 0$ in the new coordinates, the superconducting electron density n_s as a function of current density can be shown to be

$$\lambda_g^{-2}(T,J) \propto n_s(T,J) = n_s(T,0)[1 - b_0(T)J^2(\vec{r},\tau)], \tag{5.4}$$

where $b_0(T) = \lambda_g^2(T)/2H_c^2(T)$, and H_c and λ_g are the zero-current thermodynamic critical field and intragranular London penetration depth, respectively. At the current densities considered in the low and intermediate field regimes, $b_0(T)J^2(\vec{r},\tau) \sim 0.01$, assuming $H_c(0\text{ K})$ of the order of 1 T [86] and $\lambda_g(0\text{ K}) = 0.15\ \mu$m [12]. Therefore, the shift in n_s or λ can be treated as a perturbation. If I use the temperature dependences $\lambda_g \propto 1/(1-t^4)^{1/2}$ and $H_c \propto (1-t^2)$ from the two-fluid model, then

$$b_0(T) = \frac{\lambda_g^2(0\text{ K})}{2H_c^2(0\text{ K})}\frac{1}{(1-t^4)(1-t^2)^2}. \tag{5.5}$$

Assuming that the real part $\sigma_{g,1}$ of the intragranular conductivity $\sigma_g = \sigma_{g,1} - j\sigma_{g,2}$ is

much smaller than the imaginary part $\sigma_{g,2}$, I get the usual two-fluid model resistivity $\rho_g = \rho_{g,1} + j\rho_{g,2}$ [87], where

$$\rho_{g,1} = \frac{\sigma_{g,1}}{\sigma_{g,2}^2} \tag{5.6}$$

and

$$\rho_{g,2} = \omega\mu_0\lambda_g^2(T,J) \tag{5.7}$$

with

$$\lambda_g^2(T,J) = \lambda_g^2(0\text{ K})[1 + b_0(T)J^2(\vec{r},\tau)]\frac{1}{(1-t^4)}. \tag{5.8}$$

Note from Eq. (5.6) that $\sigma_{g,1}$ and hence $\rho_{g,1}$ go to zero as $T \rightarrow 0$ (see Ref. [87]). $\lambda_g(0\text{ K})$ refers to $\lambda_g(T,J)$ at $T = 0$ and $J = 0$.

Intergranular resistivity

The intergranular resistivity is derived assuming the grains are connected by resistively shunted Josephson junctions [85] of effective critical current density J_c. For $J \ll J_c$, at the frequencies considered here, the inductive impedance dominates the resistive impedance (see Fig. 5-11). The real and imaginary parts of the effective resistivity $\rho_J = \rho_{J,1} + j\rho_{J,2}$, averaged over the cubic grains of size a, are derived in Refs. [71, 85] and rewritten keeping only the lowest-order terms in J ($\ll J_c$),

$$\rho_{J,1} = \frac{\omega^2\mu_0\lambda_J^2(T)\hbar}{2eJ_c(T)R_JA}\left(1 + \frac{J^2(\vec{r},\tau)}{J_c^2(T)}\right) \tag{5.9}$$

and

$$\rho_{J,2} = \omega\mu_0\lambda_J^2(T)\left(1 + \frac{J^2(\vec{r},\tau)}{2J_c^2(T)}\right), \tag{5.10}$$

where the effective continuum penetration depth λ_J is defined as

$$\lambda_J(T,J) \equiv \left(\frac{\hbar}{2eaJ_c(T)\mu_0}\left[1 - \frac{J^2(\vec{r},\tau)}{J_c^2(T)}\right]\right)^{1/2}, \tag{5.11}$$

R_J is the (temperature-independent) shunt resistance of the Josephson junctions, and A is the junction cross-sectional area $A = a^2$ or ad for grain size a smaller or larger than film thickness d, respectively. The effective continuum penetration depth λ_J should not be confused with the Josephson penetration depth which considers the

details of the field penetration in the junction region, even though the two resemble each other in form (in the limit of zero rf current $J \rightarrow 0$) [71]. The explicit power dependences in Eqs. (5.9) and (5.10) arise from the power dependence of the inductance of the Josephson junction [85]. Note that I have dealt explicitly with the nonuniform current distribution $J(\vec{r},\tau)$, which is assumed to be the same as that for a superconducting stripline with no grain boundaries. (This assumption is valid since the measured films are in the large-grain and strong-coupling regime [18], as seen later.) Consequently, my results, which are derived for short junctions, will later be generalized easily to long junctions by integrating over the whole junction area, assuming a uniform J_c across each junction.

Total resistivity

The total effective complex resistivity $\rho = \rho_1 + j\rho_2$ is the sum of the intra- and intergranular resistivities, ρ_g and ρ_J, respectively, where

$$\rho_1 = \rho_{g,1} + \rho_{J,1} \tag{5.12}$$

and likewise,

$$\rho_2 = \rho_{g,2} + \rho_{J,2} = \omega\mu_0\lambda^2(T,J), \tag{5.13}$$

with

$$\lambda^2(T,J) = \lambda_g^2(T,J) + \lambda_J^2(T,J). \tag{5.14}$$

From Eq. (5.9), I obtain

$$\rho_1(f,T,J) = \rho_1(f,T,0)(1 + b_\rho J^2), \tag{5.15}$$

with

$$b_\rho = b_{\rho,g} + b_{\rho,J} \tag{5.16}$$

where

$$b_{\rho,g} = \frac{2[1 - n_s(T,0)/2]b_0(T)}{[1 - n_s(T,0)]} \frac{\rho_{g,1}(f,T,0)}{\rho_1(f,T,0)} \tag{5.17}$$

is the intragranular contribution, and

$$b_{\rho,J} = \frac{1}{J_c^2(T)} \frac{\rho_{J,1}(f,T,0)}{\rho_1(f,T,0)} \tag{5.18}$$

is the intergranular contribution. From Eqs. (5.7) and (5.10), I write

$$\rho_2 \propto \lambda^2(T,J) = \lambda^2(T)(1 + b_\lambda J^2), \tag{5.19}$$

with

$$b_\lambda = b_{\lambda,g} + b_{\lambda,J}, \tag{5.20}$$

where

$$b_{\lambda,g} = 2b_0(T) \frac{\lambda_g^2(T)}{\lambda^2(T)} \tag{5.21}$$

is the intragranular contribution and

$$b_{\lambda,J} = \frac{1}{2J_c^2(T)} \frac{\lambda_J^2(T)}{\lambda^2(T)} \tag{5.22}$$

is the intergranular contribution.

Zero RF Field Limit

The surface impedance Z_s can be calculated from the formula for the surface impedance of a good conductor $Z_s = (j\omega\mu_0\rho)^{1/2}$, where ρ is the total effective resistivity derived above. Since $\rho_2 \gg \rho_1$ [88],

$$Z_s = R_s + jX_s \approx \frac{\rho_1}{2\lambda} + j\omega\mu_0\lambda \tag{5.23}$$

where $\lambda^2 = \lambda_g^2 + \lambda_J^2$ [see Eq. (5.14)]. Equation (5.23) in the limit of zero rf field is similar in form to that derived by Hylton et al. [71], except that ρ_1 here includes both the intra- and intergranular contributions [see Eq. (5.12)].

RF Field Dependence

I now calculate the power dependence of the Q and the resonant frequency f_0 (of some mode n) for $H_{rf} < H_p$. Since the center conductor is much narrower and its peak current density is at least two orders of magnitude larger than that in the ground planes [53, 62], the contribution to the surface impedance from the ground planes is more than an order of magnitude smaller and hence will be neglected. The power loss P of the stripline resonator, averaged over one cycle, is given by

$$P = \int_0^{1/f_0} \frac{d\tau}{(1/f_0)} \int_0^l dz \int_A \rho_1(f_0, T, J) J^2(\vec{r}, \tau) dx dy, \tag{5.24}$$

where A is the cross-sectional area of the center conductor and $J(\vec{r}, \tau)$ is the current density flowing in the z-direction (along the stripline of length l) as calculated in Ref. [53]. From Eq. (4.15),

$$J(\vec{r}, \tau) = J_0(x, y) \sin(\frac{n\pi}{l} z) \cos(\omega_0 \tau), \tag{5.25}$$

where $\int_A J_0(x, y) dx dy = I_0$ and $\omega_0 \equiv 2\pi f_0$. I have assumed that the current distribution remains unaffected by a change in the rf power. This assumption is good in the low and intermediate field regimes ($H_{rf} < H_p$), since the change in λ, which determines the current distribution, is small relative to λ as discussed above in Sec. III.B. Substituting Eq. (5.15) into Eq. (5.24) and integrating over τ and z, I obtain

$$P(I_0) = P(0)[1 + \frac{9 b_\rho}{16} G I_0^2], \tag{5.26}$$

where

$$G = \frac{\int_A J_0^4 dx dy}{\int_A J_0^2 dx dy (\int_A J_0 dx dy)^2} \tag{5.27}$$

and

$$P(0) \equiv \frac{l}{4} \int_A \rho_1(f_0, T, 0) J_0^2 dx dy. \tag{5.28}$$

The factor G in Eq. (5.27) is determined by the cross-sectional current distribution which depends on the geometry of the transmission line.

The total stored energy E averaged over one cycle in the stripline resonator can be expressed through the inductive part of the circuit: $E = E_m + E_k$, where E_m is the stored magnetic energy and E_k the stored supercurrent kinetic energy (giving rise to the kinetic inductance). More specifically,

$$E_m = \int_0^{1/f_0} \frac{d\tau}{(1/f_0)} \int_V \mu_0 |\vec{H}(\vec{r},\tau)|^2 d\vec{r} \tag{5.29}$$

and

$$E_k = \int_0^{1/f_0} \frac{d\tau}{(1/f_0)} \int_0^l dz \int_A \mu_0 \lambda^2(T,J) J^2(\vec{r},\tau) dx dy, \tag{5.30}$$

where V is the total volume of the stripline resonator and $\vec{H}(\vec{r},\tau)$ the rf magnetic field. The total inductance L, the magnetic inductance L_m, and the kinetic inductance L_k of the resonator can be obtained from $\frac{1}{4}LI_0^2 = E$, $\frac{1}{4}L_mI_0^2 = E_m$, and $\frac{1}{4}L_kI_0^2 = E_k$, respectively. Since the current distribution is basically unaltered by a change in the rf power as discussed before, increasing the rf power, or equivalently the rf field, produces little change in L_m. Consequently, I can attribute all of the power dependence of L to L_k. (Direct numerical calculations of the kinetic inductance and the internal and external inductances confirmed the domination in power dependence of the kinetic inductance [53]). Since $\Delta f_0/f_0 = -\Delta L/2L$, from Eq. (5.30), after a few simple integrations, I get

$$f_0(H_{rf}) = f_0(0)(1 - b_f H_{rf}^2), \tag{5.31}$$

in which the quadratic coefficient b_f, that depends on T, is given by

$$b_f = -\frac{\Delta f_0}{f_0 I_0^2} C \approx \frac{1}{2}\left(\frac{L_k(H_{rf}=0)}{L(H_{rf}=0)}\right)\left(\frac{9b_\lambda}{16}\right) GC, \tag{5.32}$$

where $\Delta f_0 \equiv f_0(H_{rf}) - f_0(0)$, G is a geometrical factor [Eq. (5.27)] and $C = C(T)$ is the proportionality constant between I_0^2 and H_{rf}^2 in the limit $I_0 = 0$, i.e., $I_0^2 = CH_{rf}^2$.

Similarly, I can write

$$Q = \frac{\omega E}{P} \approx \frac{\omega E(H_{rf}=0)}{P(H_{rf}=0)}[1 - \frac{9b_\rho}{16} G I_0^2]. \tag{5.33}$$

Since $R_s \propto 1/Q$, I obtain an expression for the quadratic coefficient $b_R(T)$ [defined in Eq. (5.1)]

$$b_R = \frac{\Delta R_s}{R_s(H_{\rm rf}=0)I_0^2}C \approx \frac{9b_\rho}{16}GC \tag{5.34}$$

where $\Delta R_s = R_s(H_{\rm rf}) - R_s(0)$.

5.4.3 Comparison between Model and Experiment

The real part $\rho_{g,1}$ of the intragranular resistivity approaches zero exponentially for $t < 0.7$ in both the BCS theory and the two-fluid model [Eq. (5.6)]. In contrast, the imaginary part $\rho_{g,2} \propto \lambda$ approaches a finite value at $T = 0$. Consequently, I expect the introduction of the grain boundaries to produce a large increase in R_s, but only a relatively small shift in X_s. In fact, the intergranular contribution to X_s becomes significant only when there are enough "bad" grain boundaries (of low junction critical currents), or more quantitatively, when $\lambda_J \geq \lambda_g$. I will show below that R_s and its field dependence are dominated by the grain boundaries, whereas the magnitude of λ is dominated by the grains. The field dependence of λ, however, is dominated by the grain boundaries.

There are three fitting parameters $J_c(T)$, a, and R_J that need to be determined in the coupled-grain model. Since the power dependence of $R_s(T)$ and $X_s(T)$ are most sensitive to $J_c(T)$ and a, respectively, I will start by comparing the calculated $b_R(T)$ and $b_f(T)$ with the measurements. The extracted values of $J_c(T)$ and a will then be used in estimating the zero field $R_s(T)$, using R_J as a fitting parameter.

RF field dependence

The rf field dependence of R_s and λ in the low and intermediate field range is characterized by the quadratic coefficients $b_R(T)$ and $b_f(T)$ defined in Eqs. (5.1) and (5.31), respectively. To estimate $b_R(T)$ and $b_f(T)$ from Eqs. (5.34) and (5.32), respectively, I can calculate the geometrical factor $G(T)$ from Eq. (5.27), the proportionality constant $C(T)$ in $I_0^2 = CH_{\rm rf}^2$, and the ratio $L_k(H_{\rm rf}=0,T)/L(H_{\rm rf}=0,T)$, using the current distributions derived numerically by Sheen et al. [53].

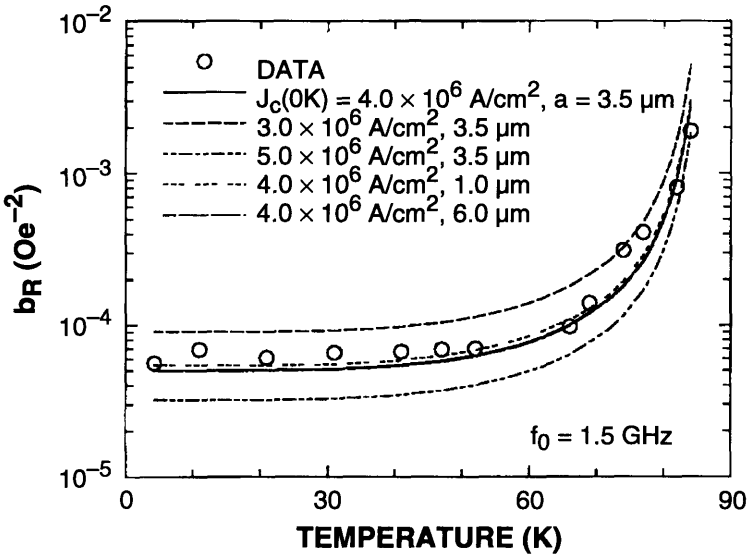

Figure 5-12: Temperature dependence of the quadratic coefficient b_R. The solid line is calculated from the coupled-grain model using the first set of values from Table 5.2. The dashed lines are produced by the remaining four sets of values from the same table.

Surface resistance

For the junction critical current density $J_c(0\text{ K})$ between 10^6 and 10^7 A/cm^2, the power dependence of R_s (or the unloaded Q) from the grain boundaries is much larger than that from the grains, i.e., $b_{\rho,g} \ll b_{\rho,J}$, assuming $H_c(0\text{ K})$ of the order of 1 T [86] and $\lambda_g = 0.15$ μm [12] as before. From Eqs. (5.16) and (5.18), I can write

$$b_\rho \approx b_{\rho,J} \approx \frac{1}{J_c^2(T)} \tag{5.35}$$

throughout the entire temperature range below T_c. Hence, from Eq. (5.34), I get

$$b_R \approx \frac{9 b_{\rho,J}}{16} GC. \tag{5.36}$$

Figure 5-12 plots b_R derived from the data used in Fig. 5-7 as a function of temperature. The solid line is the calculated b_R from Eq. (5.36) using $a = 3.5$ μm (as derived in the next subsection), $\lambda_g(T) = \lambda_g(0)/\sqrt{1-(T/T_c)^4}$, and the Ambegaokar

Table 5.2: Fitting parameters from the power-dependent coupled-grain model.

Film (Set)	J_c(0 K) (A/cm^2)	a (μm)	R_J (mΩ)
1 (1)*	4.0×10^6	3.5	0.09
1 (2)	3.0×10^6	3.5	0.16
1 (3)	5.0×10^6	3.5	0.06
1 (4)	4.0×10^6	1.0	3.60
1 (5)	4.0×10^6	6.0	0.02
2	3.4×10^6	3.0	0.01
3	2.1×10^6	3.0	0.32

* Best Set.

form for the junction critical current density

$$J_c(T) = J_c(0)\frac{E_g(T)}{E_g(0)}\tanh\frac{E_g(T)}{2k_BT}, \tag{5.37}$$

where $J_c(0) = \pi E_g(0)/2eAR_n$ and R_n is the quasiparticle-tunneling resistance (different from the shunt resistance R_J of the weak link). The critical current density $J_c(0)$ is a fitting parameter [to $b_R(T)$]. The energy gap $E_g(T)$ is assumed to follow the BCS temperature dependence and $2E_g(0)/k_BT_c = 4.3$ as used by Sridhar et al. to fit their $R_s(T)$ data [89]. As seen in Fig. 5-12, the agreement of the temperature dependence between the calculated curve (solid line) and the measurements is good over the entire temperature range. Furthermore, the value of $J_c(0) \approx 4.0 \times 10^6$ A/cm^2 obtained is comparable to the transport critical current densities $J_c^T(0)$ of the samples (see Table 5.1).

The dashed lines in Fig. 5-12 are estimates of b_R with slight variations of a and $J_c(0)$ to show the sensitivity of the calculations to these two fitting parameters (see Table 5.2). The shunt resistance R_J has been modified correspondingly to yield the same zero field $R_s(T)$. Note that R_J affects only the zero field $R_s(T)$ (and not b_R or b_f), and b_R is far more sensitive to J_c than to a.

The temperature dependence of $b_R(T)$ for samples 1 and 4, and an on-axis sputtered film from the Research Center at Jülich, Germany, is plottted in Fig. 5-13. The

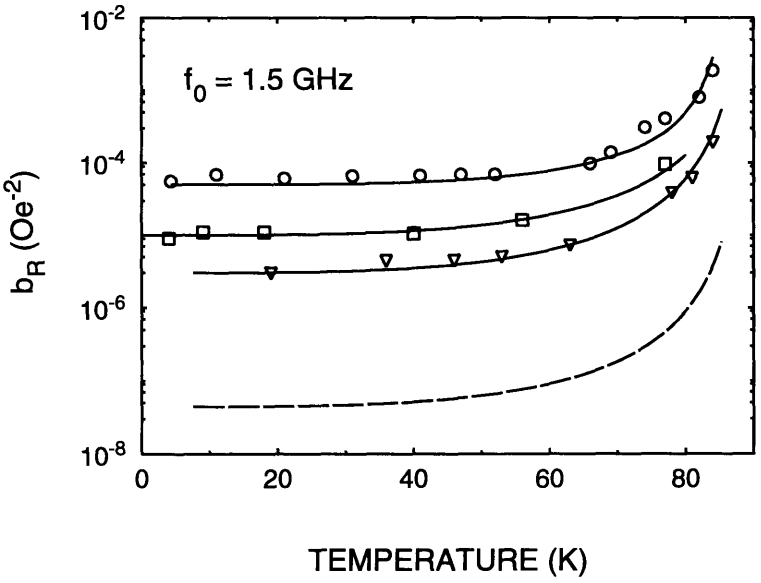

Figure 5-13: Temperature dependence of $b_R(T)$ for samples 1 (circles) and 2 (squares), and an on-axis sputtered film (inverted triangles) from the Research Center at Jülich, Germany. For comparison, an estimate of $b_R(T)$ for the intrinsic losses using the Ginzburg-Landau theory is also shown (dashed line).

solid lines are fits to the power-dependent coupled-grain model. For comparison, an estimate of $b_R(T)$ for the intrinsic losses using the Ginzburg-Landau theory is also shown (dashed line). As can be seen, the intrinsic losses yields a power-dependent coefficient $b_R(T)$ of about one order of magnitude smaller than that of the best Lincoln Lab high-quality films, indicating that there is considerable room for further improvement in film quality.

Figure 5-14 shows $\Delta R_s/H_{\rm rf}^2 \equiv [R_s(H_{\rm rf}) - R_s(0)]/H_{\rm rf}^2 = R_s(0)b_R$ as a function of frequency. $\Delta R_s/H_{\rm rf}^2$ should be proportional to f^2, since b_R is expected to be independent of f [Eq. (5.36)] and $R_s(0) \propto f^2$ [90]. This quadratic dependence on f is observed experimentally in Fig. 5-14, where the solid line (through the origin) is the best least-squares quadratic fit to $C_R f^2$. The fitting parameter C_R agrees within the experimental error with the calculation using the best calculated b_R and the experimentally determined value of $R_s(H_{\rm rf} = 0)$.

Effective penetration depth.

With $H_c(0\ {\rm K})$ of the order of 1 T [86], we find from Eqs. (5.11), (5.21), and (5.22)

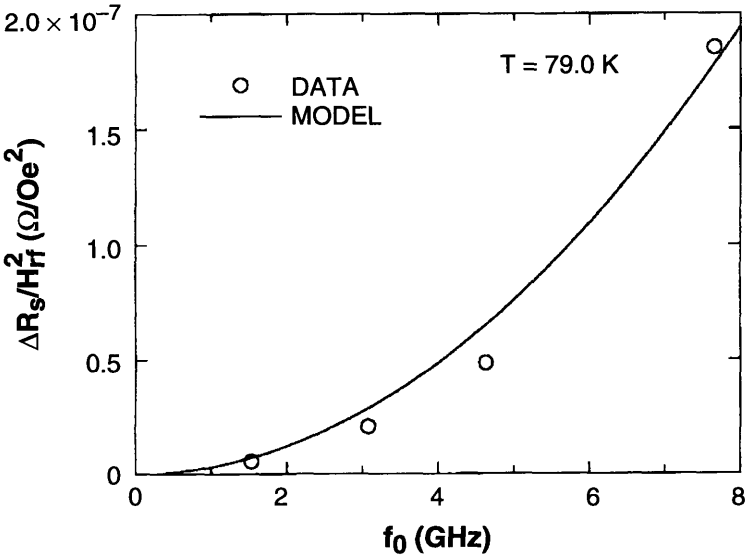

Figure 5-14: Frequency dependence of $\Delta R_s/H_{rf}^2$. The solid line is the best least-squares fit of the data to $C_R f^2$ with C_R a fitting parameter.

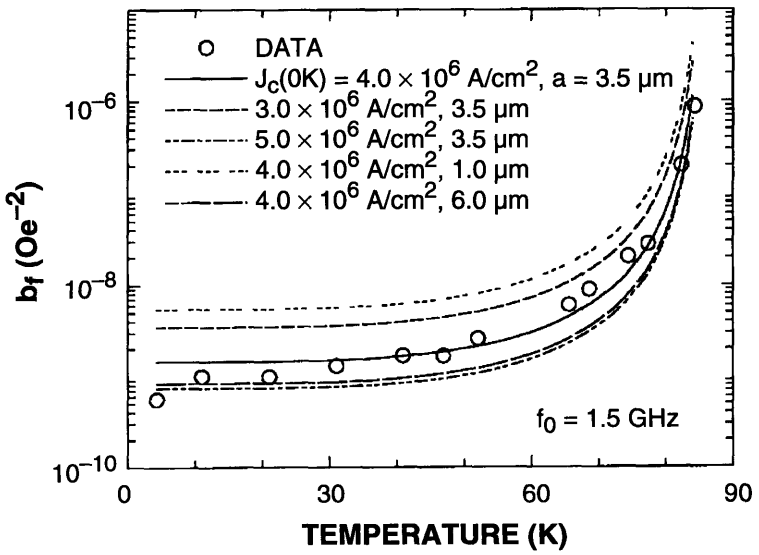

Figure 5-15: Temperature dependence of the quadratic coefficient b_f. The solid line is calculated from the coupled-grain model using the first set of values from Table 5.2. The dashed lines are produced by the remaining four sets of values from the same table.

that $b_{\lambda,J}(T) \gg b_{\lambda,g}(T)$ even though $\lambda_J(T) < \lambda_g(T)$. In other words, the effective penetration depth λ is determined by the grains but its power dependence is governed by the grain boundaries. Figure 5-15 presents the measured b_f as a function of T. The solid line is the calculated b_f from Eq. (5.32) using the value $J_c(0) = 4.0 \times 10^6$ A/cm^2 obtained above, and a as an adjustable parameter whose value $a = 3.5$ μm (also used previously) gives a close fit to the data. The agreement between the calculated $b_f(T)$ and the measurements is good. The *effective* grain size a is much larger than the average grain sizes (typically less than 1 μm [84, 91, 92]), probably because it denotes the average distance between only the grain boundaries with low critical current densities which are important in determining the power dependence of λ.

The dashed curves in Fig. 5-15, which are calculated from the remaining four sets of parameters in Table 5.2, are also presented to show the sensitivity of the calculated b_f to variations of the corresponding fitting parameters a and J_c. It can be seen that b_f is nearly equally sensitive to variations of both $J_c(0\text{ K})$ and a.

Figure 5-16 plots $\Delta f_0/H_{\rm rf}^2 = [f_0(I_0) - f_0(0)]/H_{\rm rf}^2 = f_0(0)b_f$ vs frequency. From the model, $\Delta f_0/H_{\rm rf}^2 \propto f$ for the frequency range considered in this paper ($f_0 < 17$ GHz), since b_f is independent of f [Eqs. (5.22) and (5.32)]. This linear dependence of the calculated $\Delta f_0/H_{\rm rf}^2$ on f is consistent with the measurements, as seen by the straight line fit in Fig. 5-16 (solid line) to $C_f f$, where the fitting parameter C_f agrees within the experimental error with the calculation using the best calculated b_f and the experimentally determined $f_0(H_{\rm rf} = 0)$.

Zero rf field limit

The surface resistance R_s falls rapidly below T_c in both the two-fluid model and the BCS theory. The dashed curve in Fig. 5-17 shows a BCS calculation for R_s as a function of the reduced temperature t [93] with $2E_g(0\text{ K})/k_BT_c = 4.3$, coherence length $\xi_0 = 3.1$ nm, and mean free path $l_0 = 7.0$ nm as in Ref. [89], and $\lambda_g(0\text{ K}) = 0.15$ μm as before. Above $t \approx 0.9$, the R_s values derived from our data drop more rapidly than predicted by the BCS model. This sharp superconducting transition

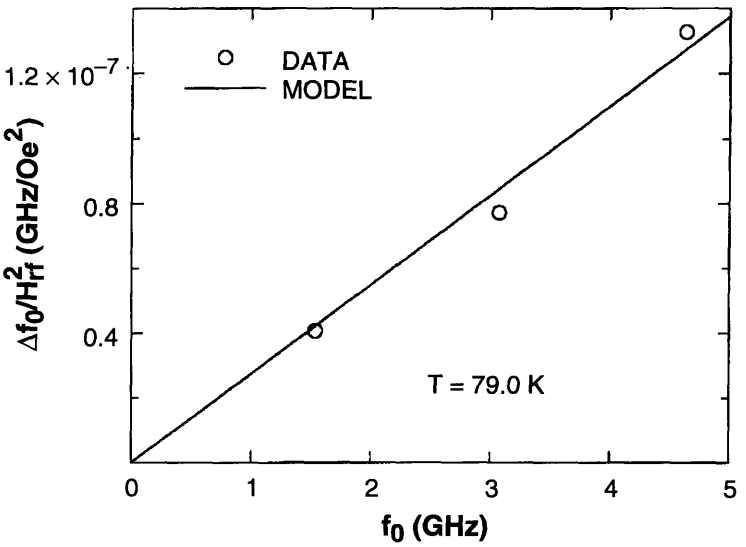

Figure 5-16: Frequency dependence of $\Delta f_0/H_{\rm rf}^2$. The solid line is the best least-squares fit of the data to $C_f f$ with C_f a fitting parameter.

has been observed also in YBCO single crystals [80]. The behavior of R_s at low temperature is clearly non-BCS. By the coupled-grain model considered here, the high residual value for R_s below $t = 0.9$ must come from the grain boundaries. From Eq. (5.23), neglecting $\rho_{g,1}$ and letting $\rho_1 = \rho_{J,1}$ for $t < 0.9$ where $\rho_{J,1}$ can be estimated from Eq. (5.9), I obtain the following relation for R_s in the $H_{\rm rf} \to 0$ limit:

$$R_s(f,T,0) = \frac{\rho_{J,1}(f,T,0)}{2\lambda(T,0)}. \tag{5.38}$$

By using the $J_c(T)$ and a derived previously (set 1 for film 1 in Table 5.2), a least-squares fit of Eq. (5.38) to the R_s data gives $R_J = 0.09$ mΩ. The fit (solid line in Fig. 5-17) looks reasonable, especially at low temperature ($t < 0.3$), though improvements to the fit close to T_c can be made if I introduce a temperature dependence to the *effective* R_J.

The value of R_J obtained here is about three orders of magnitude smaller than that measured by Gross et al. [94] and Chaudhari et al. [95] on fabricated grain-boundary single junctions. The difference in R_J may be due to two factors: the

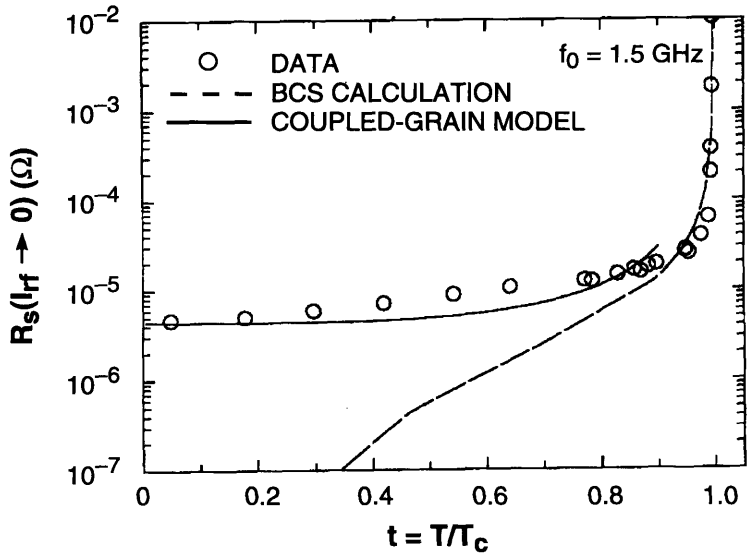

Figure 5-17: Zero field R_s for resonator 1 (circles). The dashed line is a BCS calculation with $\lambda(T = 0, H_{rf} = 0) = 0.15$ μm, $2E_g(0\text{ K})/k_BT_c = 4.3$, coherence length $\xi_0 = 3.1$ nm, and mean free path $l_0 = 7.0$ nm. The solid line is a calculation from the coupled-grain model as discussed in the text.

critical current densities of the fabricated grain boundaries in Refs. [94, 95] are an order of magnitude smaller than those for my films, and my effective grain size a is large. From Eq. (5.38), the fitting parameter R_J goes as $R_J \sim J_c^{-2}$ keeping everything else constant. My larger critical current densities, therefore, should account for most of the difference between our value of R_J and those measured from fabricated grain-boundary junctions [94, 95]. Moreover, since the fitting parameter R_J also goes as $R_J \sim a^{-3}$ [Eq. (5.38)] keeping everything else constant, my large effective grain size a should account for the rest of the difference.

Vortex-penetration field H_p

H_p can be *approximated* by eye from the Z_s data. Figure 5-18 shows H_p vs T for resonator 1 at 1.5 GHz. The long-dashed curve is the best least-squares fit (weighted by the error) to the two-fluid model functional form for the dc lower critical field $H_p(0\text{ K})[1-(T/T_c)^4]$ where $H_p(0\text{ K})$ is a fitting constant. The fit becomes very poor below about 60 K, where the experimental points also have larger error bars because

of the gradual deviation of R_s from a quadratic dependence of R_s on H_{rf} at low temperatures. Because vortices first enter the grain boundaries (where superconductivity is weakened) rather than the grains, H_p is more likely to reflect the lower critical field $H_{c1,J}$ of the grain boundaries. Since $H_{c1,J}$ is directly proportional to $J_c(T)$ [96, 97], the temperature dependence of $H_{c1,J}$ should follow approximately that of the J_c of a Josephson junction. The solid line in Fig. 5-18 is the best least-squares fit to $H_p = C_H J_c(T)$ where $J_c(T)$ is given by Eq. (5.37) and the proportionality constant C_H is a fitting parameter relating $H_{c1,J}(T)$ to $J_c(T)$. The results in Fig. 5-18 show that the fit of the experimental points to the Ambegaokar critical current function is slightly better than that to the two-fluid model but still well outside the experimental error.

If I use the functional form suggested in Ref. [66], $H_p = H_p(0\text{ K})[1 - (T/T_c)^2]$ with $H_p(0\text{ K})$ as a fitting parameter, the fit becomes excellent (short-dashed curve in Fig. 5-18). This functional form for the vortex-penetration field, however, is not well justified theoretically. Note that all the above values for H_p are obtained by inspection, and hence are highly inaccurate, since small deviations can easily escape the eye. These $H_p(T)$ values and their temperature dependence, however, agrees with those obtained by Valenzuela *et al* [66] using coplanar transmission line resonators. In the next section, I will present a more exact way to obtain H_p by using it as a fitting parameter in the modified Bean model.

5.4.4 Summary

I have presented a detailed characterization of the $Z_s(T, f, H_{rf})$ at low and intermediate rf fields for high-quality films of $YBa_2Cu_3O_{7-x}$ deposited *in situ* on $LaAlO_3$. For small H_{rf}, I find that for $t < 0.5$, the real part of Z_s, i.e., R_s, differs from the BCS theory by orders of magnitude. This deviation has also been observed by numerous other workers [64, 66]. With an appropriate set of characteristic parameters — J_c, a, and R_J — I have simultaneously accounted for the behavior of the zero field R_s and the rf field dependence of both R_s and λ as functions of temperature and frequency, using a coupled-grain model in which the superconductor is modeled as a network

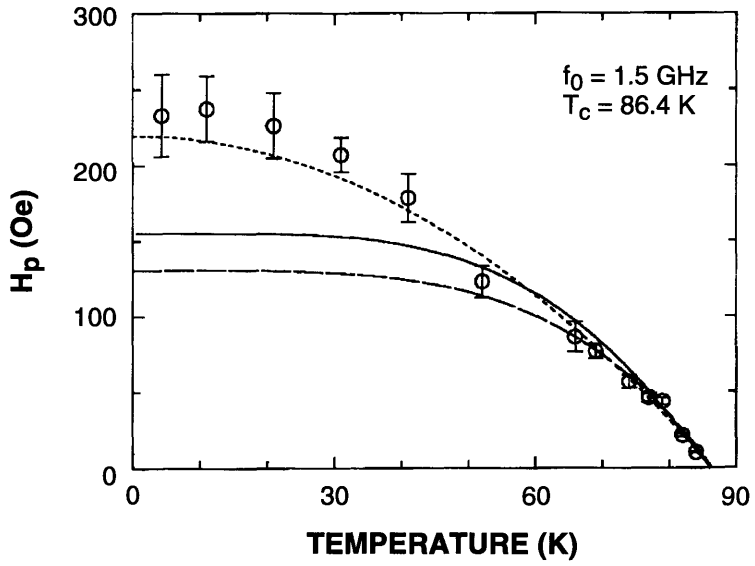

Figure 5-18: Vortex-penetration field $H_p(T)$ vs temperature for resonator 1 at 1.5 GHz. The long-dashed line is the best fit to $H_p(0\text{ K})[1-(T/T_c)^4]$ with $H_p(0\text{ K})$ a fitting parameter. The solid line is the best fit to the function $H_p = C_H J_c(T)$ where $J_c(T)$ is given by Eq. (5.37) and C_H is a fitting parameter. The short-dashed line is the best fit to the function $H_p = H_p(0\text{ K})[1-(T/T_c)^2]$ as suggested in Ref. [66].

of superconducting grains of intrinsic properties connected by weak-link Josephson junctions whose properties are extrinsic to the fundamental material and depend on film deposition and sample preparation.

It is interesting to note that the fractional power-induced change in R_s is more than one hundred times larger than the fractional change in λ. This is explained by the coupled-grain model in a simple way. The resistance is dominated by the properties of the weak-link Josephson junctions, which show a strong dependence on rf magnetic field. The zero field inductance is dominated by the intrinsic properties of the grains, which have weak dependencies on rf field. As the rf field is increased, the intergranular inductance increases much more rapidly than the intragranular inductance. The change in the intergranular inductance, however, is moderated by the large zero field intragranular inductance.

5.5 Z_s at High RF Fields

5.5.1 Experimental Results

The power-dependence of Z_s in the low- and intermediate-field regime has been quantitatively accounted for in the preceding section by the power-dependent coupled-grain model, which treats the superconductor as a network of superconducting grains connected by grain boundaries acting as resistively shunted Josephson junctions [18, 63, 84, 85]. The low- and intermediate- field regime corresponds to the Meissner state of the coupled-grain network. According to this power-dependent coupled-grain model, the Z_s of the superconducting junction network is nonlinear because the imaginary part of the junctions's impedance varies with input power.

As the microwave power is increased into the high-power regime ($H_{\rm rf} > 50$ Oe at 77 K for a typical YBCO thin film), Z_s becomes more nonlinear than in the intermediate-power regime, i.e., R_s and λ both increase more rapidly [63]. In the high-power regime, despite the interesting physics involved and the obvious importance of this nonlinear behavior of Z_s to film and device makers [98, 99], such nonlinear effects have not been

well-understood. I now present measurements of the losses at high microwave powers and explain them with a modified Bean critical-state model.

At low rf currents (linear Z_s), R_s, λ, and H_{rf}, can be numerically calculated [53]. At low and intermediate rf fields, as the complex resistivity of the material is no longer uniform, R_s and λ are not well-defined, and H_{rf} has to be corrected to account for the change in the rf current distribution. The deviation from the linear case is relatively small at low and intermediate rf fields, but becomes large at high rf fields as vortices enter the sample. I will continue, however, to employ these parameters in their average forms because they are useful and intuitive parameters. The corresponding well-defined parameters would be the unloaded quality factor Q_u, the resonant frequency f_0, and the rf current on the standing-wave peaks I_{rf}. I define the average parameters above as follows:

$$1/R_s \propto Q_u, \quad \Delta\lambda \propto \Delta f_0, \quad H_{rf} \propto I_{rf}$$

with the same proportionality constants as those in the low-rf-current situation [63]. The Q_u, f_0, and I_{rf} are not used because they are not fundamental parameters; they depend on the geometry of the measurements. It is important, however, to keep in mind that the average quantities R_s, λ, and H_{rf} used in this section are meaningful only as long as they are regarded as alternative expressions of the Q_u, f_0, and I_{rf}. These alternative expressions, of course, revert fully to their well-defined usual meanings at low rf powers.

The low- and intermediate-field region has been quantitatively explained by the power-dependent coupled-grain model in the Meissner state. As mentioned before, I propose that in the high-field region, above a certain vortex-penetration field H_p, rf vortices form and enter the sample, introducing vortex loss mechanisms. The superconducting film is treated as an effective continuous medium by averaging over the grains, defects, and grain boundaries. The field H_p is thus the microwave equivalent of the dc lower critical field H_{c1}. Note that in the high-rf-field regime, the losses described by the power-dependent coupled-grain model are still present. These losses,

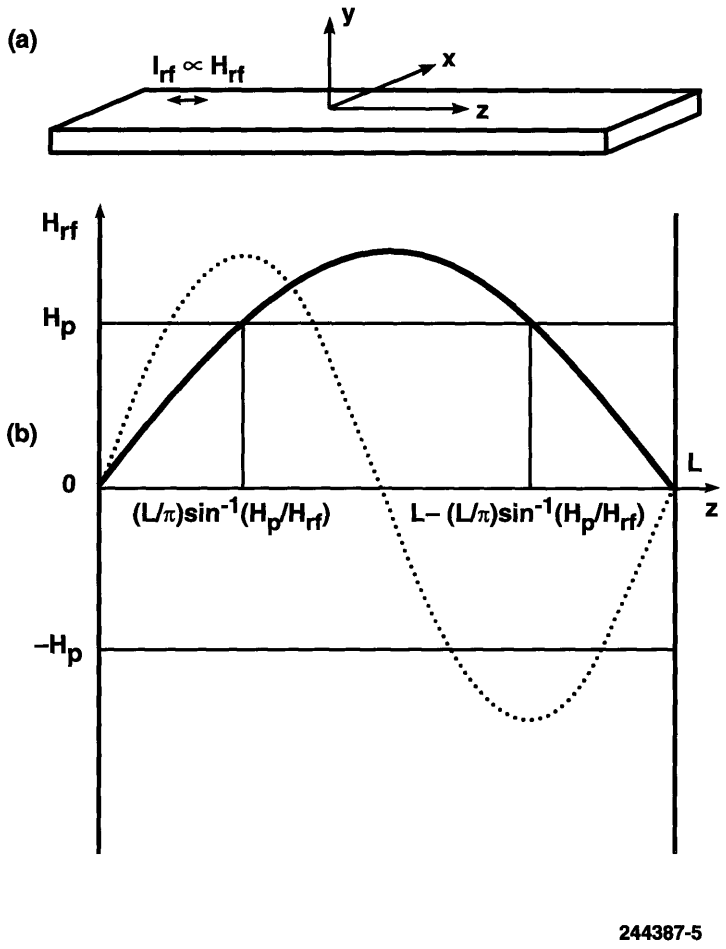

Figure 5-19: (a) Thin strip geometry with microwave current $I_{rf} \propto H_{rf}$ flowing along the length. (b) Amplitude of H_{rf} (or I_{rf}) along the length of the strip. The sinusoidal solid and dashed lines represent the first and second standing-wave resonant modes, respectively. The positions of the intersection of the first-mode curve with the H_p horizontal line are also shown.

referred to hereafter as Meissner losses, exist simultaneously with the added vortex-loss mechanisms, because the Meissner shielding surface current persists even after vortex penetration [100, 101]. Furthermore, in the stripline geometry with H_{rf} not much larger than H_p, vortices enter only the sections of the line around the peaks of the resonant standing wave (see Fig. 5-19). Part (a) of Fig. 5-19 shows a thin strip with microwave current $I_{rf} \propto H_{rf}$ flowing along the length. Part (b) shows the amplitude of $I_{rf} \propto H_{rf}$ along the length of the strip. Recall that H_{rf} is the peak rf field at the edges on the maxima of the resonant standing wave and is a function only of the coordinate z along the length of the line. The sinusoidal solid and dashed lines represent the standing waves of the first and second resonant modes, respectively. The positions of the intersection of the first-mode curve with the H_p horizontal line are also given. From Fig. 5-19, much of the line is still in the Meissner state for H not much bigger than H_p. Thus

$$R_s = R_s^M + R_s^B \tag{5.39}$$

where R_s^M and R_s^B correspond to Meissner and vortex hysteretic losses, respectively. R_s^M can be approximated above H_p by the power-dependent coupled-grain model [63]. Since hysteretic losses due to rf vortices are much larger than Meissner losses at sufficiently high rf fields, R_s^B can be deduced quite accurately using Eq. 5.39. In the next section, I calculate the unloaded Q_u of the stripline resonator using a critical-state model. The calculated Q_u will then be inverted to give the effective surface resistance R_s^B to compare with the measurements.

5.5.2 Analysis

The critical-state model is used to calculate the hysteretic losses at high rf fields. As the model does not distinguish between Abrikosov and Josephson vortices, I treat the films as an effective continuous medium, averaging over grains, defects and grain boundaries. Using the Bean critical-state model in which the lower critical field H_{c1} is assumed to be 0, Norris calculated hysteretic losses [102] incurred in a thin strip

of width $\gg$ thickness by a low-frequency $f < 1$ kHz current $I(t)$ with amplitude I_0. The emf (per unit length) induced in the strip is $E(x) = \partial\phi(x)/\partial t$ where x refers to the coordinate (Fig. 5-19) along the width $2a$ of the strip, and the flux $\phi(x) = \mu_0 \int_0^x H(s)ds$ where μ_0 is the permeability of free space. In each cycle, the energy dissipated $\mathrm{E_{cycle}}$ equals

$$\mathrm{E_{cycle}} = \int_0^{1/f} dt \int_{-a}^{a} \jmath(x)E(x)dx. \tag{5.40}$$

where conformal mapping gives the sheet current $\jmath$ which is the current density integrated over the sample thickness [102]. Norris found the dissipated power per unit length $\mathcal{P}$ due to hysteresis to be

$$\mathcal{P} = \frac{f\mu_0 I_c^2}{\pi}[(1-F)\ln(1-F) + (1+F)\ln(1+F) - F^2] \tag{5.41}$$

where $F = (I_0/I_c)$ and $I_c = J_c^P A$ with J_c^P the critical current density arising from vortex pinning (i.e., J_c^P is determined by the balance between the Lorentz and pinning forces [44, 103]: $J_c^P \propto U$ where U is the vortex pinning potential) and A the cross-sectional area of the strip. Equation (5.41) includes both the vortex-motion and vortex-annihilation losses [104]. For $I_0 \ll I_c$, Eq. (5.41) reduces to

$$\mathcal{P} \simeq \frac{f\mu_0}{\pi I_c^2} I_0^4. \tag{5.42}$$

Because of the thin-strip geometry, the hysteretic losses grow initially with the fourth power of the amplitude I_0, instead of the well-known third power derived for a semi-infinite superconducting slab [105]. From Eq. (5.42), as $I_0 \to 0$, $R_s \propto \mathcal{P}/I_0^2$ goes to 0 as I_0^2 for the thin film geometry. In contrast, as $I_0 \to 0$, $R_s \propto I_0$ for an infinite slab.

Since there was no limit imposed on f in the derivation, Eq. (5.41) should apply equally well at microwave frequencies [65]. Similarly, because the dimension along the film thickness does not enter Norris's conformal mapping formalism, Eq. (5.41) can be used for the anisotropic high-T_c superconductors. The bulk lower critical field H_{c1}, below which the superconductor is in the Meissner state (no vortices), however,

is assumed to be zero in both Bean's model and Norris's calculation. The assumption of vortex penetration at arbitrarily small magnetic fields, whether externally applied or induced by traversing current, is invalid for a real superconductor (see Appendix A). For a magnetic field much larger than H_{c1}, the assumption $H_{c1} \equiv 0$ gives a good approximation. For fields around H_{c1}, however, this assumption breaks down. To account for $H_{c1} > 0$, I need to apply the modified Bean model [100, 101] to Norris's calculation. From the modified Bean model, no hysteretic losses are present for $H_0 < H_{c1}$ where $H_0(I_0)$ induced by I_0 is the peak magnetic field at the edge of the strip, since there are no vortices penetrating the superconductor. For $H_0 > H_{c1}$, H_0 is replaced by $H_0 - H_{c1}$. The vortex-penetration field H_{c1} is included for $H_0 > H_{c1}$ because the equilibrium magnetization from the Meissner shielding surface current continues to exist even after vortex penetration [100, 101]. With the above modifications, applying Norris's calculation to the stripline geometry, I obtain hysteretic power losses per unit length for resonant mode n, for $I_p < I_{rf} \ll I_c$:

$$\mathcal{P}^B \simeq \frac{n f_{0,m1} \mu_0}{\pi I_c^2} \int_0^{'L} (I_{rf} \sin \frac{\pi z}{L} - I_p)^4 \frac{dz}{L} \tag{5.43}$$

where the rf current amplitude I_{rf} replaces I_0 in Eq. (5.42), I_p is the total peak rf current which produces a peak rf field H_p with vortex-penetration field H_p in place of H_{c1}, n is the resonant mode number, $f_{0,m1}$ the fundamental frequency, and L the length of the center line of the stripline resonator. The prime sign restricts the integral to the portions along the length of the stripline resonator (Fig. 5-19) in which the rf current $I_{rf}(z) = I_{rf} \sin(\pi z/L)$ is larger than I_p. I neglected the small contribution from the ground planes ($\ll 10\%$). Furthermore, the standing wave of the current $I_{rf}(z)$ is assumed to remain sinusoidal along the stripline, because the total inductance per unit length which determines the current distribution along the strip length is changed little upon flux penetration [63]. (The kinetic inductance changes upon flux penetration, but this change is still very small compared with the nearly-unchanged geometric inductance which is more than two orders of magnitude larger [53].) From the hysteretic quality factor $Q^B = 2\pi f \mathcal{E}/\mathcal{P}^B$ where $\mathcal{E} = \mathcal{L} I_{rf}^2$ is the

total stored energy per unit length and $\mathcal{L}$ the total inductance per unit length of the stripline, the microwave surface resistance due to hysteretic losses can be derived:

$$R_s^B \simeq \frac{n f_{0,m1} \Gamma \mu_0}{12\pi^2 \mathcal{L} I_c^2 C \Delta} F(H_{\rm rf}) \tag{5.44}$$

with

$$F(H_{\rm rf}) \equiv \int_{\frac{L}{\pi}\arcsin(\frac{H_p}{H_{\rm rf}})}^{L-\frac{L}{\pi}\arcsin(\frac{H_p}{H_{\rm rf}})} (H_{\rm rf}\sin\frac{\pi z}{L} - H_p)^4/H_{\rm rf}^2 \, \frac{dz}{L} \tag{5.45}$$

where $H_{\rm rf}^2 = CI_{\rm rf}^2$ with C a function of temperature only [63], $\Gamma = 0.41$ Ω/GHz is a geometrical factor, and $\Delta(\lambda(T)/\text{thickness})$ is a correction factor for finite film thickness [54]. Note that $R_s^B \propto f$, as expected for hysteretic losses, and $R_s^B \propto 1/(J_c^P)^2$ where $J_c^P \equiv I_c/A$. Recall that J_c^P or I_c refers to the current density or the corresponding total current determined by vortex pinnings as discussed in the next section. Equation (5.45) can be integrated exactly,

$$\begin{aligned} F(H_{\rm rf}) = \tfrac{H_p^4}{24\pi H_{\rm rf}^2}([24\pi + 72\pi(H_{\rm rf}/H_p)^2 + 9\pi(H_{\rm rf}/H_p)^4] \\ -[100 + 110(H_{\rm rf}/H_p)^2]\sqrt{(H_{\rm rf}/H_p)^2 - 1} \\ -[48 + 144(H_{\rm rf}/H_p)^2 + 18(H_{\rm rf}/H_p)^4]\arcsin(H_p/H_{\rm rf})). \end{aligned}$$

Figure 5-20 plots $F(H_{\rm rf})$ with $H_p \equiv 50$ Oe. For comparison, two quadratic curves $\propto H_{\rm rf}^2$ and $\propto (H_{\rm rf} - H_p)^2$ are shown to emphasize the non-quadratic behavior of $F(H_{\rm rf})$ around H_p.

5.5.3 Comparison between Model and Experiment

At each temperature and frequency, R_s^B is determined from the experimentally measured R_s in the following manner. The low-field $R_s(H_{\rm rf})$ is fit to Eq. (5.1):

$$R_s(H_{\rm rf}) = R_s^M(H_{\rm rf}) = R_s(0)[1 + b_R H_{\rm rf}^2]$$

in the low- and intermediate-field regime. In the high-field regime, $R_s^B(H_{\rm rf}) \equiv R_s(H_{\rm rf}) - R_s^M(H_{\rm rf})$ with $R_s^M(H_{\rm rf})$ the extrapolated values of R_s from the low- and intermediate-field regime. The extracted R_s^B, in other words, is simply the deviation

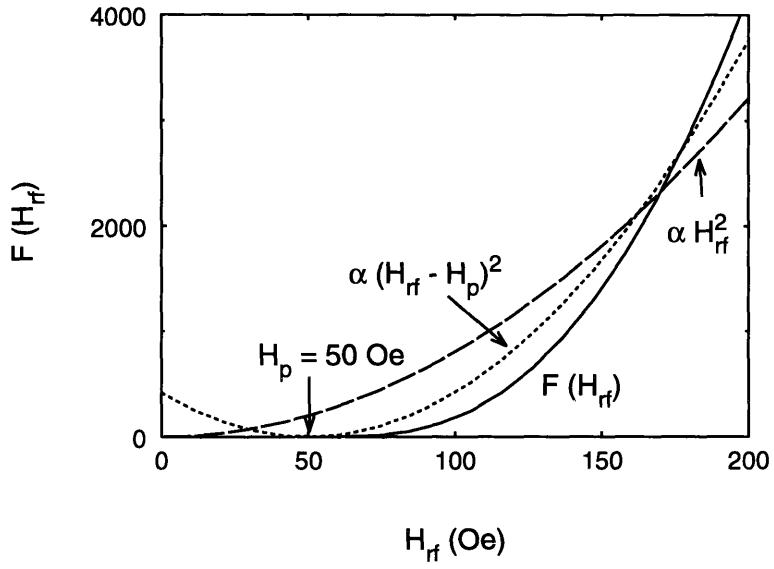

Figure 5-20: Function $F(H_{\rm rf})$ vs $H_{\rm rf}$ with $H_p \equiv 50$ Oe. For comparison, two quadratic curves $\propto H_{\rm rf}^2$ (dashed line) and $\propto (H_{\rm rf} - H_p)^2$ (dotted line) are shown to emphasize the non-quadratic behavior of $F(H_{\rm rf})$ around H_p.

of $R_s(H_{\rm rf})$ from the $H_{\rm rf}^2$-dependent curve.

Figure 5-21 plots R_s^B vs f_0 for several YBCO samples. For each sample, R_s^B is plotted vs resonant frequency at some fixed temperature and rf field value. For most of the samples, $R_s^B \propto f^\alpha$ where α approaches 1, as expected for hysteretic losses [Eq. (5.44)]. For the other samples, no clear frequency dependence is observed as the data are either lacking or too scattered. The solid line is the best least-square linear fit $c_B f^\alpha$, with the fitting parameter c_B, to R_s^B of sample 7. The inset also plots R_s vs f for sample 7 at very low rf field, which exhibit clear f^2 dependence, as expected from the power-dependent coupled-grain model [63]. The solid lines in the inset are the best least-square linear and quadratic fits to the low-field R_s and the high-field R_s^B data, respectively.

Figure 5-22 plots R_s^B vs $H_{\rm rf}$ for sample 1 at $f = 1.5$ GHz at several temperatures. The solid lines are fits using the hysteretic-loss model developed in the previous section [Eq. (5.44)] with two fitting parameters: the vortex-penetration field $H_p(T)$ and the pinning critical current density $J_c^P(T)$. The fits are good over the whole temperature

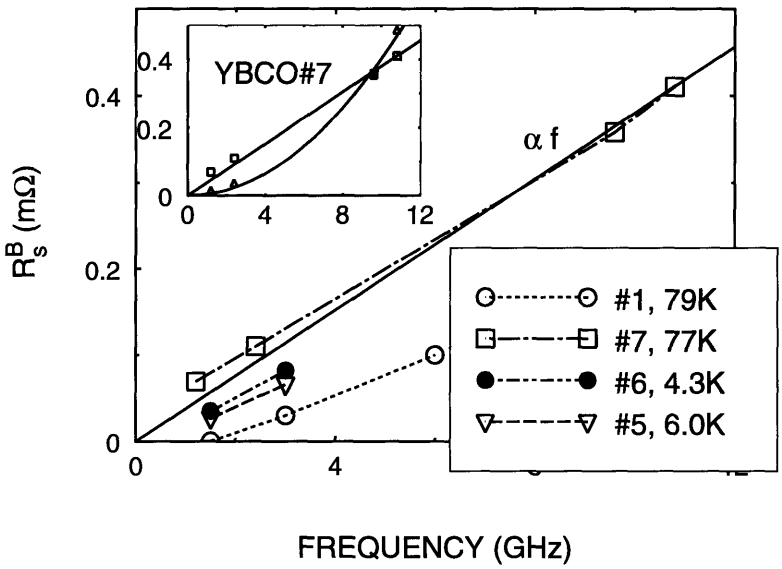

Figure 5-21: The frequency dependence of the surface resistance $R_s^B \equiv R_s - R_s^M$ where R_s is the measured total surface resistance, R_s^M the extrapolated value of the $H_{\rm rf}^2$-dependent R_s from the low and intermediate field region. The extracted R_s^B is attributed to hysteretic losses (see text). For each YBCO sample, the temperature and the rf field value at which R_s^B is extracted are given: sample 1 (○) at 68 Oe, sample 5 (inverted triangles) at 500 Oe, sample 6 (●) at 500 Oe, and sample 7 (□) at 120 Oe. For most of the samples, $R_s^B \propto f^\alpha$ where α approaches 1, as expected for hysteretic losses [Eq. (5.44)]. The solid line is the best least-square linear fit to R_s^B of sample 7. The inset also plots R_s^B (□) vs f (△) for sample 7 at very low rf field. R_s^B for sample 7 exhibits a clear f^2 dependence, as expected from the power-dependent coupled-grain model [63]. The solid lines in the inset are the best least-square linear and quadratic fits to the low-field R_s and the high-field R_s^B data, respectively.

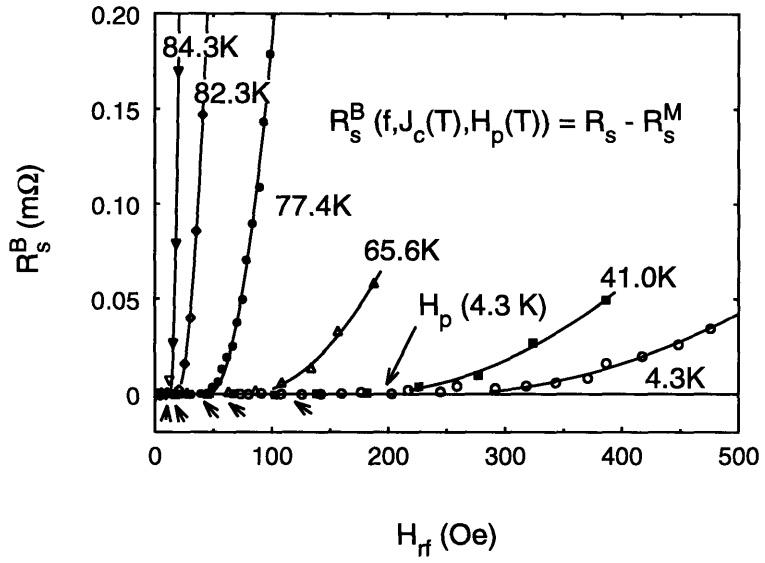

Figure 5-22: The R_s^B vs H_{rf} for sample 1 at several temperatures. The solid lines are fits using a modified Bean critical state model (see text) with two fitting parameters: the vortex-penetration rf field $H_p(T)$, and the pinning critical current density $J_c^P(T)$. The $H_p(T)$ values are indicated at each measurement temperature by the arrows.

range. Similar good fits are also obtained for other YBCO films.

Vortex-Penetration Field $H_p(T)$

The $H_p(T)$ values for YBCO from the hysteretic model are about 30% less than the values estimated by eye in both the ΔR_s vs λ and the ΔR_s vs H_{rf}^2 plots (e.g., Figs. 5-3 and 5-2). These difference between the $H_p(T)$ values obtained from the fits to the hysteretic model and the eye-detected values arise probably because the method of determining H_p by detecting *slight* deviation from the straight lines has large uncertainties. In NbN films where the initial deviation from the H_{rf}^2-curve is much larger (see Fig. 5-4), the H_p values obtained by fitting and the estimated values by eye agree to better than 15% (Fig. 5-4).

Figure 5-23 shows the temperature dependence of the fitting parameter $H_p(T)$ for sample 1 and sample 5. For sample 5, $H_p(T)$ is approximately the same for both mode 1 (1.5GHz) and mode 2 (3.0GHz) over the whole temperature range below T_c.

Figure 5-24 shows the frequency dependence of H_p. For most of the YBCO films,

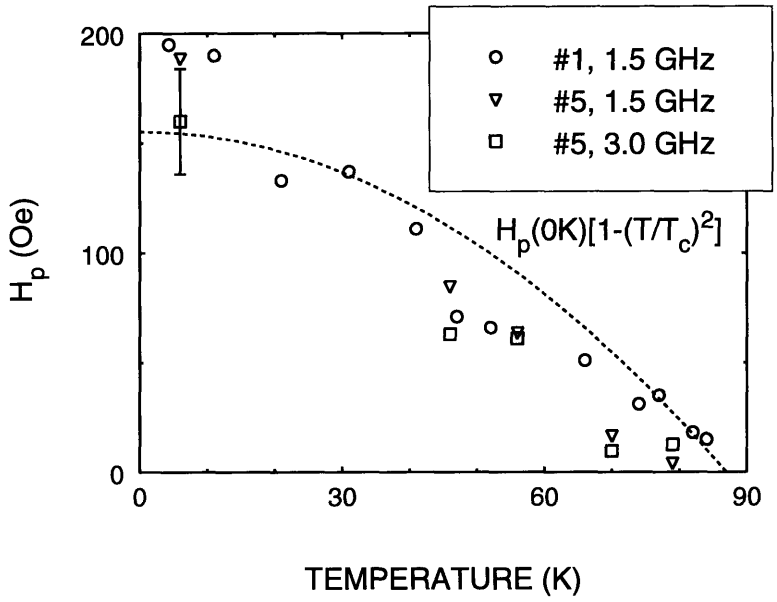

Figure 5-23: The fitting parameter $H_p(T)$, which is the rf-vortex-penetration field, plotted vs temperature for resonators 1 and 5. For sample 5, results for the first two modes at 1.5 GHz and 3.0 GHz are shown. The dotted line is the best fit to the function $H_p(T) = H_p(0)[1 - (T/T_c)^2]$ for sample 1 with $H_p(0)$ a fitting parameter.

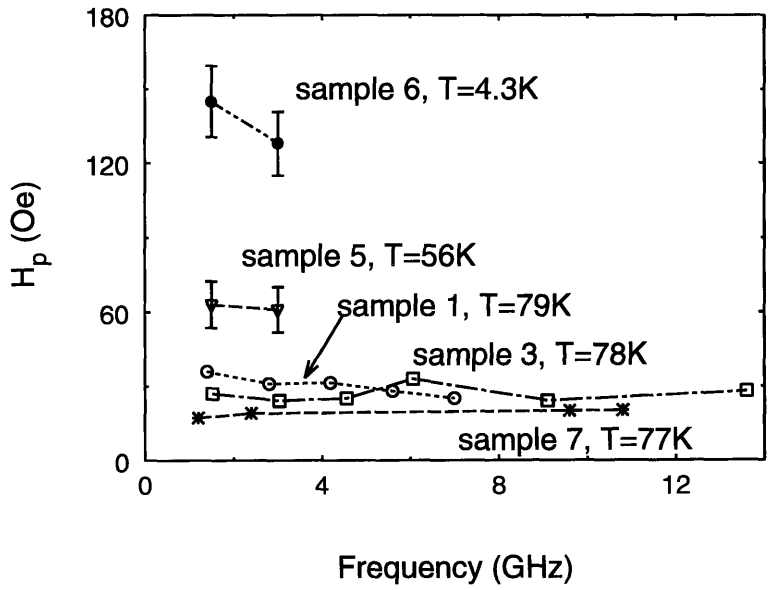

Figure 5-24: The fitting parameter $H_p(T)$ vs resonant frequency for several samples at various temperatures. The scatter of the $H_p(T)$ values is probably the result of the films's non-uniformity (see text).

the values of $H_p(T)$ appear to be independent of frequency for the frequency range considered (< 14 GHz). For some of the samples, which are not shown in Fig. 5-24, H_p as a function of frequency exhibits a large amount of scatter that is probably the result of the films's non-uniformity. For different resonant modes, the peaks of the resonant standing waves are located at different places along the length of the stripline. For nonuniform films, the field values for vortex penetration may be different at different locations of the films, which would lead to different H_p values for different resonant modes.

The values of $H_p(T)$ obtained here are lower than $H_{c1}^{\perp c}$ which are already much lower than $H_{c1}^{\parallel c}$, where $H_{c1}^{\perp c}$ (~ 250 Oe at 0 K) and $H_{c1}^{\parallel c}$ (~ 850 Oe at 0 K) are the lower critical field values measured in YBCO single crystal [86] and epitaxial films [106, 107] with an applied dc magnetic field perpendicular and parallel to the c-axis, respectively. Using the anisotropic Ginzburg-Landau model, Klemm [108] calculates the lower critical field $H_{c1}(\theta_H)$ where θ_H is the angle between the c-axis and the dc applied field. He finds that $H_{c1}(\theta_H)$ decreases rapidly for $\theta_H > 10°$. The decrease of $H_{c1}(\theta_H)$ with increasing θ_H for YBCO has also been observed experimentally [109, 110]. That our H_p values reflect $H_{c1}^{\perp c}$ more than $H_{c1}^{\parallel c}$ can be attributed to the high curvature of the stripline's rf-field lines, especially around the edges (Fig. 5-25).

For a YBCO film of thickness 0.3 μm and $\lambda(T) = 0.2$ μm, the maximum magnetic field at the corners of the center strip with cross-section 0.2 μm $\times$ 150 μm makes an angle $\theta_H \simeq 20°$ with the c-axis [81].

Since the penetration field H_p for a YBCO c-axis film is suppressed towards $H_{c1}^{\perp c}$ values by the *average* field curvature, H_p is expected to be higher for thicker films which have less *average* curvature. The thickest YBCO sample 4 (Table 5.1) has an H_p ($\simeq 380$ Oe at 36 K and $\simeq 102$ Oe at 77 K) about 3 times larger than those of thinner YBCO films, in agreement with the simple picture of field curvature.

That the $H_p(T)$ values for YBCO thin films obtained are low even when compared with the intrinsic $H_{c1}^{\perp c}$ of YBCO single crystals [86] can be also attributed to lower vortex-penetration fields for the junction defects and grain boundaries in the films where vortices first penetrate. Thus in YBCO thin films, both the strong field curva-

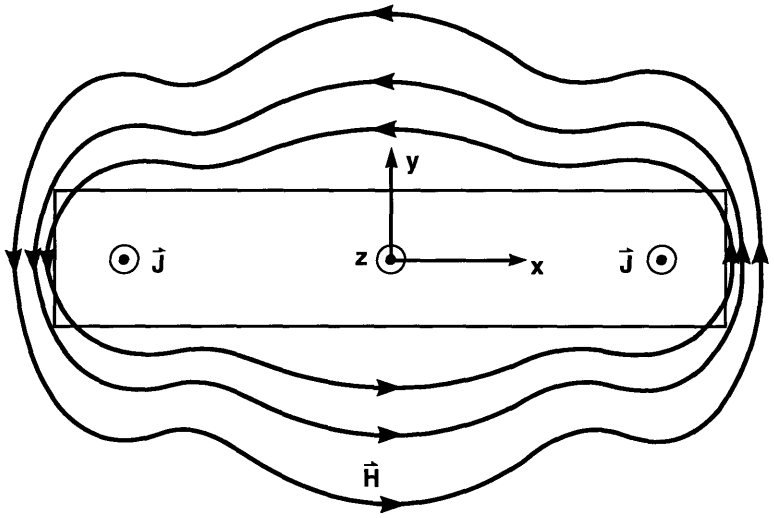

Figure 5-25: Schematic showing the current-induced rf magnetic field around the cross-sectional area of a superconducting strip in the Meissner state carrying an rf current (out of the page). The rf magnetic field lines are strongly curved, especially around the edges. Though some field lines penetrate the thin strip, no vortices are formed yet at sufficiently low magnetic field. The field contour lines bulge at the two ends where the current density is highest.

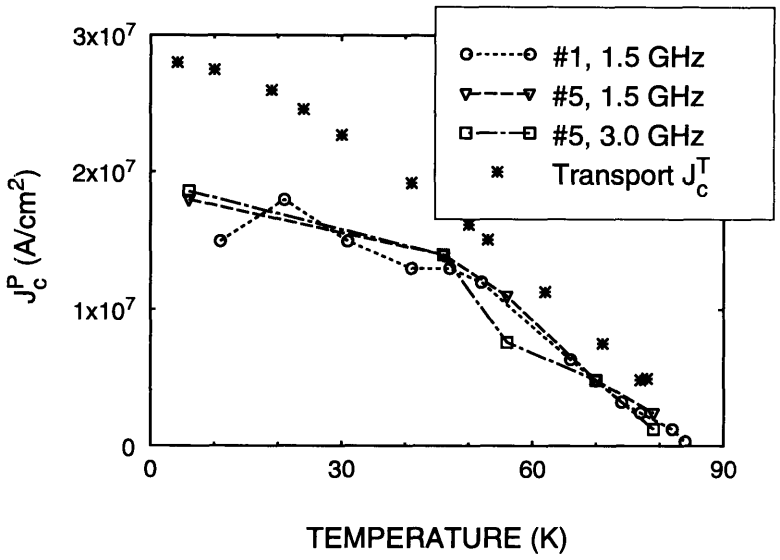

Figure 5-26: The fitting parameter $J_c^P(T)$ which is the pinning critical current density vs temperature for resonators 1 and 5. The dashed lines are guides to the eye. For resonator 5, the first two modes at 1.5 GHz and 3.0 GHz are shown. The dc critical current density, as obtained by dc transport measurements on a film deposited under the same conditions as YBCO sample 1, is also shown (asterisks) for comparison.

ture and defects and grain boundaries may be working together to lower the $H_p(T)$ values.

Pinning Critical Current Density $J_c^P(T)$

Figure 5-26 plots the second fitting parameter $J_c^P(T)$ from the modified Bean model for samples 1 and 5. Despite the simplicity of the Bean model, values of the fitting parameter $J_c^P(T)$ for sample 1 agree well both in amplitude and temperature-dependence with the critical current density J_c^T obtained by dc transport measurement on a film deposited under exactly the same conditions. (J_c^T cannot be measured in the sample 1 used for the resonator, but J_c^T is available for a sample deposited under the same conditions and this is shown in Fig. 5-26). For sample 5, the $J_c^P(T)$ values extracted for two different modes, mode 1 at 1.5 GHz and mode 2 at 3.0 GHz, are nearly identical.

The $J_c^P(T)$ values are about an order of magnitude larger than the fitting param-

eter $J_c(T)$ extracted from the fits using the power-dependent coupled-grain model in the low- and intermediate-field region [63] for the same films. This difference can be explained as follows: The $J_c(T)$ in the power-dependent coupled-grain model reflects the critical current density of a resistively shunted Josephson junction, whose temperature-dependence follows the Ambegaokar functional form [63]. This $J_c(T)$ is directly related to the lower critical field of the junction (i.e., the vortex-penetration field) [96] and has nothing to do with vortex pinning. On the other hand, $J_c^P(T)$ reflects the vortex pinning strength [44, 103] ($J_c^P \propto U$). Vortices start to penetrate for current densities larger than J_c, but the magnitude of the hysteretic losses is determined by J_c^P, as shown in Eq. 5.44. The transport J_c^T measures the sum of the junction J_c and the pinning J_c^P. In the limit of strong pinning, $J_c^P \gg J_c$ and hence $J_c^T \simeq J_c^P$. Our result $J_c^T \simeq J_c^P \gg J_c$ implies strong vortex pinning for YBCO, consistent with other vortex-pinning measurements which reveal strong pinning forces in YBCO (see for instance, Wu and Sridhar [86]). In the limit of weak pinning, $J_c^P \ll J_c$ and hence $J_c^T \simeq J_c$. Since the NbN films are highly granular as observed via transmission electron microscopy (with average grain size of about 0.02μm), I expect weak pinning for Josephson vortices moving along each junction, because the order parameter is suppressed there [111]. For NbN sample 1 at 13.4 K (Fig. 5-27), the effective critical-current density of the junction is $J_c \simeq 5.8 \times 10^5$ A/cm^2, as obtained from the fit using the power-dependent coupled-grain model [63] for the low- and intermediate-rf-field regime, whereas the pinning J_c^P is $J_c^P \simeq 1.2 \times 10^5$ A/cm^2, as obtained from the fit using our hysteretic-loss model [Eq. (5.44)]. These are to be compared with the measured dc transport J_c^T values of 0.7 to 6.7×10^5 A/cm^2 at 13.4 K for several granular NbN films.

That $J_c \gg J_c^P$ for NbN compared with $J_c \ll J_c^P$ for YBCO gives rise to the abrupt change in the R_s and λ vs $H_{\rm rf}$ curves for NbN films at H_p, but only a gradual change for YBCO films. To see more clearly how the abrupt change in NbN comes about, consider the limit of *zero* vortex pinning: As soon as the induced field exceeds the vortex-penetration field H_p of the film, vortices would penetrate the sample *everywhere*, in the absence of macroscopic shielding current arising from pinning. This

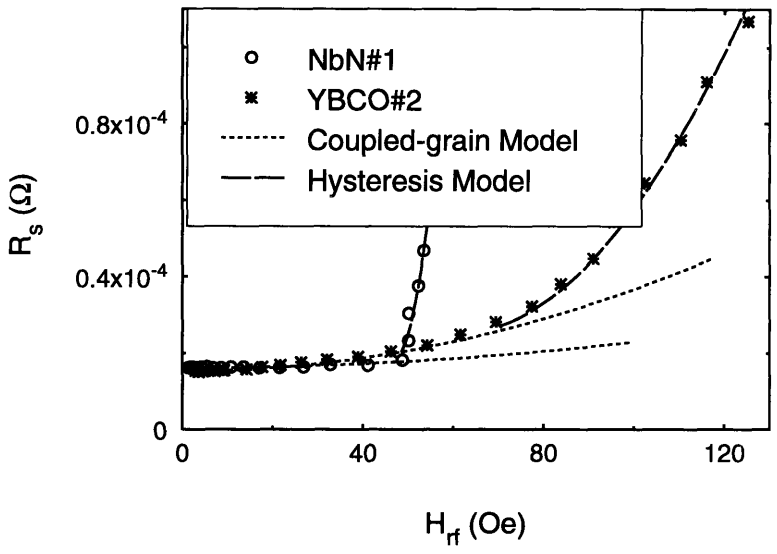

Figure 5-27: Comparison between YBCO (asterisks) and NbN (o) films. The R_s vs H_{rf} are plotted for YBCO sample 2 (at 1.5 GHz) and for NbN sample 1 (at 1.7 GHz) at similar reduced temperatures $T/T_c \simeq 13.4$ K/15.3 K $\simeq$ 78 K/90 K $= 0.867$. The dotted lines are fits to the power-dependent coupled-grain model [63] for the low- and intermediate-rf-field region. The dashed lines are fits to a modified Bean critical state model.

sudden influx of vortices would produce sharp changes in the pair density and in the losses, and hence in λ and R_s, respectively.

5.5.4 Summary

I have measured the microwave surface impedance as a function of the microwave magnetic field at various temperatures and frequencies for several types of YBCO films of different thicknesses and for NbN films. For both YBCO and NbN, $R_s(H_{rf})$ and $\lambda(H_{rf})$ can be divided into two regions: 1) the low and intermediate rf field region and 2) the high rf field region. The value of H_{rf} that separates the two regions is the vortex-penetration field $H_p(T)$. In the low- and intermediate-field region, the power-dependent coupled-grain model (for the Meissner state) quantitatively accounts for the power dependence of both YBCO and NbN films, giving $R_s \propto f^2$ and $\Delta R_s \propto H_{rf}^2$.

In the high-field region, both $R_s(H_{rf})$ and $\lambda(H_{rf})$ deviate from the low-field quadratic dependence on H_{rf}^2. Using a modified Bean model ($H_p > 0$), I adapted Norris's cal-

culations to account quantitatively for the behavior of $R_s^B(H_{rf})$ for most YBCO and NbN films at various temperatures and frequencies with two fitting parameters $H_p(T)$ and $J_c^P(T)$. The measured R_s^B is found to be nearly proportional to frequency for several samples. While I think I have strong evidence that $R_s^B \propto f$, some samples did not show a clearly defined frequency dependence, probably because of film non-uniformity as discussed in Sec. 5.5.3. The frequency dependence of R_s^B hence requires further study to understand the effect of non-uniformity.

The values of $H_p(T)$ obtained show vortex penetration occurring at field values closer to the dc $H_{c1}^{\perp c}$ than to the $H_{c1}^{\parallel c}$ values. This behavior of $H_p(T)$ can be explained by the curvature of the magnetic fields at the edge of a superconducting thin-film strip. That the $H_p(T)$ values for YBCO thin films obtained are low even when compared with the intrinsic $H_{c1}^{\perp c}$ of YBCO single crystals [86] may be attributed to lower vortex-penetration fields for the junction defects and grain boundaries in the films where vortices first penetrate. The field H_p is therefore an extrinsic quantity, leaving room for improvement of the power-handling capability of the films through improved deposition techniques.

The values of $J_c^P(T)$ extracted from the fits using the hysteretic-loss model agree with the critical current densities $J_c^T(T)$ obtained by dc transport measurements for YBCO but not NbN films. The disagreement for NbN can be explained by considering the effects of strong vs weak pinning on the J_c^T values. The strong pinning in YBCO and the weak pinning in NbN also are shown to be responsible for the qualitatively different behavior in R_s above H_p.

The use of the critical-state model to calculate hysteresis losses has been done before. Easson and Hlawiczka [112] measured a.c. dissipation in smooth-surface bulk Nb and used the modified Bean critical-state model successfully to explain their data. Recently, Sridhar [113] applied the formalism by Norris [102] to calculate hysteretic losses in an isolated strip at the microwave frequencies. Sridhar's approach, however, differs from my approach in this work in that he assumes that microwave vortices penetrate the film as soon as the rf field is induced. In other words, H_p is assumed to be zero, which disagrees with the results of the discussion presented in Appendix

A of this work.

5.6 Conclusion and Discussions

I have presented the complete characterization of $Z_s(f, T, H_{rf})$ for high-quality YBCO thin films. At each temperature and frequency, the $Z_s(H_{rf})$ curves can be divided into two regions. In the low- and intermediate-field region, R_s and λ have a quadratic dependence on H_{rf}, which can be accounted for by the power-dependent coupled-grain model. In the high-field region, $R_s(H_{rf})$ increases faster than H_{rf}^2 and can be explained by a hysteretic critical-state model. The field value at which the faster increase becomes noticeable is the same value as the point where the resonant curves becomes non-Lorentzian and that point is identified with the beginning of rf vortex penetration. In the high-field region, the frequency dependence of R_s appears to change from $R_s \propto f^2$, which holds for the intermediate-field region, over to a dependence $R_s \propto f$.

Despite their simplicity, both the power-dependent coupled-grain and the hysteresis models explain simultaneously Z_s as a function of frequency, temperature, and rf field remarkably well for various types of superconducting films of different thicknesses. In the following, I will remark on the validity of the two models and how they relate to real physical mechanisms.

5.6.1 Validity of the Coupled-Grain Model

As discussed in Chapter 2, many structural defects exist in a superconductor. For high-T_c materials, these defects tend to play an especially important role in determining the transport properties because of the extremely short coherence lengths and the higher operating temperatures which promote scattering. Twin-boundary defects have been shown to have little effect on the surface impedance [114], among all the common defects in high-T_c superconductors such as point defects, line and plane defects, stacking faults, and a-axis. Like the possible existence of noncondensating normal carriers, point defects can account for the large residual surface resistance in high-T_c superconductors. Nevertheless, as I calculated, they contribute little to the

strong power dependence observed in these materials. Though a-axis grain-boundaries can behave as very weak links, their contribution to the microwave losses is probably small because there are very few of them in high-quality c-axis films. Thus stacking faults and plane defects appear to be the most important defects determining Z_s. In a typical high-T_c film, stacking faults and line and plane defects are dissimilar, randomly distributed with all possible planar orientations. Furthermore, the size of these structural defects can vary greatly. It is therefore oversimplifying to model them as a uniform array of junctions as in the coupled-grain model. Nevertheless, the coupled-grain model does contain the essential features and serves well as a basis for a more complex model.

A relatively simple and immediate improvement that can be made on the power-dependent coupled-grain model is to assume elongated (along the current direction) instead of cubic grains. The physical justification for this is two-fold. First, non-cubic grains are more realistic as there is little correlation among the defect size and the distance between defects. Second, not every defect along the current direction contributes significantly to the transport characteristics. In other words, the junctions along the current direction can merge to form long elongated grains. With elongated grains, I red-id the fits of the power-dependent coupled-grain model to the data for sample 1 in Table 5.2. Assuming the same grain size (3.5 μm) perpendicular to the current direction and the same grain thickness as the film thickness (0.3 μm), I obtained identically good fits with the new junction resistance $R_J \simeq 12\ \mu\Omega$ which is much closer to the values obtained from measurements by others on single grain-boundary junctions [94, 95]. The critical current density $J_c(T)$ turned out to be the same as for the cubic-grain power-dependent coupled-grain model since the fitting parameter $J_c(T)$ depends only weakly on the grain size and shape.

One of the oversimplification of the coupled-grain model is that it assumes the grain boundaries span in a piecewise manner across the whole width of the films. In this assumption, a current must traverse the grain boundaries since they are in series with the grains. Structural defects in high-quality epitaxial superconducting films, however, do not span the films. Consequently, a current can bypass the defects via

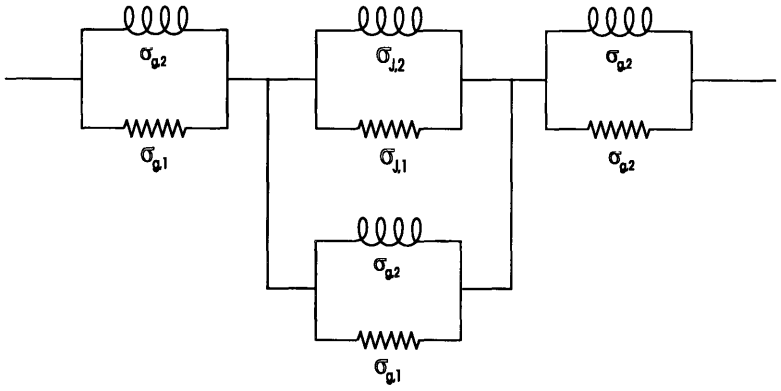

Figure 5-28: Circuit showing a possible improvement of the power-dependent coupled-grain model. A shunting path represented by a parallel resistor and inductor with the same values as those of the grain is added in parallel to the junction's resistor and inductor.

the parallel grains, at least at dc or low frequencies. At high frequencies such as the microwave frequencies, the inductivity instead of resistivity of the film determines the path of the traversing current, and shunting therefore occurs less often if the defects act like strongly coupled junctions (with large J_c). The power-dependent coupled-grain model applies well at microwave-frequencies probably because of this lack of wholesale shunting of defects. An obvious improvement of the model would be to add a resistor and inductor reflecting a superconducting grain in parallel to the junction as shown in Fig. 5-28. Further improvement can be made by introducing a distribution for the resistances and inductances of the junctions and the grains.

5.6.2 Validity of the Hysteretic Model

At high rf fields, vortices enter the superconductor, and the coupled-grain model dealing only with the Meissner state must be generalized to account for vortices. Because of the weaker superconductivity in the junctions, vortices tend to penetrate the grain boundaries first. As the rf-field amplitude increases, vortices then enter the grains. The hysteretic model I have presented is the first step in an attempt to describe these rf vortices and the associated losses by treating the sample as an effective uniform medium, making no distinction between junction and grain vortices. This

neglect of the two different types of vortices is partially justified since the critical-state model applies equally well to both types of vortices, though immediate improvements can be made by trying a more complex critical state model, such as the Kim model. A more realistic model should distinguish between the two types of vortices and their different motions (e.g., junction vortices prefer to move along rather than out of the junctions), and give a distribution to the pinning potentials.

5.6.3 SQUID Measurements

Even though the structural defects can be observed by the various characterization techniques such as SEM, TEM, X-ray analysis, STM, etc., the importance of these defects on the transport properties can not be assessed by such techniques. Magnetization measurements, on the other hand, provide a means to directly probe the structural defects in a superconductor. The main concept is as follows. From the critical state model, the critical current density J_c^P is related to the dimension of the effective shielding diameter of the sample. Given a hysteretic loop of magnetization vs the (low-frequency) ac applied magnetic field, J_c^P can be derived directly from the effective shielding diameter. Specifically, from the Bean critical-state model:

$$J_c^P(H) = 30[M_+(H) - M_-(H)]/D \tag{5.46}$$

where M_+ [emu/cm^3] and M_- [emu/cm^3] are the upper and lower points on the hysteretic loop at the same ac magnetic-field amplitude H, and D [cm] the effective shielding diameter. Figure 5-29 illustrates the relation between J_c [A/cm^3] and the average grain size. At the top of the figure is a typical hysteretic loop. At one extreme, for a superconducting film of perfect crystallinity (Case 1 of Fig. 5-29), or nearly perfect with very strongly coupled junctions, the effective shielding diameter D that enters Eq. 5.46 should be about the size L of the whole sample. At the opposite extreme where the film is very granular with either independent grains or very weakly coupled junctions (Case 2), D is of the order of the average physical grain size a. A real superconducting film is expected to lie between these two extremes (Case 3) yielding

D between the average grain size a and the overall sample size L. Thus by measuring the ac hysteretic loops, the effective shielding diameter, which can be regarded as a form of effective grain size, can be obtained, yielding valuable information concerning the contributions of the structural defects in the sample.

Figure 5-30 presents a typical hysteretic loop of magnetization versus applied magnetic field for an off-axis YBCO film of 0.3 μm thickness on $LaAlO_3$ at 5 K. The data were obtained with a SQUID. The Bean model applies only at magnetic fields much higher (greater than about 1 Tesla here) than the lower critical field H_{c1}, where the shielding effects from the surface current become unimportant.

Using Eq. 5.46, J_c^P is plotted as a function of the applied ac magnetic field H in Fig. 5-31 for different values of D. From the figure, $J_c^P(H)$ shows a strong dependence on H compared with the critical current density I measured on a YBCO single crystal. This strong magnetic-field dependence suggests the existence of defects acting like weak links in the YBCO film. If I picked the effective shielding size D to be around 10 μm, the corresponding J_c^P would be larger than 10^9 A/cm^2 at $H = 1$ Tesla, which is unrealistically large compared with all the values obtained by other methods (for example, from my transport measurements). With $D \simeq 4$ mm, a reasonable value $J_c^P \simeq 0.8 \times 10^7$ A/cm^2 is obtained at $H = 1$ Tesla. That the effective shielding diameter D is only slightly less than the sample size of 5 mm suggest that the junctions in the measured films are strongly coupled, as assumed by the power-dependent coupled-grain model.

5.7 Intermodulation Products

5.7.1 Introduction

Nonlinear effects in superconducting materials lead to harmonic generation. Direct observation of harmonic generation in a stripline resonator is impossible since the resonant frequencies of the overtone modes are not exactly integer multiples of the fundamental frequency, owing to a small amount of dispersion of the line. The

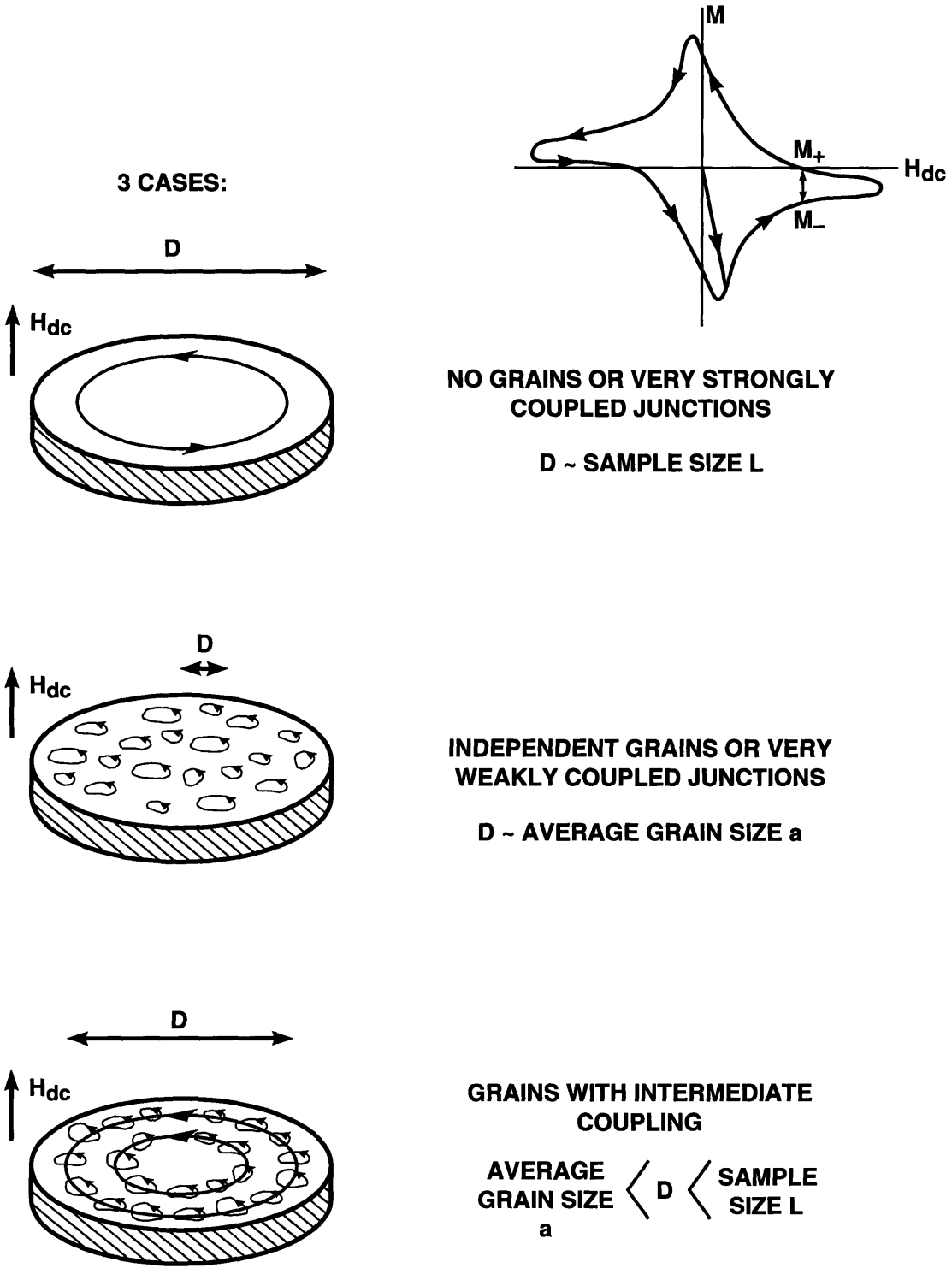

Figure 5-29: Illustrations of the relation between the pinning critical current density and the effective film diameter D.

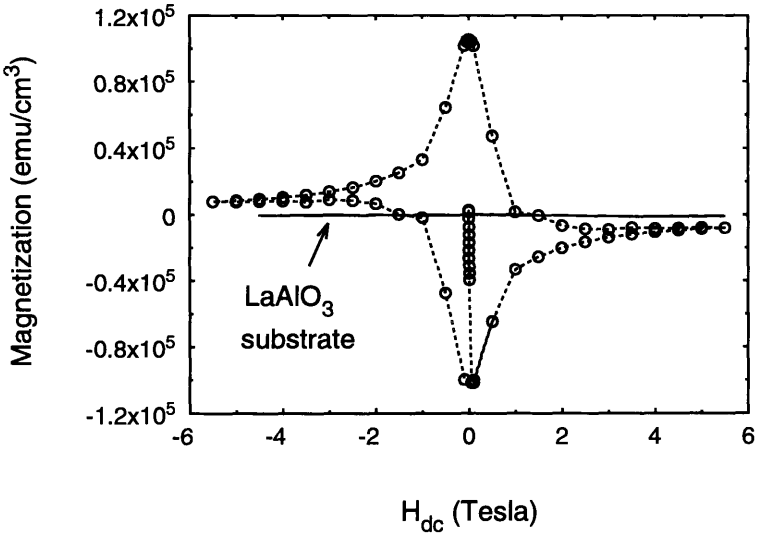

Figure 5-30: Hysteretic loop for an off-axis smooth YBCO film of 0.3 μm thickness on $LaAlO_3$ at 5 K. The data were obtained with a SQUID.

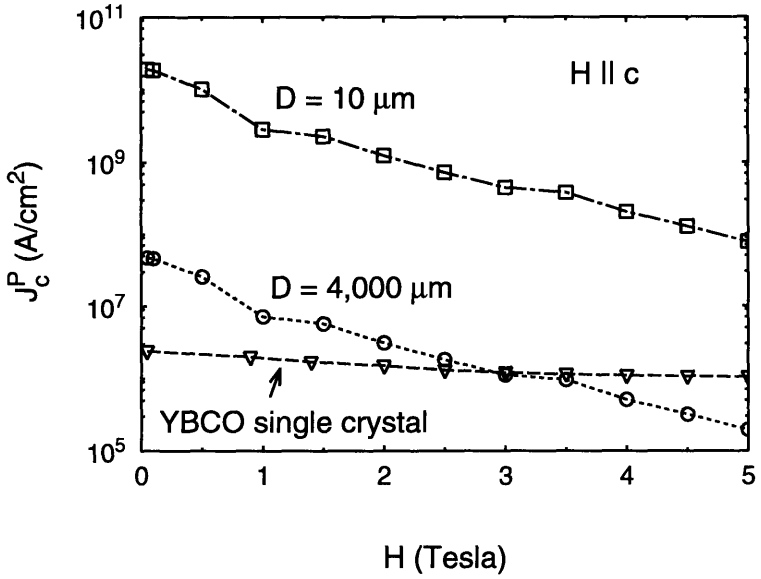

Figure 5-31: J_c^P obtained from the hysteretic loop using the Bean model. Two different values of J_c^P are shown for two different selected effective shielding diameters D. The transport critical current density for a YBCO single crystal is also shown (inverted triangles) for comparison.

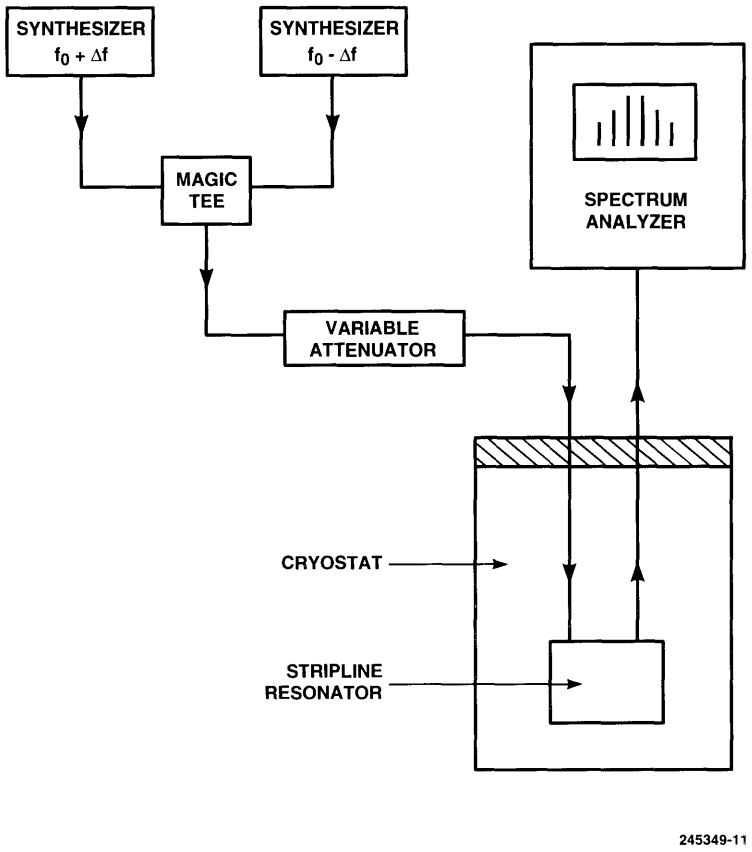

Figure 5-32: Setup for intermodulation measurement.

nonlinearity responsible for harmonic generation can, however, be observed by intermodulation (IM) product measurements. As shown in Fig. 5-32, IM product measurements are performed by combining two input signals of frequencies $f_1 = f_0 + \Delta f$ and $f_2 = f_0 - \Delta f$ from two synthesizers. Δf is chosen to be less than half of the 3-dB bandwidth. The IM products of frequencies $2f_1 - f_2$, $2f_2 - f_1$ (third-order IM), $3f_2 - 2f_1$, $3f_1 - 2f_2$ (fifth-order IM), etc., can be observed within the bandwidth of the mode by a spectrum analyzer. IM products are highly important in practical devices such as filters, where IM distortions limit the range of operating power. I am including here the measurements of the IM product at various temperatures for both YBCO and NbN thin films, because IM generation can occur only if the nonlinear effects are fast, i.e., a nonlinear response follows the microwave frequency with a time constant less than 10^{-10} s. Thermally generated nonlinear effects, for instance, will not produce IM products, because of the much lower speed associated with thermal time constants ($\leq 10^{-4}$ s). Thus the observation of IM generation confirms that the observed nonlinear Z_s behavior is due to true microwave-frequency nonlinearities and is not simply the result of heating even on a local scale [78].

5.7.2 IM Results

Figure 5-33 plots the output power of the fundamental and of the third-order IM product versus the input power of the stripline resonator sample 4 at 77 K and 1.53 GHz.

The output power of the fundamental below about -5 dBm follows a straight line of slope 1, as expected. Saturation takes place for the fundamental above -5 dBm. Below about -10 dBm, the third-order IM products also have the expected slope 3. Above -10 dBm, the IM signals quickly saturates, signifying strong nonlinearity. The IM behavior appears to correlate with the nonlinear behavior of $Z_s(H_{rf})$. The saturation of the IM products is consistent with the sharp rise in R_s, which causes a large increase in the losses in the stripline, hence attenuating all signals including the IM products. Figure 5-34 shows similar data from the same resonator as in Fig. 5-33 at a different temperature $T = 4.3$ K. Though the fundamental now still follows the

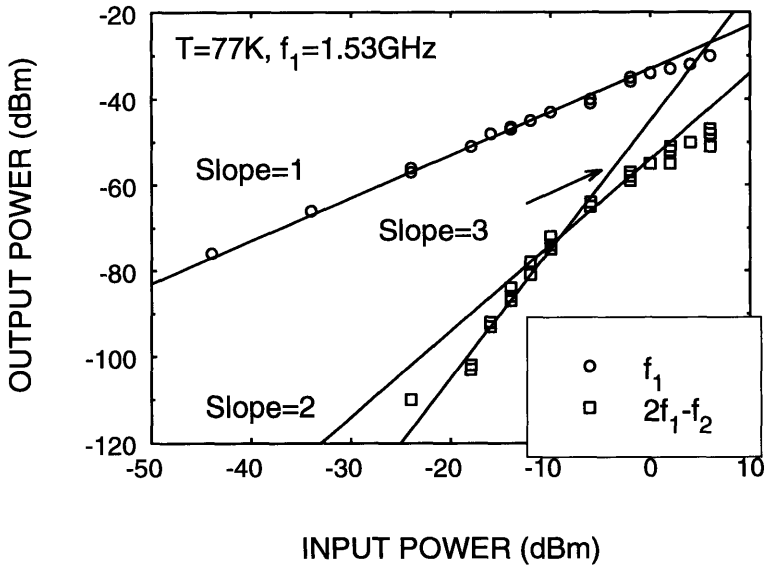

Figure 5-33: Output power vs input power for the fundamental and the third-order IM products for stripline resonator sample 4 at 77 K and 1.53 GHz.

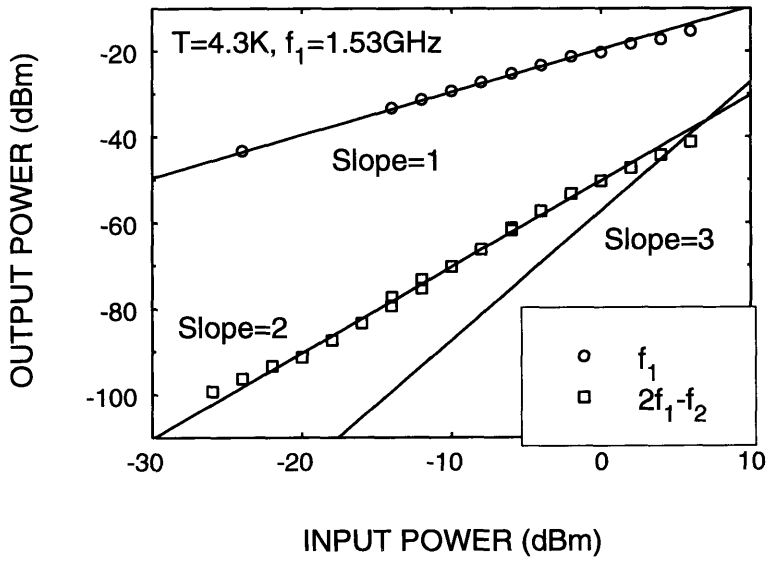

Figure 5-34: Output power vs input power for the fundamental and the third-order IM products for sample 4 at 4.3 K and 1.53 GHz.

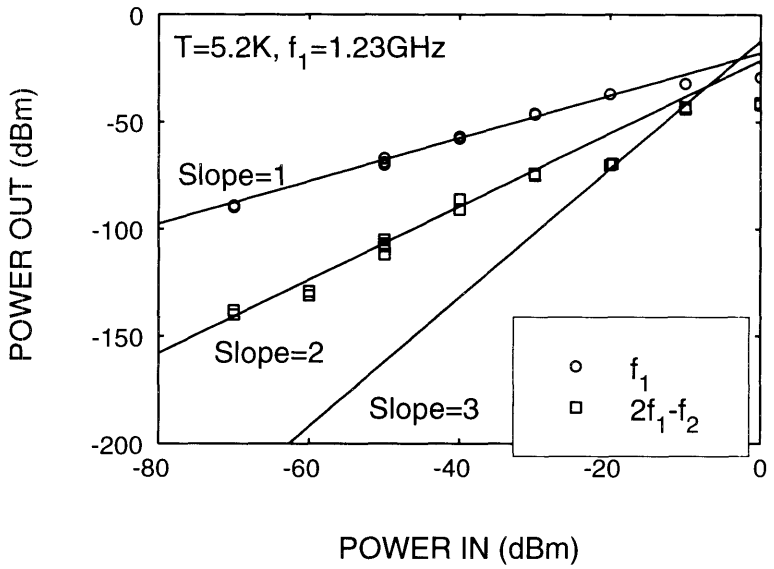

Figure 5-35: Output power vs input power for the fundamental and the third-order IM products for sample 7 at 5.2 K and 1.23 GHz.

same slope 1 as expected, the third-order IM products follows a slope of 2 or slightly less, suggesting that the nonlinearity remains strong throughout the entire range of measured input power.

Similarly, the third-order IM products for sample 7 also show a slope of 2 over the entire input power range that was measured (Fig. 5-35). One sees that the third-order intercept in sample 4 is more than 10 dB higher than that of sample 7 around 5 K. This demonstrates that a lower $H_{\rm rf}$ dependence (e.g., sample 4) improves practical performance, as expected.

Chapter 6

Microwave Properties of High-T_c Josephson Junctions

In the previous chapters, I have demonstrated that extended defects, acting like resistively shunted Josephson junctions, play an essential role in determining the microwave properties of a high-T_c superconductor. These junctions were treated as identical elements in a regular array in the power-dependent coupled-grain model. Junctions in a real superconductor, however, are nonuniform; and any treatment that models them as identical consequently can yield only average properties. A deeper understanding of the behavior of the surface impedance of high-T_c superconductors hence require detailed knowledge of single high-T_c Josephson junctions whose properties are still poorly understood, especially their microwave properties. High-T_c Josephson junctions also deserve to be investigated on their own right because they can provide clues to the superconducting mechanisms in high-T_c materials and their potential for application is important (e.g., for SQUID applications). Some important issues for the basic study of high-T_c Josephson junctions are: 1) structure: SNS weak-link (i.e., non-tunnel) or SIS tunnel junction type or some other, 2) the effects of the barrier type and interface quality on the junction properties, 3) the mechanisms of the supercurrent and quasiparticle-current passage, and 4) the reasons for the low I_cR_n products.

Josephson junction grain boundaries are among the high-T_c junctions most often

studied. Investigation of natural grain-boundary junctions (GBJ) occurring in high-T_c films is difficult, since such junctions are dissimilar and randomly distributed. As a result, many artificial grain boundaries have been fabricated for study by different techniques: bicrystal, biepitaxial, and step-edge [114]. Besides GBJs, other types of junctions have also been made and measured. In this chapter, I report measurements on $YBa_2Cu_3O_{7-x}$ Josephson edge junctions prepared by *in situ* laser ablation deposition. The chapter is divided as follows. I will start with experimental design together with the fabrication of the measured edge junctions. The reader who is unfamiliar with the basic properties of Josephson junctions is referred to the vast relevant literature, including the popular book by van Duzer and Turner [87] and the excellent review by Likharev [115]. Next, I will present measurements and analysis and then summarize my results at the conclusion of the chapter.

6.1 Experimental Design and Fabrication

Figure 6-1 illustrates one of my designs for studying the microwave properties of Josephson junctions. The junction is positioned at the midpoint of the center conductor. Since the rf current of the odd resonant modes also peaks at the midpoint, the junction exerts maximum influence on these modes. On the other hand, the even resonant modes should be completely unaffected by the presence of the junction because these modes have a current node at the midpoint. Thus, by measuring both the odd and even modes of the stripline with an incorporated Josephson junction, I am able to isolate the properties of the junction and compare them with the properties of the film.

The edge junctions YBCO/YBCoCO/YBCO were prepared by Koren *et al.* at the Technion-Israel Institute of Technology, where multiple targets and externally manipulated stainless steel contact masks were used in an *in-situ* laser-ablation deposition process [116, 117, 118]. Figure 6-2 shows a cross section of the edge junction. The base YBCO film about 0.15 μm thick is first deposited onto (100)$LaAlO_3$ substrate at 790°C. A narrow insulating YBCoCO stripe is then deposited on top of the base

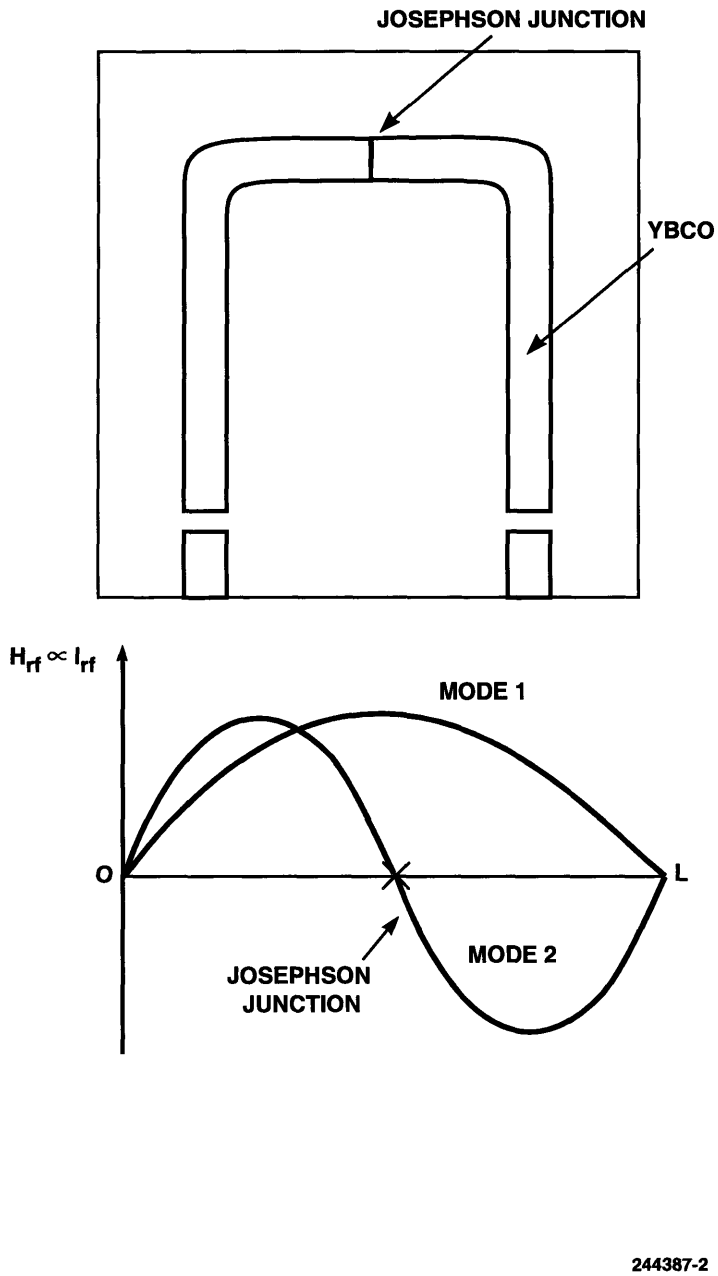

Figure 6-1: Josephson junction fabricated at the midpoint of the center conductor of a stripline resonator. Only the odd resonant modes whose rf currents peak at the midpoint are altered by the junction. The even modes whose rf currents have a node at the midpoint should be unaffected.

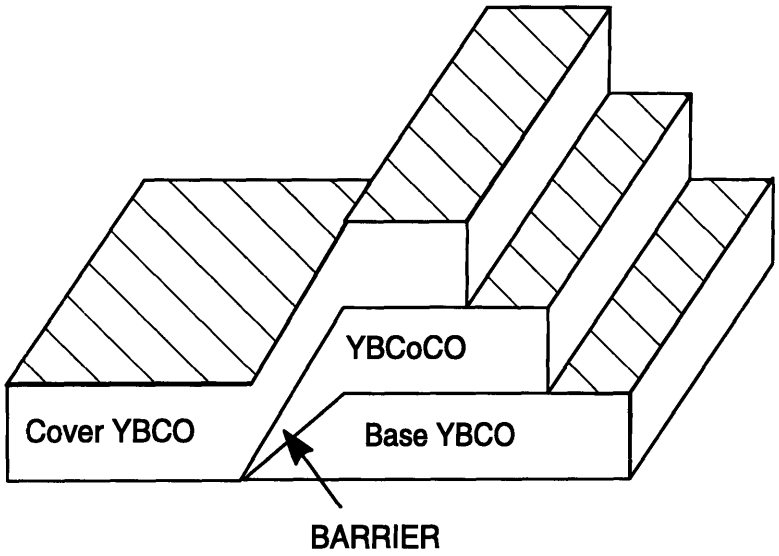

Figure 6-2: Cross section of a photolithographically prepared Josephson edge junction.

YBCO, including the slanted edge. The YBCoCO portion that covers the slanted edge of the YBCO base is wedge-shaped, which acts as a barrier. As the barrier, YBCoCO serves as a good insulator [$\rho(77\text{K}) \simeq 1\ \Omega\text{cm}$], which is compatible with YBCO in multilayer growth and acid etching processes. Finally, a cover YBCO film of the same thickness as the base is deposited on the uncoated half of the wafer just slightly overlapping the base and the insulating layer.

Patterning was performed with standard photolithography, and 0.25% phosphoric acid etch, which removes both YBCO and YBCoCO equally well.

6.2 Experimental Results and Discussions

Figure 6-3 plots the resistance of a YBCO/YBCoCO/YBCO edge junction as a function of temperature. The onset of phase coherence across the junction is around 86 K with the junction resistance equal to zero around 80 K. The junction critical current is $I_c \simeq 90\ \mu\text{A}$ and the shunt resistance is $R_J \simeq 200\ \text{m}\Omega$ at 42 K.

Figure 6-4 shows the I-V curve of the same edge junction. This curve is well-explained by the resistively shunted junction (RSJ) model with excess current, with

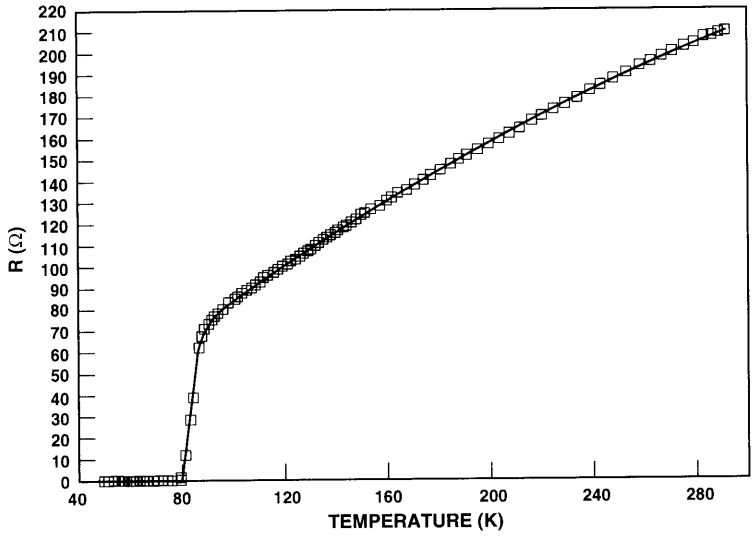

Figure 6-3: R vs T of a YBCO/YBCoCO/YBCO edge junction (see text).

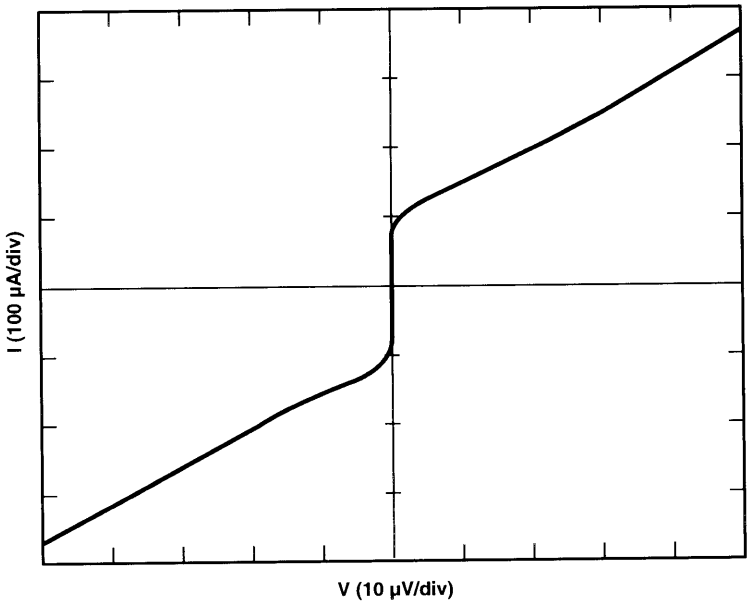

Figure 6-4: I-V curve of a YBCO/YBCoCO/YBCO edge junction.

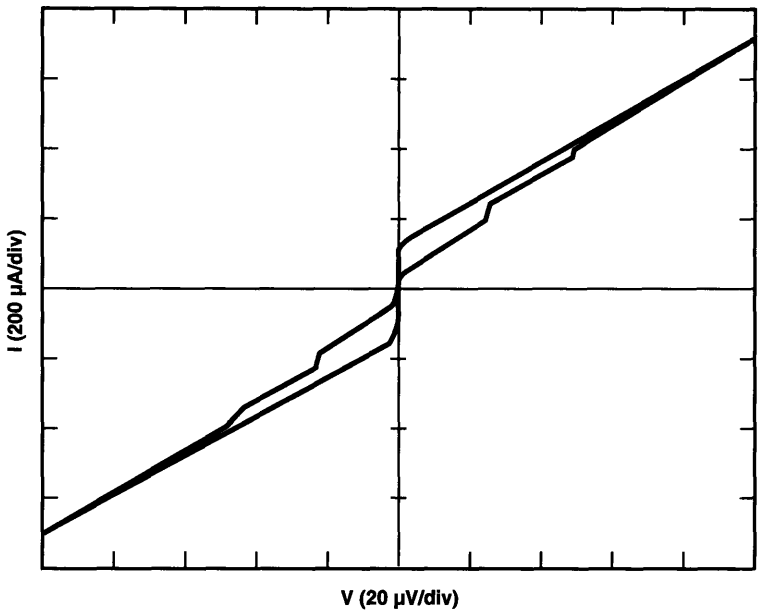

Figure 6-5: Shapiro steps of a YBCO/YBCoCO/YBCO edge junction. The smooth curve with no step is the I-V curve with no microwave irradiation.

$I_c \simeq 85$ μA and $R_J \simeq 200$ mΩ at 51 K. Sharp Shapiro steps, a clear signature of a working Josephson junction, are also observed in Fig. 6-5 from the film under microwave irradiation at 10 GHz.

The temperature dependence of a YBCO/YBCoCO/YBCO edge junction for $1/Q_u$ with Q_u the unloaded quality factor, and resonant frequency f_0 of the fundamental (odd) mode at 2.1 GHz is shown in Figs. 6-6 and 6-7. With a low critical current density ($J_c^J \simeq 5 \times 10^4$ A/cm^2 at 4 K by dc transport measurement), the junction is expected to dominate the film's transport properties. The junction's microwave losses, which are proportional to $1/Q_u$, behave similar to the $R_s \propto 1/Q_u$ of a plain YBCO film (see Chapter 5), dropping down rapidly below T_c and leveling off at low temperature. No local maxima, however, are observed here. The resonant frequency f_0 drops rapidly as T approaches $T_c \simeq 86$ K as expected, since the junction's penetration depth, which dominates the kinetic inductance of the stripline, increases quickly near T_c. At low temperature, f_0 does not level off nearly as much as that for a plain YBCO film (see Chapter 4).

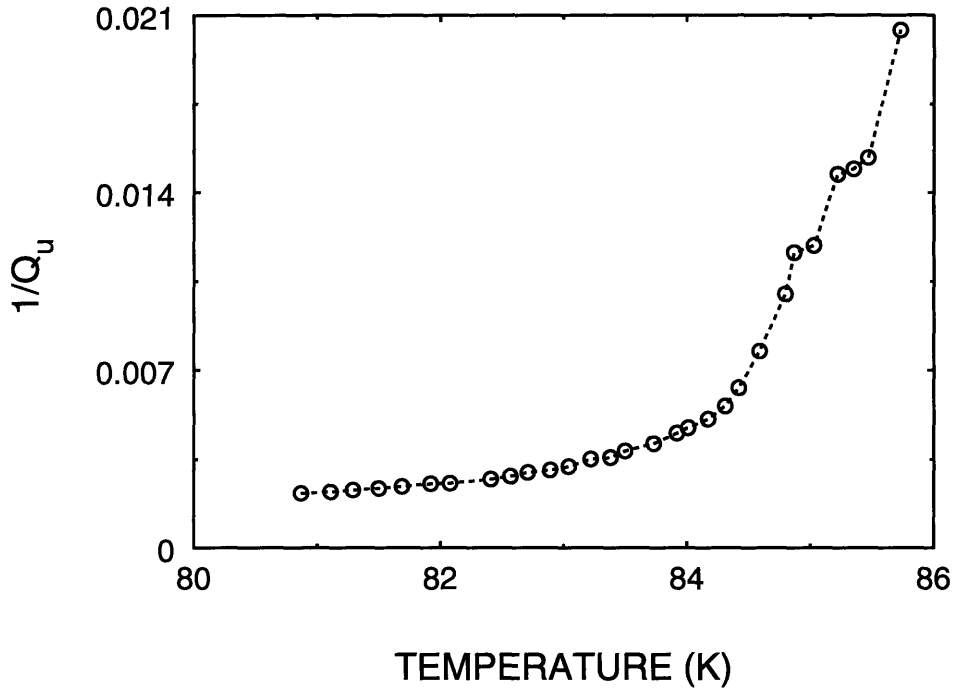

Figure 6-6: $1/Q_u$ vs T for the fundamental mode at 2.1 GHz of an edge junction.

The resonant frequencies f_0 versus the mode number are plotted in Fig. 6-8 at 5 K. For a YBCO plain film, f_0 follows a straight line. A junction added at the midpoint of the center conductor of the stripline resonator is expected to modify the kinetic inductance to shift the f_0 for the odd modes off this straight line. A systematic shift in f_0, however, is not observed here for the odd modes because the geometric inductance is about 500 times larger than the kinetic one [53]. Consequently, the junction provides only a minor perturbation to the resonant frequencies of the system. On the other hand, as shown below, the R_s values for the odd modes are strongly affected. Returning to Fig. 6-9, the geometric inductance hence washes out any changes in f_0, making it possible to apply much of the previous circuit analysis for the plain resonator to the junction-incorporated resonator, at least in the first approximation.

Assuming the same current distribution as for a plain resonator, the peak rf magnetic field $H_{\rm rf}$ at the maxima of the resonant standing wave can be estimated for the junction-incorporated resonator, using the approach described in Chapter 4. Similarly, the effective surface resistance R_s can be obtained from the Q. Fig. 6-9 plots R_s

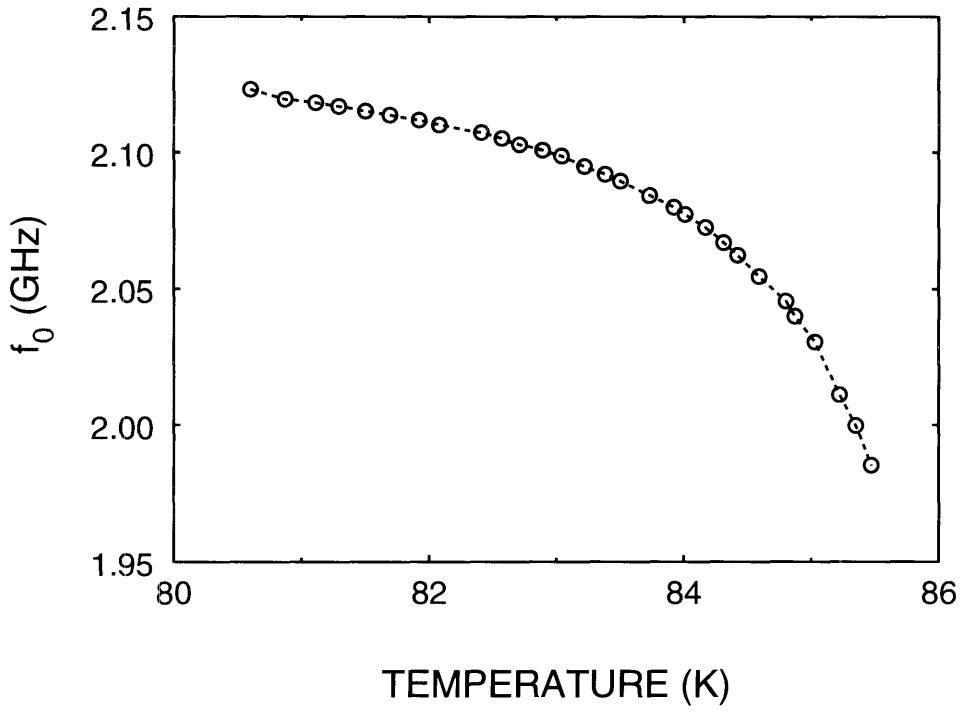

Figure 6-7: Resonant frequency f_0 vs T of the fundamental mode for an edge junction.

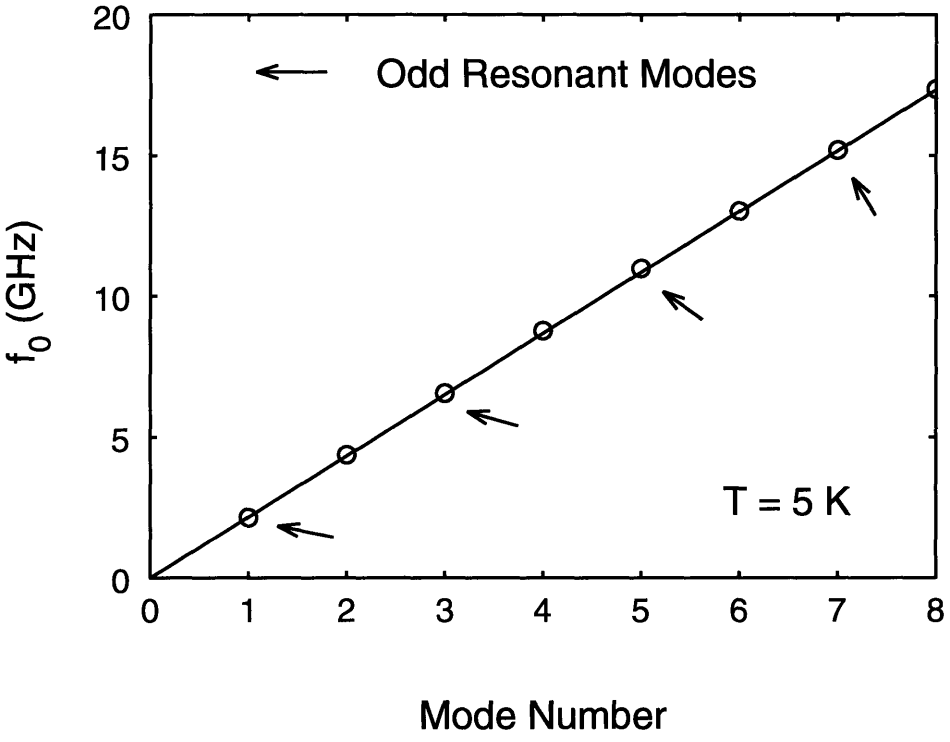

Figure 6-8: Resonant frequency f_0 vs mode number for an edge junction at 5 K. The arrows point to the odd resonant modes.

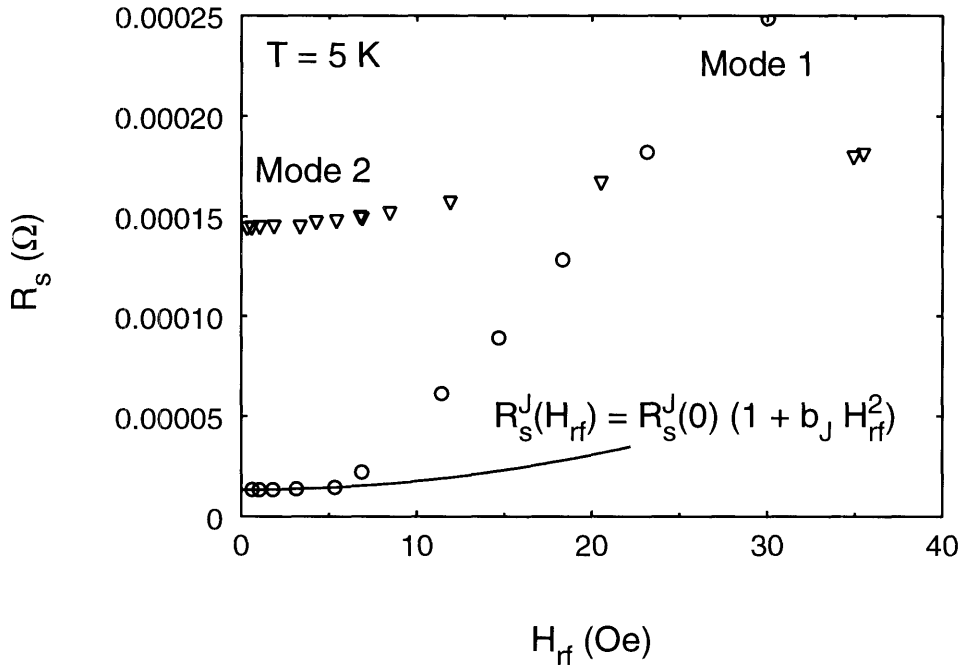

Figure 6-9: R_s vs $H_{\rm rf}$ for the first 2 modes at 5 K. R_s of the fundamental mode 1 is affected by the junction, whereas R_s of mode 2 is not. R_s of mode 1 depends quadratically on $H_{\rm rf}$ below $H_p \simeq 5$ Oe as the quadratic fit (solid line) shows. Note that the junction's H_p value here is much smaller than that for a plain YBCO film (see Chapter 5).

vs H_{rf} of the first two modes for an edge junction at 5 K. R_s of the fundamental mode is observed to increase much more rapidly than that of the second mode, with the two curves crossing at around 18 Oe. This is expected since the fundamental sees the junction which has low J_c and hence high losses, whereas the second mode does not. For the rf field region below 5 Oe, R_s of the fundamental is quadratic in H_{rf} as the quadratic fit (solid line) shows in Fig. 6-9. Above 5 Oe, R_s of the fundamental shoots up rapidly. This behavior of R_s suggests that the junction has a flux penetration field H_p around 5 Oe. Using the Josephson relation between the junction's critical current density J_c^J and the junction's penetration depth λ_J [87], I estimate $\lambda_J \simeq 1.1$ μm and the junction lower critical field $\sim$ 9 Oe. Despite the simplicity of the estimate, the calculated value for vortex penetration is close to the measured H_p. The qualitative behavior of R_s of the fundamental of the junction thus shows consistency with the power-dependent coupled-grain model. R_s of the second mode remains quadratic in the power range considered in Fig. 6-9.

Figure 6-10 plots R_s vs H_{rf} for the fundamental at 70 K for the same junction-incorporated resonator. Here the low-field quadratic region is suppressed beyond the H_{rf}-sensitivity of the measurement as expected, since H_p at this temperature is small ($\sim$ 1 Oe). Above 30 Oe, R_s seems to level off. This field-dependence behavior is similar to that of high-T_c granular films which consist of many grain boundaries [68].

6.3 Summary

I have shown some preliminary measurement results and analysis of stripline resonators designed with YBCO Josephson junctions fabricated at the midpoint of the center conductors. For a junction-incorporated resonator, the effective surface resistance for the fundamental mode, which reflects the junction, shows much stronger dependence on the rf field strength than that for the second mode, which does not see the junction and hence reflects the properties of the film. This is expected since the critical current density of the junction is much smaller than that of the plain film. R_s of the fundamental also exhibits two regions of different dependences on H_{rf}. In

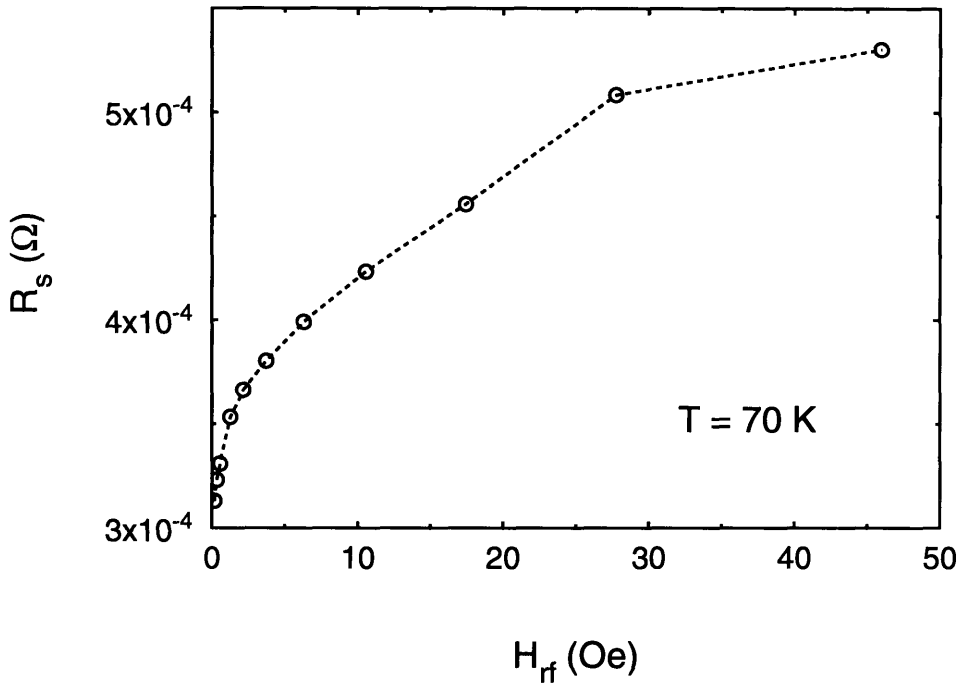

Figure 6-10: R_s vs H_{rf} for mode 1 at 70 K.

the low- and intermediate-field region, R_s has an H_{rf}^2 dependence, as expected by the power-dependent coupled-grain model. Calculation using simple Josephson relations yields a field value that roughly agrees with the measured vortex-penetration field H_p that marks the boundary between the two regions. The qualitative behavior of the R_s of the fundamental mode, that represents the junction, presented above was also reported recently by Hein *et al.* [119], who measured the power dependence of a SQUID coupled to a microstrip resonator.

Further measurements and analysis must be done to gain more insight into the microwave properties of high-T_c junctions. Junction-types other than edge junctions also should be tried, especially grain-boundary junctions which are more closely related to natural grain-boundary junctions in high-T_c films.

Chapter 7

Conclusions

Detailed summaries of the three major projects in this thesis have been given at the end of the corresponding chapters. I will briefly repeat the most important results here and then offer some suggestions for future work.

7.1 Properties of $YBa_2Cu_3O_{7-x}Br_y$ Single Crystals

Non-superconducting de-oxygenated YBCO single crystals have been found to become superconducting with high transition temperature $T_c \simeq 92$ K upon bromination. Bromination of de-oxygenated YBCO single crystals increases the scattering rate as well as the anisotropy with respect to the fully oxygenated YBCO single crystals. The relative lack of variation of $\xi_{ab}(0)$ and the reduction of $\xi_c(0)$ by a factor of 3 upon bromination of YBCO suggest that Br never enters the CuO_2 planes. The pinning energy for vortex motion in the ab plane decreases after bromination and this decrease can be attributed to the increased anisotropy which is measured independently. For vortex motion along the $\hat{c}$ axis, however, the pinning energy decreases or increases depending on temperature and field. Bromination suppresses J_c and makes it strongly dependent on the applied magnetic field. At high temperature, the H_{c1} in the brominated YBCO single crystals indicates a reduction in carrier density (by

a factor of between 2 and 3) which is consistent with the observed reduction in the plasma frequency.

7.2 Power Dependence of Z_s of $YBa_2Cu_3O_{7-x}$ Thin Films at Microwave Frequencies

The large residual surface resistance of R_s (at low microwave power) at low temperature disagrees with conventional BCS theory. Similarly, the strong power dependence of Z_s is inconsistent with calculations using the Ginzburg-Landau theory. These findings motivate the work here that involves measuring Z_s and explaining its behavior with defects and microwave vortices in YBCO thin films.

I have measured the microwave surface impedance as a function of the microwave magnetic field at various temperatures and frequencies for several types of YBCO films of different thicknesses and for NbN films. For both YBCO and NbN, $R_s(H_{\rm rf})$ and $\lambda(H_{\rm rf})$ can be divided into two regions: 1) the low and intermediate rf field and 2) the high rf field. The value of $H_{\rm rf}$ that separates the two regions is the vortex-penetration field $H_p(T)$.

In the low- and intermediate-field region, my measurements show that $R_s \propto f^2$ and $\Delta R_s \propto H_{\rm rf}^2$. Similarly, $\Delta\lambda \propto H_{\rm rf}^2$. With an appropriate set of characteristic parameters — J_c, a, and R_J — I have simultaneously accounted for the behavior of the zero field R_s and the rf field dependence of both R_s and λ as functions of temperature and frequency, using the power-dependent coupled-grain model (for the Meissner phase) in which the superconductor is modeled as a network of superconducting grains of intrinsic properties connected by Josephson junctions whose properties are extrinsic to the fundamental material and depend on sample preparation processes.

It is interesting to note that the fractional power-induced change in R_s is more than one hundred times larger than the fractional change in λ. This is explained by the coupled-grain model in a simple way. The resistance is dominated by the properties of the weak-link Josephson junctions, which show a strong dependence on rf magnetic field. The zero field inductance is dominated by the intrinsic properties of the grains,

which have weak dependencies on rf field. As the rf field is increased, the intergranular inductance increases much more rapidly than the intragranular inductance. The change in the intergranular inductance, however, is moderated by the large zero field intragranular inductance.

In the high-field region, both $R_s(H_{rf})$ and $\lambda(H_{rf})$ deviate from the low-field quadratic dependence on H_{rf}^2. Using a modified Bean model ($H_p > 0$), I adapted Norris's calculations to account quantitatively for the behavior of $R_s^B(H_{rf})$ for most YBCO and NbN films at various temperatures and frequencies with two fitting parameters $H_p(T)$ and $J_c^P(T)$. The measured R_s^B is found to be nearly proportional to frequency for several samples. While I think I have strong evidence that $R_s^B \propto f$, some samples did not show a clearly defined frequency dependence, probably because of film non-uniformity as discussed in Sec. 5.5.3. The frequency dependence of R_s^B hence requires further study to understand the effect of non-uniformity.

The measured values of $H_p(T)$ show vortex penetration occurring at field values closer to the dc $H_{c1}^{\perp c}$ than $H_{c1}^{\parallel c}$ values. This behavior of $H_p(T)$ can be explained by the curvature of the magnetic field at the edge of a superconducting thin-film strip. That the $H_p(T)$ values for YBCO thin films obtained are low, even when compared with the intrinsic $H_{c1}^{\perp c}$ of YBCO single crystals [86], may be attributed to lower vortex-penetration fields for the junction defects and grain boundaries in the films where vortices first penetrate. The field H_p is therefore an extrinsic quantity, leaving considerable room for further improvement of the power-handling capability of the films through improved deposition techniques.

The values of $J_c^P(T)$ extracted from the fits using the hysteretic-loss model agree with the critical current densities $J_c^T(T)$ obtained by dc transport measurements for YBCO but not NbN films. The disagreement for NbN can be explained by considering the effects of strong vs weak pinning on the J_c^T. The strong pinning in YBCO and the weak pinning in NbN also are shown to be responsible for the qualitatively different behavior in R_s above H_p.

Since structural defects that act like Josephson junctions in high-T_c films play an important role in determining the transport properties of the samples, a detailed

study of isolated high-T_c junctions is essential for a better understanding of both the individual junctions and the junction arrays. This reasoning motivated my next project.

7.3 Microwave Properties of High-T_c Josephson Junctions

The YBCO edge junctions were prepared by an *in-situ* laser-ablation deposition process using multiple targets and externally manipulated stainless steel contact masks. Each junction is located at the midpoint of the center conductor of a stripline resonator, so that only the odd resonant modes are altered by the junction. The even resonances are unaffected by the junction, and hence provide an effective means to isolate the properties of the film from those of the junction. At low microwave magnetic fields ($H_{\rm rf} < 5$ Oe), the effective surface resistance R_s for the first odd mode (1.5 GHz) shows a quadratic dependence on $H_{\rm rf}$. This behavior shows consistency with the power-dependent coupled-grain model. At high $H_{\rm rf}$ (i.e., $H_{\rm rf} > H_p \simeq 5$ Oe), R_s increases much more rapidly. Calculations, using simple Josephson relations, yield a field value $H_{\rm c1}$ that roughly agrees with the measured vortex penetration field H_p that marks the boundary between the two regions.

In contrast, the increase of R_s for the first even mode (3.0 GHz) continues to be small and quadratic in $H_{\rm rf}$ up to much higher $H_{\rm rf}$ values.

7.4 Suggestions for Future Work

Future experiments are suggested in this section to further clarify some of the issues related to high-T_c thin films and crystals.

1) Bromination of YBCO thin films could provide interesting physics and important potential for applications, since Br can penetrate a thin film much more easily than a single crystal. Substitution of oxygen in YBCO with other halogens should also be studied further for the purpose of comparison with Br-doping.

2) A systematic investigation of the correlation among Z_s, J_c, T_c, normal resistivity ρ_n, and X-ray, SEM, TEM, and STM structural analysis is highly desirable for both the science and technology of high-T_c materials.

3) Introduction of artificial defects such as by irradiation or de-oxygenation would help clarify the role of small scale defects in the low- and intermediate-rf-field region. In the high-rf-field region, the artificial defects would create extra pinning sites for rf vortices. How this increase in the number of pinning sites affect the microwave losses is of great interest to applications.

4) The effect of film thickness on the microwave losses, especially on the power dependence, requires further systematic study. Thicker films appear to drastically reduce the nonlinearity in Z_s.

5) The behavior of the intermodulation products of high-T_c thin films is presently poorly understood. Further measurements and modeling are highly desirable as these IM distortions characterize the performance of superconducting microwave devices such as microwave filters.

6) The nucleation and propagation process of vortices created by microwave magnetic fields requires further investigation. Outstanding questions include the nucleation and propagation times for high-T_c materials compared with conventional superconductors; and the cutoff frequencies above which microwave vortices are too slow to be created. These cutoff frequencies are highly important technologically, since superconducting microwave devices operating above these frequencies would suffer no hysteretic losses. At high frequencies, hysteretic losses can be very large.

7) Further improvement of the power-dependent coupled-grain model to take into account shunting and the distribution in defect structures in high-T_c thin films can be made to better fit the data. Similarly, in the high-rf-field region, the hysteretic model presented in this work can be improved by taking into account the different types of rf vortices: intra- and intergranular rf vortices.

8) More measurements and analysis need to be carried out to gain more insight into the microwave properties of high-T_c Josephson junctions, especially the power dependence which is not well-understood yet. Josephson junctions other than edge

junctions should also be studied, especially grain-boundary junctions which are more closely related to natural grain-boundary junctions in high-T_c films.

9) Measurement of Z_s in an applied dc magnetic field can provide important insights into the dependence of Z_s on $H_{\rm rf}$. In the Meissner state, rf and dc magnetic fields should produce the same qualitative effects on the sample. In the mixed state induced by a large rf field, rf vortices can be created, moved, and annihilated, producing large hysteretic losses. A small rf field in the mixed state induced by a large applied dc magnetic field, on the other hand, experiences much smaller hysteretic losses.

10) The quest for high-T_c materials with smaller loss and better power-handling capabilities must continue, as it will contribute greatly to the understanding of the properties of high-T_c superconductors, and to application of these fascinating materials at high frequencies.

Appendix A

Field at Edges of Conducting Media

Field at Edges of Normal Conducting Media

To address the magnetic field strength at the edges of a strip, I first review the case of a nonsuperconducting wedge surrounded by a homogeneous dielectric medium with a common straight edge. Figure A-1 shows the cross section (perpendicular to the edge) in cylindrical coordinates (ρ, ϕ, z) where ϵ_a, μ_a, and $\sigma_a = \sigma_{a,1} + j\sigma_{a,2}$ are the permitivity, permeability, and complex conductivity, respectively, of the conducting wedge, while ϵ_b and μ_b are the permitivity and permeability of the surrounding dielectric medium. I consider only the lossless dielectric medium situation with real ϵ_a, ϵ_b, μ_a, and μ_b.

For $\sigma_{a,1} = \infty$ (perfect conductivity), using the edge condition that the electromagnetic energy density must be integrable over any finite domain, Meixner [120] studies the singularity of the electric and magnetic fields in the neighborhood of the common edge of angular dielectric or conducting regions at frequencies ranging from dc to microwave. He finds that the magnetic field components H_ρ and $H_\phi \rightarrow \infty$ at the edge ($\rho \rightarrow 0$) for a sharp wedge ($\phi_0 > \pi$) or an infinitely thin film ($\phi_0 = 2\pi$).

Extending Meixner's approach to the case $\sigma_{a,1} < \infty$ (lossy conductivity), Geisel *et al.* [121] discovers that H_ρ and H_ϕ remain bounded unless the media have different magnetic permeabilities [121] ($\mu_a \neq \mu_b$).

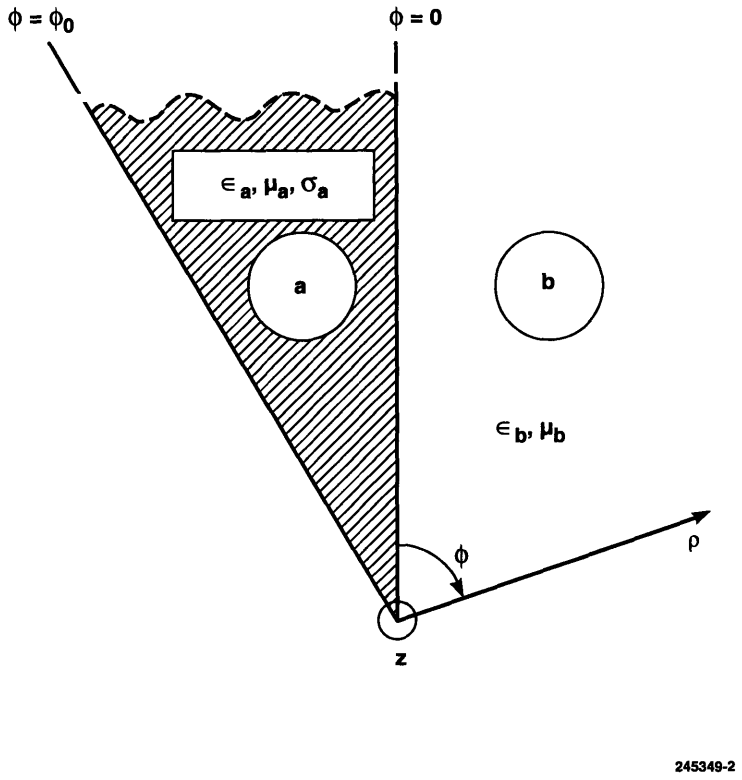

Figure A-1: Cross section of an infinitely long conducting wedge with complex conductivity $\sigma_a = \sigma_{a,1} - j\sigma_{a,2}$ surrounded by a lossy dielectric medium. For a normal conductor, the imaginary part $\sigma_{a,2}$ is neglected at low enough frequencies f (typically for $f < 10^{11}$ Hz).

The field component parallel to the wedge H_z is bounded in all the above cases [120, 121].

Field at Edges of Superconducting Media

From the two-fluid model, the complex conductivity for the superconductor (region a in Fig. A-1) is $\sigma_a = \sigma_{a,1} - j\sigma_{a,2}$ where $\sigma_{a,1} = n_n e^2 \tau / m$ for low enough frequencies f (typically for $f < 10^{11}$ Hz) [87] where n_n and m are the density and mass of the normal carriers, e the electronic charge, and τ the scattering time. An effective complex permitivity can then be written $\epsilon_a = (\epsilon_a - \sigma_{a,2}) - j\sigma_{a,1}/2\pi f$. For $n_n >$

0 (at non-zero temperature), the superconducting wedge thus behaves like a lossy conductor of finite conductivity $\sigma_{a,1} < \infty$, assuming $\mu_b = \mu_0$. Note that I have taken $\mu_a = \mu_b = \mu_0$ since I have treated the superconductor as a non-magnetic material, with the induced magnetization accounted for by the shielding supercurrent [11]. Thus the magnetic field amplitude at the edges is bounded just as it would be for a lossy normal conducting wedge. This is the case of interest in this work.

For $n_n = 0$ (at zero temperature assuming all carriers become paired), the superconducting wedge can be treated as a lossless ($\sigma_{a,1} = 0$) dielectric instead of a conducting wedge. For a right-angle dielectric wedge ($\phi_0 = 3\pi/2$), the magnetic field at the edges is also found to be bounded [122].

The magnetic field at the edges of a superconducting wedge or thin film is thus finite, at least at temperatures greater than 0. In fact, the current and field distributions in the Meissner state can be *exactly* solved numerically using the London and Maxwell equations. Sheen *et al.* [53] divide the stripline cross-section into many small grids and numerically calculate the current and field in each grid. By observing the saturating currents and fields in the grids at the corners and edges as the grid size is continually decreased, they have concluded that these currents and fields remain finite at all times [53].

Bibliography

[1] R. Beyers and T. M. Shaw, Solid State Physics **42**, 135 (1989).

[2] R. Beyers, G. Lim, E. M. Engler, V. Y. Lee, M. L. Ramirez, R. J. Savoy, R. D. Jacowitz, T. M. Shaw, S. LaPlaca, R. Boehme, C. C. Tsui, S. I. Park, M. W. Shafer, and W. J. Gallagher, Appl. Phys. Lett. **51**, 614 (1987).

[3] R. Byers, G. Lim, E. M. Engler, R. J. Saboy, T. M. Shaw, T. R. Dinger, W. J. Gallagher, and R. J. Sandstrom, Appl. Phys. Lett. **50**, 1918 (1987).

[4] K. Ikeda, M. Nagata, M. Ishihara, S. Kumazawa, T. Shibayama, A. Imagawa, T. Sugamata, H. Katoh, N. Momozawa, K. Umezawa, and K. Ishida, J. J. Appl. Phys. **27**, L202 (1988).

[5] R. J. Cava, B. Batlogg, C. H. Chen, E. A. Rietman, S. M. Zahurak, and D. Werder, Phys. Rev. B **36**, 5719 (1987).

[6] E. D. Specht, C. J. Sparks, A. G. Dhere, J. Brynestad, O. B. Cavin, D. M. Kroeger, and H. A. Oye, Phys. Rev. B **37**, 7426 (1988).

[7] Y. Iye, Physica B **163**, 63 (1990).

[8] J. B. Goodenough, A. Manthiram, Y. Dai, and A. Campion, Supercond. Sci. Technol. **1**, 187 (1988).

[9] J. J. Neumeier, T. Bjornholm, M. B. Maple, and Ivan K. Schuller, Phys. Rev. Lett. **63**, 2516 (1989).

[10] W. E. Lawrence and S. Doniach. In *Low Temperature Physics*, page 361. editor E. Kandu, Tokyo, 1971.

[11] T. P. Orlando and K. A. Delin. In *Foundations of Applied Superconductivity*, page 178. Addison-Wesley Publishing Company, Inc., Reading, MA, 1991.

[12] D. R. Harshman, G. Aeppli, E. J. Ansaldo, B. Batlogg, J. H. Brewer, J. F. Carolan, R. J. Cava, M. Celio, A. C. D. Chaklader, W. N. Hardy, S. R. Kreitzman, G. M. Luke, D. R. Noakes, and M. Senba, Phys. Rev. **B36**, 2386 (1987).

[13] D. Bhatt, S. N. Basu, A. C. Westerheim, and A. C. Anderson, Physica C **222**, 283 (1994).

[14] J. Geerk, G. Linker, and O. Meyer, Mater. Sci. Rep. **4**, 193 (1989).

[15] R. W. Simon, C. E. Platt, A. E. Lee, G. S. Lee, K. P. Daly, and M. S. Wire, Appl. Phys. Lett. **53**, 2677 (1988).

[16] A. C. Westerheim. In *Sputter Deposition and Characterization of* in situ *Superconducting Y-Ba-Cu-O Thin Films.* Ph.D. Thesis, Department of Materials Science and Engineering, MIT, Cambridge, MA, 1992.

[17] A. S. Westerheim, A. C. Anderson, D. E. Oates, S. N. Basu, D. Bhatt, and M. J. Cima, J. Appl. Phys. (1994). In press.

[18] T. L. Hylton, Ph. D. thesis, Dept. of Phys., Stanford University (1991).

[19] A. V. Narlikar, C. V. Narashimha Rao, and S. K. Agarwal. In *Studies of High Temperature Superconductors*, page 341, 1989.

[20] Yu. A. Ossipyan, O. V. Zharikov, N. S. Sidorov, V. I. Kulavkov, D. N. Mogilyanskii, R. K. Nikoloev, V. Sh. Shekhtman, O. A. Volegova, and I. M. Romanenko, JETP Lett. **48**, 247 (1988).

[21] Yu. A. Ossipyan, O. V. Zharikov, G. V. Norikov, N. S. Sidorov, V. I. Kulakov, L. V. Sipavina, R. K. Nikoloev, and A. M. Gromov, JETP Lett. **48**, 247 (1989).

[22] H. B. Radousky, R. S. Glass, P. A. Hahn, M. J. Fluss, R. G. Meisenheimer, B. P. bonner, C. I. Mertzbacher, E. M. Larson, K. D. McKeegan, J. C. O'Brian, J. L. Peng, R. N. Shelton, and K. F. McCarty, Phys. Rev. B **41**, 11140 (1990).

[23] A. Tressaud, B. Chevalier, B. Lepine, J. M. Dance, L. Lozano, T. Grannec, T. Etourneau, R. Tournier, A. Sulpice, and P. Lejay, Mod. Phys. Lett. B **2**, 1183 (1988).

[24] Y. X. Jia, J. Z. Liu, M. D. Lan, P. Klavins, R. N. Shelton, and H. B. Radousky, Phys. Rev. B **45**, 10609 (1992).

[25] E. E. Amitin, N. V. Bausck, S. A. Gromilov, S. G. Kozlova, N. K. Moroz, L. N. Mazalov, V. N. Naumov, P. P. Samoilov, S. A. Slobdjan, M. A. Starikov, V. E. Fedorov, G. I. Frolova, and S. B. Ehrenburg, Physica C (1992).

[26] Y. A. Ossipyan and O. V. Zharikov, Physica C **162-164**, 79 (1989).

[27] Y. A. Ossipyan, O. V. Zharikov, G. Y. Logvenov, N. S. Sidorov, V. I. Kulakov, I. M. Shmytko, I. K. Bdikin, and A. M. Gromov, Physica C **165**, 107 (1990).

[28] A. Williams, G. H. Kwei, R. B. Von Dreele, A. C. Larson, I. D. Raistrik, and D. L. Bish, Phys. Rev. B **37**, 7460 (1988).

[29] J. D. Jorgensen, H. B. Schuttler, D. G. Hinks, D. W. Capne, K. Zhang, M. B. Brodski, and D. J. Scalapino, Phys. Rev. Lett. **58**, 1024 (1987).

[30] Y. Wang, A. M. Rao, J. G. Zhang, X. X. Bi, P. C. Eklund, M. S. Dresselhaus, P. P. Nguyen, J. S. Moodera, G. Dresselhaus, H. B. Radousky, R. S. Glass, M. J. Fluss, and J. Z. Liu, Phys. Rev. B **45**, 2523 (1992).

[31] M. D. Lan, J. Z. Liu, and R. N. Shelton, Phys. Rev. B **43**, 12989 (1991).

[32] F. J. Blunt, A. R. Perry, A. M. Campbell, and R. S. Liu, Physica C **175**, 539 (1991).

[33] Yu. T. Pavlyukhin, A. P. Nemudry, N. G. Khainovsky, and V. V. Boldyrev, Solid State Commun. **72**, 107 (1989).

[34] Yu. A. Ossipyan, O. V. Zharikov, V. L. Matukhin, and V. N. Anashkin, Zeits. f. Naturforsh. A **47**, 21 (1992).

[35] C. P. Bean, Phys. Rev. Lett. **8**, 250 (1962).

[36] W. A. Fietz and W. W. Webb, Phys. Rev. B **178**, 657 (1969).

[37] T. Penney, S. von Molnar, D. Kaiser, F. Holtzberg, and A. W. Kleinsasser, Phys. Rev. B **38**, 2918 (1988).

[38] T. Ito, H. Takagi, S. Ishibashi, T. Ido, and S. Uchida, Nature **350**, 596 (1991).

[39] N. R. Werthamer, E. Helfand, and P. C. Hohenberg, Phys. Rev. **147**, 295 (1966).

[40] Y. Iye, T. Sakakibara, T. Goto, N. Miura, H. Takeya, and H. Takei, Physica C **153-155**, 26 (1988).

[41] J. S. Moodera, R. Meservey, J. E. Tkaczyk, C. X. Hao, G. A. Gibson, and P. M. Tedrow, Phys. Rev. B **37**, 619 (1988).

[42] M. Tinkham, in *Introduction to Superconductivity*, (McGraw-Hill, Inc., New York, NY, 1975).

[43] T. T. M. Palstra, B. Batlogg, L. F. Schneemeyer, and J. V. Waszczak, Phys. Rev. B **43**, 3756 (1991).

[44] T. T. M. Palstra, B. Batlogg, R. B. van Dover, L. F. Schneemeyer, and J. V. Waszczak, Phys. Rev. B **41**, 6621 (1990).

[45] S. Chakravarty, B. I. Ivelev, and Y. N. Ovchinnikov, Phys. Rev. Lett. **64**, 3187 (1990).

[46] M. D. Lan, J. Z. Liu, and R. N. Shelton, Phys. Rev. B **44**, 233 (1991).

[47] L. Burlachkov, Y. Yeshurun, M. Konczykowski, and F. Holtzberg, Phys. Rev. B **45**, 8193 (1992).

[48] W. E. Farneth, R. K. Bordia, E. M. McCarron III, M. K. Crawford, and R. B. Flippen, Solid St. Commun. **66**, 953 (1988).

[49] A. J. Jacobsen, J. M. Newsam, D. C. Johnston, D. P. Goshorn, J. T. Lewandowski, and M. S. Alvarez, Phys. Rev. B **39**, 254 (1989).

[50] J. G. Ossandon, J. R. Thompson, D. K. Christen, B. C. Sales, H. R. Kerchner, J. O. Thomson, Y. R. Sun, K. W. Lay, and J. E. Tkaczyk, Phys. Rev. B **45**, 12534 (1992).

[51] M. S. Dilorio, A. C. Anderson, and B-Y. Tsaur, Phys. Rev. B **38**, 7019 (1988).

[52] W. T. Weeks, L.L. Wu, M. F. McAllister, and A. Singh, IBM J. Res. Develop. **23**, 652 (1979).

[53] D. M. Sheen, S. M. Ali, D. E. Oates, R. S. Withers, and J. A. Kong, IEEE Trans. on Appl. Supercond. **AS-1**, 108 (1991).

[54] D. E. Oates, A. C. Anderson, D. M. Sheen, and S. M. Ali, IEEE Trans. Microwave Theory and Tech. **39**, 1522 (1991).

[55] D. C. Mattis and J. Bardeen, Phys. Rev. **111**, 412 (1979).

[56] S. M. Anlage, B. W. Langley, G. Deutscher, J. Halbritter, and M. R. Beasley, Phys. Rev. **B44**, 9764 (1991).

[57] G. L. Matthaei, L. Young, and E. M. T. Jones. In *Microwave Filters, Impedance-Matching Networks, and Coupling Structures.* McGraw-Hill, New York, 1964.

[58] L. D. Landau and E. M. Liftschitz. In *Mechanics.* Pergamon, Elmsford, New York, 1988.

[59] J. Halbritter, J. Appl. Phys. **41**, 4581 (1970).

[60] J. H. Oates, R. T. Shin, D. E. Oates, M. J. Tsuk, and P. P. Nguyen, IEEE Trans. on Applied Superconductor **in press** (1993).

[61] A. M. Portis, D. W. Cooke, and E. R. Gray, J. Superconduct. **3**, 297 (1990).

[62] C. W. Lam, D. M. Sheen, S. M. Ali, and D. E. Oates, IEEE Trans. Appl. Supercond. **2**, 58 (1992).

[63] P. P. Nguyen, D. E. Oates, G. Dresselhaus, and M. S. Dresselhaus, Phys. Rev. B **48**, 6400 (1993).

[64] H. Piel, H. Chaloupka, and G. Müller. In *Advances in Superconductivity IV*, page 925. Springer Verlag, Tokyo, 1992.

[65] D. E. Oates, P. P. Nguyen, G. Dresselhaus, M. S. Dresselhaus, C. W. Lam, and S. M. Ali, J. Superconduct. **5**, 361 (1992).

[66] A. A. Valenzuela, G. Sölkner, J. Kessler, and P. Russer, High Temperature Superconductors, PhD Thesis (1992).

[67] J. R. Delayen and C. L. Bohn, Phys. Rev. **B40**, 5151 (1989).

[68] J. Halbritter, J. Appl. Phys. **68**, 6315 (1990).

[69] J. Halbritter, Supercond. Sci. Technol. **4**, 127 (1991).

[70] J. Halbritter, J. Superconduct. **5**, 171 (1992).

[71] T. L. Hylton, A. Kapitulnik, M. R. Beasley, J. P. Carini, L. Drabeck, and G. Grüner, Appl. Phys. Lett. **53**, 1343 (1988).

[72] K. Scharnberg and D. Walker, J. Superconduct. **3**, 269 (1990).

[73] W. Rauch, E. Gornik, G. Sölkner, A. A. Valenzuela, F. Fox, and H. Behner, J. Appl. Phys. **73**, 1866 (1993).

[74] A. S. Westerheim, L. S. Yu-Jahnes, and A. C. Anderson, IEEE Trans. Magn. **27**, 1001 (1991).

[75] A. C. Anderson, unpublished (1994).

[76] R. H. Ono, J. A. Beall, M. W. Cromar, T. E. Harvey, M. E. Johansson, C. D. Reintsema, and D. A. Rudman, Appl. Phys. Lett. **59**, 1126 (1991).

[77] A. C. Anderson, D. J. Lichtenwalner, and W. T. Brogan, IEEE Trans. Magn. **25**, 2084 (1989).

[78] C. C. Chin, D. E. Oates, G. Dresselhaus, and M. S. Dresselhaus, Phys. Rev. B **45**, 4788 (1992).

[79] D. E. Oates, Alfredo C. Anderson, C. C. Chin, J. S. Derov, G. Dresselhaus, and M. S. Dresselhaus, Phys. Rev. B **43**, 7655 (1991).

[80] D. A. Bonn, P. Dosanjh, R. Lang, and W. N. Hardy, Phy. Rev. Lett. **68**, 2390 (1992).

[81] C. W. Lam, D. E. Oates, and S. M. Ali, Presentation at ASC (1992).

[82] J. I. Gittleman and B. Rosenblum, Phys. Rev. Lett. **16**, 735 (1966).

[83] D. Walker and K. Scharnberg, Phys. Rev. B **42**, 2211 (1990).

[84] T. L. Hylton and M. R. Beasley, Phys. Rev. **B39**, 9042 (1989).

[85] C. Attanasio, L. Mariato, and R. Vaglio, Phys. Rev. **B43**, 6128 (1991).

[86] Dong-Ho Wu and S. Sridhar, Phys. Rev. Lett. **65**, 2074 (1990).

[87] T. van Duzer and C. W. Turner. In *Principles of Superconductive Devices and Circuits*. Elsevier North Holland, Inc., New York, NY, 1981.

[88] N. Klein, U. Poppe, N. Tellmann, H. Schulz, W. Evers, U. Dähne, and K. Urban, IEEE Trans. on Applied Superconductor **3**, 1102 (1993).

[89] S. Sridhar, Dong-Ho Wu, and W. Kennedy, Phys. Rev. Lett. **63**, 1873 (1989).

[90] D. E. Oates, A. C. Anderson, and P. M. Mankiewich, J. Supercond. **3**, 251 (1990).

[91] C. B. Eom, J. Z. Sun, K. Yamamoto, A. F. Marshall, K. E. Luther, S. S. Laderman, and T. H. Geballe, Appl. Phys. Lett. **55**, 595 (1989).

[92] C. B. Eom, J. Z. Sun, B. M. Lairson, S. K. Streiffer, A. F. Marshall, K. Yamamoto, S. M. Anlage, J. C. Bravman, and T. H. Geballe, Physica C **171**, 354 (1990).

[93] J. Halbritter, Z. Phys. **266**, 209 (1974).

[94] R. Gross, P. Chaudhari, M. Kawasaki, and A. Gupta, Phy. Rev. **B42**, 10735 (1990).

[95] P. Chaudhari, J. Mannhart, D. Dimos, C. C. Tsuei, J. Chi, M. M. Oprysko, and M. Scheuermann, Phy. Rev. Lett. **60**, 1653 (1988).

[96] J. R. Clem, Physica C **153-155**, 50 (1988).

[97] M. Tinkham and C. J. Lobb, Solid State Physics **42**, 91 (1989).

[98] A. M. Portis, J. Superconduct. **5**, 319 (1992).

[99] D. E. Oates, W. G. Lyons, and A. C. Anderson, Proc. of 45*th* Ann. Frequency Symposium page 460 (1991).

[100] W. A. Fietz, M. R. Beasley, J. Silcox, and W. W. Webb, Phys. Rev. **136**, A335 (1964).

[101] W. I. Dunn and P. Hlawiczka, Brit. J. Appl. Phys. (J. Phys. D) **1**, 1469 (1968).

[102] W. T. Norris, J. Phys. D **3**, 489 (1970).

[103] P. P. Nguyen, Z. H. Wang, A. M. Rao, M. S. Dresselhaus, J. S. Moodera, G. Dresselhaus, H. B. Radousky, and R. S. Glass, Phys. Rev. B **48**, 1148 (1993).

[104] J. R. Clem, J. Appl. Phys. **50**, 3518 (1979).

[105] E. H. Brandt and M. Indenbom, Phys. Rev. B **48**, 12893 (1993).

[106] Ch. Heinzel, Ch. Neumann, Th. Ritzi, and P. Ziemann, J. Superconduct. **5**, 319 (1992).

[107] D. C. Bullock, T. J. Folkerts, P. Klavins, and R. N. Shelton, Physica C **162-164**, 331 (1989).

[108] R. A. Klemm, Phys. Rev. B **47**, 14630 (1993).

[109] S. Senoussi and C. Aguillon, Europhys. Lett. **12**, 273 (1990).

[110] D. E. Farrell *et al.*, Phys. Rev. Lett. **64**, 1573 (1990).

[111] Y. Yeshurun and A. P. Malozemoff, Phys. Rev. Lett. **60**, 2202 (1988).

[112] R. M. Easson and P. Hlawiczka, Brit. J. Appl. Phys. (J. Phys. D) **1**, 1477 (1968).

[113] S. Sridhar, Submitted to JAP (1994).

[114] R. Gross. In *Interfaces in High-T_c Superconducting Systems*, pages 176–209. Springer-Verlag New York, Inc., 1994.

[115] K. K. Likharev, Rev. Mod. Phys. **51**(1), 101 (1979).

[116] G. Koren, E. Aharoni, E. Polturak, and D. Cohen, Appl. Phys. Lett. **58**, 634 (1991).

[117] G. Koren, E. Polturak, E. Aharoni, and D. Cohen, Appl. Phys. Lett. **59**, 2745 (1991).

[118] G. Koren, E. Polturak, D. Cohen, E. Aharoni, and L. Patlagan, Physica C **221**, 157 (1994).

[119] M. A. Hein, M. Strupp, and H. Piel. In *Proceedings of European Conference on Applied Superconductivity*, page 1, 1993.

[120] J. Meixner, IEEE Trans. Antennas Propagat. **AP-20**, 442 (1972).

[121] J. Geisel, K.-H. Muth, and W. Heinrich, IEEE Trans. Microwave Theory and Tech. **40**, 158 (1992).

[122] M. Bressan and P. Gamba, IEEE Microwave and Guided Wave Lett. **4**, 3 (1994).